ABSTRACT

Title of Dissertation:	ADVANCED IMAGING AND DATA MINING TECHNOLOGIES FOR MEDICAL AND FOOD SAFETY APPLICATIONS
	Lu Jiang, Doctor of Philosophy, 2009
Dissertation Directed By:	Professor Yang Tao, the Fischell Department of Bioengineering

As one of the most fast-developing research areas, biological imaging and image analysis receive more and more attentions, and have been already widely applied in many scientific fields including medical diagnosis and food safety inspection. To further investigate such a very interesting area, this research is mainly focused on advanced imaging and pattern recognition technologies in both medical and food safety applications, which include 1) noise reduction of ultra-low-dose multi-slice helical CT imaging for early lung cancer screening, and 2) automated discrimination between walnut shell and meat under hyperspectral florescence imaging.

In the medical imaging and diagnosis area, because X-ray computed tomography (CT) has been applied to screen large populations for early lung cancer

detection during the last decade, more and more attentions have been paid to studying low-dose, even ultra-low-dose X-ray CTs. However, reducing CT radiation exposure inevitably increases the noise level in the sinogram, thereby degrading the quality of reconstructed CT images. Thus, how to reduce the noise levels in the low-dose CT images becomes a meaningful topic. In this research, a nonparametric smoothing method with block based thin plate smoothing splines and the roughness penalty was introduced to restore the ultra-low-dose helical CT raw data, which was acquired under 120 kVp / 10 mAs protocol. The objective thorax image quality evaluation was first conducted to assess the image quality and noise level of proposed method. A web-based subjective evaluation system was also built for the total of 23 radiologists to compare proposed approach with traditional sinogram restoration method. Both objective and subjective evaluation studies showed the effectiveness of proposed thin-plate based nonparametric regression method in sinogram restoration of multi-slice helical ultra-low-dose CT.

In food quality inspection area, automated discrimination between walnut shell and meat has become an imperative task in the walnut postharvest processing industry in the U.S. This research developed two hyperspectral fluorescence imaging based approaches, which were capable of differentiating walnut small shell fragments from meat. Firstly, a principal component analysis (PCA) and Gaussian mixture model (PCA-GMM)-based Bayesian classification method was introduced. PCA was used to extract features, and then the optimal number of components in PCA was selected by a cross-validation technique. The PCA-GMM-based Bayesian classifier was further applied to differentiate the walnut shell and meat according to the class-conditional probability and the prior estimated by the Gaussian mixture model. The experimental results showed the effectiveness of this PCA-GMM approach, and an overall 98.2% recognition rate was achieved. Secondly, Gaussian-kernel based Support Vector Machine (SVM) was presented for the walnut shell and meat discrimination in the hyperspectral florescence imagery. SVM was applied to seek an optimal low to high dimensional mapping such that the nonlinear separable input data in the original input data space became separable on the mapped high dimensional space, and hence fulfilled the classification between walnut shell and meat. An overall recognition rate of 98.7% was achieved by this method.

Although the hyperspectral fluorescence imaging is capable of differentiating between walnut shell and meat, one persistent problem is how to deal with huge amount of data acquired by the hyperspectral imaging system, and hence improve the efficiency of application system. To solve this problem, an Independent Component Analysis with k-Nearest Neighbor Classifier (ICA-kNN) approach was presented in this research to reduce the data redundancy while not sacrifice the classification performance too much. An overall 90.6% detection rate was achieved given 10 optimal wavelengths, which constituted only 13% of the total acquired hyperspectral image data. In order to further evaluate the proposed method, the classification results of the ICA-kNN approach were also compared to the kNN classifier method alone. The experimental results showed that the ICA-kNN method with fewer wavelengths had the same performance as the kNN classifier alone using information from all 79 wavelengths. This demonstrated the effectiveness of the proposed ICA-kNN method for the hyperspectral band selection in the walnut shell and meat classification.

ADVANCED IMAGING AND DATA MINING TECHNOLOGIES FOR MEDICAL AND FOOD SAFETY APPLICATIONS

By

LU JIANG

Dissertation submitted to the Faculty of the Graduate School of the
University of Maryland, College Park, in partial fulfillment
of the requirements for the degree of
Doctor of Philosophy
2009

Advisory Committee:
Professor Yang Tao, Chair
Professor Adel Shirmohammadi
Professor Eliot Siegel
Professor Hubert Montas
Professor Nam Sun Wang

Acknowledgements

I would like to give my deepest gratitude to my advisor, Dr. Yang Tao for providing me with great graduate education and research guidance, for offering me tremendous scientific opportunities and economic support, and for showing me how to approach my work as a top imaging scientist.

I wish to express my warm and sincere thanks to my committee members: Dr. Adel Shirmohammadi, Dr. Eliot Siegel, Dr. Hubert Montas and Dr. Nam Sun Wang. Their support and thoughtfulness made my research life smooth and rewarding.

I would like to thank all the members at the Bio-imaging and machine vision laboratory: Fenghua Jin, Lei Qin, Hansong Jing, Xin Chen, Xuemei Cheng, Abby Vogel, Angela Vargas, and Gary Seibel for their friendship and help. It would have been a lonely lab without them.

I owe my loving thanks to my husband Bin Zhu, my daughter Sophia, and my whole family. They were always there cheering me up and stood by me through the good times and challenges. I would never have been able to finish my dissertation without their enduring love.

Table of Contents

List of Tables

List of Figures

1 Introduction

1.1 Motivations

Food and medical care are the two fundamental and vital "ingredients" of human life. In the modern society, people pay even more attentions to their diet and health than ever before. Each year the U.S. government invests a huge amount of money for research on food safety and healthcare to improve the quality of human life. As a non-invasive, high efficient approach, bio-imaging technique becomes more and more popular these days. Intensive research efforts have been put into this research, which is believed to have the great potential to resolve many challenge problems in both food safety inspection and medical diagnosis areas in the near future.

In medical application, growing concerns have recently been raised about the side effect of annual screening of smokers and former smokers for early-stage lung cancer detection recently. With such early-detection followed by prompt treatments, the survival rate of lung cancer patients can be significantly increased (Health Alliance, 2009). However, because a larger population is involved in X-ray computed tomography (CT) lung cancer screening exams, radiation exposure becomes an issue which may cause radiation-induced lung cancer if not properly taken care of (Brenner, et al., 2007). To solve this radiation issue, a low-dose or ultra-low-dose CT imaging device is desired. On the other hand, reducing radiation exposure of CT, i.e. lowering the current (mAs), will inevitably increase noise level in the sinogram as well as degrade the quality of reconstructed CT images. As a result, developing an effective approach to reduce the image noise of low-dose multi-slice helical CT without sacrificing image resolution becomes very important.

In food quality inspection application, automated differentiation between walnut shell and meat has become a critical task in the walnut postharvest processing industry in the U.S. The eastern black walnut, which grows throughout the central and eastern parts of the U.S., has a rich and distinctive flavor and is often used as an additive in value-added foods. The shell fragments of black walnuts are hard and especially hazardous to consumers. Therefore, automated detection of walnuts shell from meat is very important in walnuts food quality inspection.

1.2 Objectives

The overall objective of this research is to explore advanced bio-imaging and data mining technologies in both early lung cancer screening and automated food safety inspection applications.

Specifically, it will include the following sub-objectives:

1) To decrease the noise levels and streak artifacts in multi-slice low-dose helical CT and explore an alternative way to improve the quality of ultra-low-dose multi-slice helical CT images without sacrificing image resolution.
2) To explore the physical difference between walnuts shell and meat, identify the effective vision method by using the hyperspectral fluorescence imaging technique, and develop novel data mining and pattern recognition approaches to classify the walnuts shell and meat.

3) To select the optimal waveband information from walnut hyperspectral fluorescence imagery, and subsequently develop a multispectral imaging technology which is capable of automatically discriminating the walnut shells from the meat.

1.3 Organization

This Ph. D. dissertation is laid out as the following: The researches according to the sub-objectives are introduced in Chapters 2, 3 and 4, respectively. These three chapters are also organized as journal paper style. The conclusions as well as the future work are presented in Chapter 5 and 6. Because of the journal paper style in chapter 2, 3 and 4, certain repeating is expected in this dissertation in order to make these chapters stand alone.

2 Noise Reduction in Ultra-Low-Dose Multi-slice Helical CT

2.1 Introduction

Computed tomography (CT) has revolutionized diagnostic radiology. Figure 2.1 shows the estimated number of CT scans performed since 1980's annually in the United States. It is estimated more than 62 million CT scans per year are currently obtained in the United States, including at least 4 million for children. (Brenner, et al., 2007)

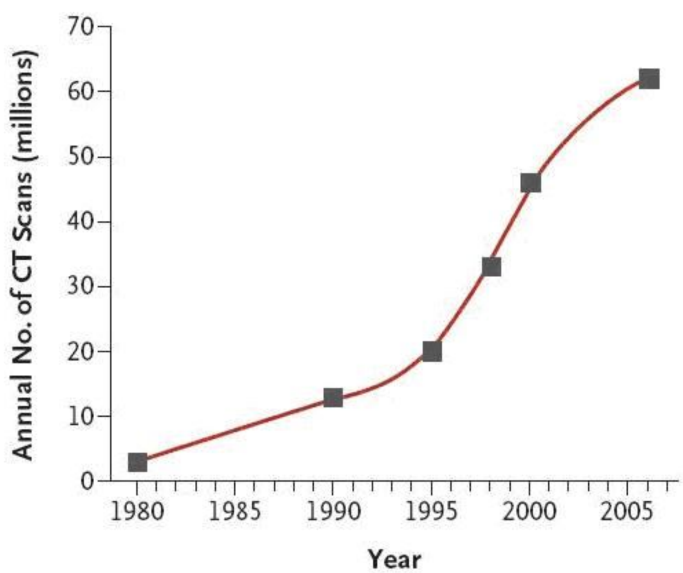

Figure 2.1. Estimated Number of CT scans performed annually in the United States (Brenner, et al., 2007)

Because a larger population is involved in X-ray CT exams, radiation exposure becomes an issue which may cause radiation-induced cancer if not properly taken care of. To solve aforementioned radiation problem, a low-dose or ultra-low-dose CT imaging device is desired. However, reducing radiation exposure of CT, i.e. lowering the current (mAs), will inevitably increase the noise level in the sinogram as well as degrade the quality of reconstructed CT images such that more and more streak artifacts near the apices of the lung become pronounced. In addition, as the new multi-slice helical CT, which has replaced conventional stop-and-shoot CT in many clinical applications, becomes widely used in recent years. Researchers (Jung, et al., 2000) have found that the radiation exposure in helical CT could be up to 4 times higher than the conventional stop-and-shoot CT. Furthermore, it has been shown (Hsieh, 1997) that the helical low-dose CT images induced non-uniform noise at a level of 10%-40% more than the conventional CT images. As a result, developing an effective approach to reduce the image noise of low-dose multi-slice helical CT becomes very important.

2.2 Literature Review

2.2.1 Overview of X-ray imaging technologies in radiology

In 1895, Röntgen discovered the first X-rays pictures which could penetrate matter. In 1901 Röntgen received the Nobel Prize for Physics, which was the first Nobel Prize in physics ever awarded. Drs. Ratcliffe and Hall Edwards first used X-ray on 13 Jan. 1896 in medical area. They show the location of a small needle in a woman's hand from X-ray image. Also in 1896 Randolph Hearst challenged scientists to capture an image of the brain. Allan Cormack and Godfrey Hounsfield built up mathematics and the first hardware implementation of the CT scanner which can image the brain in about 24 hours. As a result, Cormack and Hounsfield shared the

Nobel Price in Physiology and Medicine in 1979. (Novelline, 1997; Feynman, et al., 1963)

X-ray is electromagnetic (EM) radiation which is similar to light, TV waves, etc. Figure 2.2 illustrates some of the components of the EM spectrum including their energy, frequency and wavelength. (Dendy, 1999)

Energy (eV)	Frequency (Hz)		Wavelength (m)
4×10^{-11}	10^{4}	AM radio waves	10^{4}
4×10^{-10}	10^{5}		10^{3}
4×10^{-9}	10^{6}		10^{2}
4×10^{-8}	10^{7}	Short radio waves FM radio waves and TV	10^{1}
4×10^{-7}	10^{8}		10^{0}
4×10^{-6}	10^{9}		10^{-1}
4×10^{-5}	10^{10}	Microwaves and radar	10^{-2}
4×10^{-4}	10^{11}		10^{-3}
4×10^{-3}	10^{12}	Infrared Light	10^{-4}
4×10^{-2}	10^{13}		10^{-5}
4×10^{-1}	10^{14}	Visible Light	10^{-6}
4×10^{0}	10^{15}	Ultra-violet light	10^{-7}
4×10^{1}	10^{16}		10^{-8}
4×10^{2}	10^{17}		10^{-9}
4×10^{3}	10^{18}	X-ray	10^{-10}
4×10^{4}	10^{19}		10^{-11}
4×10^{5}	10^{20}		10^{-12}
4×10^{6}	10^{21}	Gamma ray	10^{-13}
4×10^{7}	10^{22}	Cosmic ray	10^{-14}

Figure 2.2 Electromagnetic Wave Spectrum (Dendy, 1999)

X-rays are also characterized as particles, which are called photons. If the particle energy is greater than about 1-2 eV, then the photons are capable of ionizing atoms. X-rays are ionizing radiation, and this radiation can change the chemical bonds of important substances, such as DNA. Diagnostic radiation is typically in the range of 12keV to 125keV.

There are several modes of interaction of X-rays with matter. The study of X-ray interaction is important for understanding how the image contrast is developed in medical images, and how X-ray detector works. There are five possible modes of interactions: Coherent (Rayleigh) scattering, Photoelectric effect, Compton scattering, Pair production, and Photo-disintegration. (Henke, et al., 1993) The probability of each mode is determined primarily by the energy of the incident photon and the atomic number of the item.

Coherent scattering refers to the collision of a photon with an electron after that the photon is deflected into a new direction. Little energy is lost by the low energy photon, which has insufficient energy to ionize the atom. As a result, this is not an ionizing interaction and this scattering interaction is unimportant to medical imaging (Dove, 2004; Henke, et al., 1993).

Photo-disintegration refers to nuclear reactions. The photons interact with or are absorbed by the nucleus of the target atoms. One or more nuclear particles are ejected in this photo-disintegration interaction, which makes one element becoming a different element. This elemental transformation would be extremely damaging to human tissue and this interaction can occur if the photon has a very high energy (Dove, 2004; Henke, et al., 1993).

Albert Einstein won the Nobel Prize for physics for explaining photo-electric effect modality. As an electron moves from a higher energy orbit to a low energy level, it must give up or get rid of excess energy. This process either produces photons, or the excess energy can actually cause other electrons to become free of their shells. The energy in the photons produced by this falling-down process is called fluorescent or characteristic energy. The radiation is called characteristic radiation. This process is illustrated in the Figure 2.3 (Dove, 2004; Henke, et al., 1993).

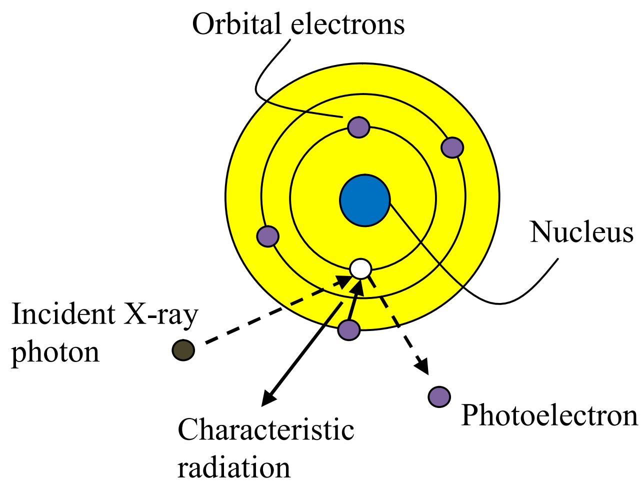

Figure 2.3 Drawing of Photoelectric effect

In Compton scattering, a photon interacts with an electron, but in contrast with the photoelectric effect, only a part of the photon energy is transferred to the electron. The photon continues on its way, but with reduced energy (i.e., a lower frequency). This is equivalent to a reduction in the momentum of the photon. The electron is still ejected from its orbit. This phenomenon is illustrated in Figure 2.4 (Dove, 2004; Henke, et al., 1993).

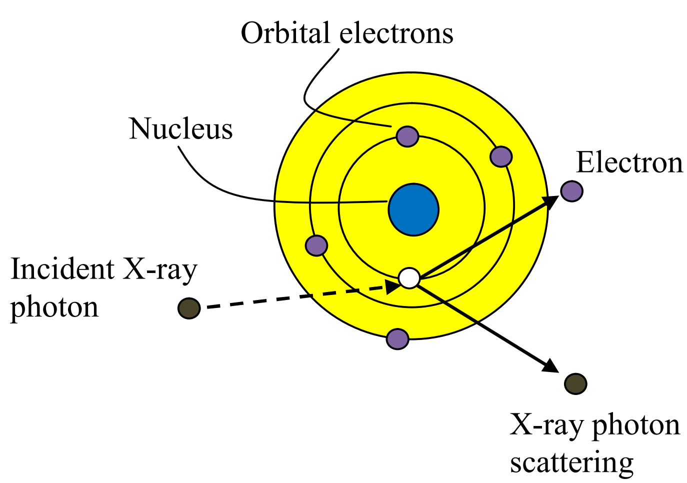

Figure 2.4 Illustration of the Compton scattering phenomenon

Pair production is characterized by a photon-nucleus interaction. In this, high-energy photons are absorbed by a nucleus; a positron (a positive electron: a form of anti-matter) is emitted along with an electron. This interaction is extremely unusual in diagnostic radiology due to the high energies required. However, pair production describes antimatter formation that is used in PET scanning (Dove, 2004; Henke, et al., 1993).

The frequency of occurrence (the probability) depends on the incident energy E, configuration of the electrons around the atom, atomic number and density of the target tissue, etc. Figure 2.5 (Dove, 2004) illustrates the relative probability of different absorption mechanisms for X-rays in carbon. Most human tissue types have similar curves. At the energy levels of most medical X-rays (50 keV to 200 keV), most of the energy absorbed by human tissue is due to the photoelectric effect. Compton Scattering is also playing an important role, which we will find adds noise to the image. Pair production occurs at energy levels that are usually out of the frequency range of medical X-rays.

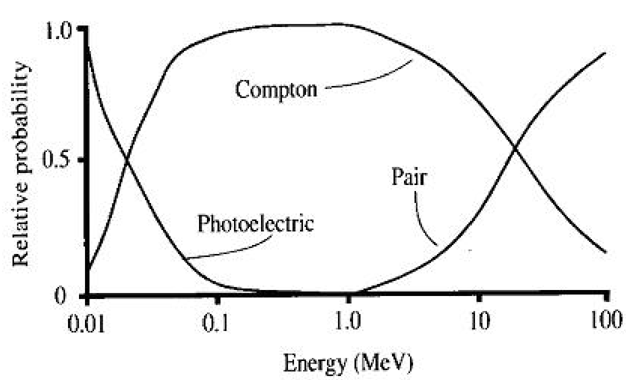

Figure 2.5 Relative probabilities of three absorption mechanisms. Low energy photons are absorbed primarily by photo-electric mechanism, high energy photons by pair production, and mid level energy photons by Compton scattering. (Dove, 2004)

2.2.2 Radiations in X-ray CT

It is necessary to measure radiation to which the subject is exposed In order to protect people from ionizing radiation and calculate the risk/benefit ratio for exposing a patient to possibly necessary radiation,. The unit of exposure used to be the roentgen (R) which was defined as “The quantity of radiation that will release an electrical charge of 2.58×10^{-4} coulombs in one kilogram of dry air”. This is equivalent to about 1.3×10^{15} electrons. So we have $1R = 2.58\times10^{-4}$ C kg^{-1} dry air.

A more useful measure is derived from the concept of radiation dose, which describes the dose of radiation absorbed by human tissue. The absorbed dose is measured in terms of the energy absorbed per unit of mass of tissue. Energy is measured in joules, and mass in kilograms. The unit of dose is the ‘gray’ (Gy) where $1Gy = 1J\ kg^{-1}$ of tissue. Absorbed dose is difficult to measure. It is first calculated by measuring the exposure and then calibrating from knowledge of mass absorption coefficients for air and tissue (Creagh and Hubbell, 1992).

Another measure is the dose equivalent, which takes into account the fact that some types of radiation are more damaging than others (Hart, et al., 2004, Larson, et al., 2007). The unit of dose equivalent is that dose that gives the same risk of damage or detriment to health whatever the type of radiation. This unit is called the sievert (Sv): $1\ Sv = 1\ J\ kg^{-1}$ tissue × constant. The constant is the radiation weight factor, which depends on the type of radiation. The radiation weighting factor for X-rays and γ-rays is 1, for neutrons the constant is 10, and for α particles the constant is 20.

Maximum permissible doses levels in various medical practices are expressed in units of dose equivalent. The International Commission on Radiological Protection

(ICRP) recommends maximum annual dose equivalent for radiation workers as 50 mSv, with a 5-year average less than 20 mSv per year. For members of the public, the recommended whole-body dose is 1 mSv averaged over 5 years (Dove, 2004). The maximum permitted dose levels have been reduced over the last 70 years. It is possible that further reduction will be made, because even small dose may have long-term effects, and these effects can only be expressed in statistical terms as the chance that a generic change or leukemia or other cancer developed (BRER, 2006). Since there are also natural causes of these changes, the assessment of risk becomes quite complicated.

A lot of research has been done about this ionizing radiation hazards to human being (Donnelly, et al., 2001; Brenner, et al., 2001, Goldman, 2007). Most of them suggest keeping the dose as low as rationally achievable, especially for the very young people. Current practice leads to tissue doses in the range of 0.1-100 mSv per examination. Nuclear medical procedures often exceed this range and procedures based on CT often exceed this range as well.

Radiation dose from CT procedures varies from patient to patient. Using the concept of effective dose equivalent allows comparison of the risk estimates associated with partial or whole-body radiation exposures. A list of representative diagnostic procedures and associated doses are given in Table 2.1 (FDA,2009). From Table 2.1, we can see organ dose from CT scanning is considerably larger than those from corresponding conventional radiography. For example, a conventional posterior-anterior abdominal X-ray examination results in a dose to the stomach of approximately 0.25 mSv, which is at least 50 times smaller than the corresponding stomach dose from an abdominal CT scan.

Table 2.1 Radiation Dose Comparison (FDA, 2009)

Diagnostic Procedure	Typical Effective Dose (mSv)	Number of Chest X-rays (PA film) for Equivalent Effective Dose	Time Period for Equivalent Effective Dose from Natural Background Radiation
Chest X-ray (PA film)	0.02	1	2.4 days
Skull x ray	0.07	4	8.5 days
Lumbar spine	1.3	65	158 days
I.V. urogram	2.5	125	304 days
Upper G.I. exam	3.0	150	1.0 year
Barium enema	7.0	350	2.3 years
CT head	2.0	100	243 days
CT abdomen	10.0	500	3.3 years

2.2.3 Factors to effect dosage of X-ray CT

The radiation doses to particular organs from any given CT study depend on X-ray beam parameters and image parameters. The X-ray beam parameters include items that can be chosen or adjusted by the technologist such as kilovoltage (kVp), which is the voltage supplied to the X-ray tube and determines how penetrating the x rays are, milliamperage (mA) which the electrical current provided to the X-ray tube and determines how many X-rays there are, filtration which is added to remove the low-energy x rays that only increase patient dose without contributing to image quality, collimation which adjust the X-ray beam to the area desired, and detection efficiency, which means how many of the x rays that "hit" the detector are "seen" by the detector. Image parameters cannot be controlled by the operator and include noise which makes the image appear "grainy", spatial resolution which measures how well the system produces images of very small objects, and slice thickness.

The most important of factors which affect the radiation dose to patient from a CT scan are the number of scans, the tube current and scanning time in milliamp-seconds (mAs), the size of the patient, the axial scan range, the scan pitch (the degree of overlap between adjacent CT slices), the tube voltage in the kilovolt peaks (kVp), and the specific design of the scanner being used. Many of these factors are under the control of the radiologist or radiology technician. A reduced mAs is the most practical means of lowering dosage due to direct proportionality between mAs and dose. It is always the case that the relative noise in CT images will increase as the radiation dose decreases, which means that there will always be a tradeoff between the need for low-noise images and the desirability of using low doses of radiation.

2.2.4 CT Images Quality

Fundamentally, image quality in CT, as in all medical imaging, depends on four basic factors: image contrast, spatial resolution, image noise and artifacts. Depending on the diagnostic task, these factors interact to determine sensitivity and visibility of details. Since we focused on the image noise issue in this research, we will discuss the CT image noise in details.

In CT, X-rays contribute to detector measurements and not to individual pixels. CT image noise is thus associated with the number of X-rays contributing to each detector measurement. How each factor in the technique affects the number of detected X-rays could be imagined to understand how CT technique affects noise. Here we take X-ray tube amperage as an example: changing the mA value changes the beam intensity and thus the number of X-rays—proportionally. Thus, doubling the mA value will double the beam intensity and the number of X-rays detected by each measurement. The scan time determines the duration of each measurement and the number of detected X-rays proportionally too. Because amperage and scan time similarly affect noise and patient dose, they are usually considered together as mA · s, or mAs.

Because CT noise appears as fluctuations in CT numbers (the density assigned to a voxel in a CT scan on an arbitrary scale on which air has a density −1000; water, 0; and compact bone +1000), a measurement of image noise is a measurement of these fluctuations, and such a measurement can be made using regions of interest (ROIs) on a scan of a uniform phantom. A statistical ROI function (available on most CT scanners) allows users to place a rectangular or oval ROI on the image, within which is calculated the average and standard deviation (SD) of the CT numbers for the enclosed pixels. The SD indicates the magnitude of random fluctuations in the CT number and thus is related to noise: The larger the SD, the higher the image noise. Another measurement of image noise is to use a control image as standard, and calculate the mean square error (MSE) of the target image with that control image for the each pixel in the image. In this research, we select the standard dose CT image of the same subject which was taken at the same time with the ultra-low-dose CT image as our control.

However, the above two measurements are all objective methods. The most valuable measurements of the image noise level, especially the quality of whole image to the clinics, would be opinions from the radiologists, which is a subjective CT image quality evaluation method. In this research we developed a comparative evaluation system which involved the radiologists as evaluators to evaluate the CT images quality. This evaluation system will be introduced in details in the later section.

2.2.5 Current Low-dose X-ray CT image restoration techniques and their limitations

During last several years, much effort has been made by the researchers to suppress the noise induced streak artifacts in low-dose CT, even in ultra low-dose CT. Their work can be summarized as the following three aspects.

One straightforward strategy is to deal with the reconstructed CT images directly. A sophisticated linear or non-linear filter is usually used by to reduce the noise level in the reconstructed image domain. Sauer et al. (Sauer, et al., 1991) designed a set of nonstationary filters by minimizing the image degradation measured by a combination of noise power and resolution loss, and the set of filters were tuned to local noise autocorrelation functions in the reconstructed tomographic images. Finally, the associated optimization problem could be expressed in terms of a simple matrix norm with linear constraints. Kalra et al. (Kalra, et al., 2003) evaluated the low-dose abdomen CT image quality with specified six noise reduction filters in image domain. These six filters were classified by GE Medical Systems as normal-low filter, normal-medium filter, normal-high filter, special-low filter, special-medium filter and special-high filter. Results based on seven patients showed the use of noise reduction filters in image domain was effective in reducing the noise in the CT images acquired with 50% reduction in radiation dose. Although the tomographic image based noise reduction approaches are quite straightforward and fairly easy to implement, the performances of such methods are not very promising, which is expectable since the noise properties from the projection data (the source) as well as the sinogram to CT image reconstruction are not fully explored by only focusing on the recovered image domain.

Another approach is to focus on the reconstruction process by improving a statistic based reconstruction algorithm through a cost function such that the noise level can be suppressed during the sinogram to tomographic recovery. Fessler (Fessler, 1994) presented an image reconstruction method for PET images based on a penalized, weighted least-squares (PWLS) objective with the nonnegative successive over-relaxation algorithm (PWLS +SOR). Both the quantitative and qualitative results showed that the proposed method had better performance in terms of the noise reduction comparing to the traditional ML-EM or FBP approaches. In the work of Elbakri and Fessler (Elbakri, et al., 2002; Elbakri, et al., 2003), the detected photon numbers were considered as a compound Poisson instead of the traditional Poisson distribution. By doing so, the authors indicated that a more realistic polyenergetic model could be built to reduce the noise caused by beam hardening or low-dose imaging. Given the compound Poisson model, a penalized likelihood approach was used to estimate the image densities during the sinogram to image reconstruction. Cheng et al. (Cheng, et al., 2006) proposed a fast two-step iterative strategy for the low-dose CT reconstruction. The two-step iterative approach included the adaptive filtering in the image space as well as the discrepancy minimization in the Radon space. Experimental results showed that the optimal iteration step size could be achieved according to the proposed method. The disadvantage of aforementioned statistical image reconstruction approaches is that it requires an accurate or realistic statistical model, which is often unattainable, of the whole system behavior. Therefore, modeling itself becomes a very challenging task. In addition, the noise associated with the projection data are still not well taken care of by the methods in this category.

To overcome previous mentioned disadvantages, a more intuitive way is to address the noise issue directly from the source – the projection data or sinogram space. Recently more and more attentions have been paid to such sinogram based noise reduction approaches. The basic idea of the methods following in this category is to model the noise characteristic by a cost function in the sinogram space, and then remove the noise through a corresponding filter or filters. Once the noise in the projection data is eliminated, the traditional CT reconstruction approaches can be used to build the tomographical images. Hsieh (Hsieh, 1998) introduced an adaptive filtering approach in the sinogram domain to reduce the streak artifact in CT images. The adaptive filtering was achieved by dynamically adjusting the smoothing operations according to the local noise characteristics. The results showed the proposed method was effective in the quantum noise reduction, and had minimum impact on the spatial resolution. Lu et al. (Lu, et al., 2002) found the calibrated low-dose CT sinogram data follow approximately the Gaussian distribution with a nonlinear dependence between the sample mean and sample variance. Based on this model, they proposed a penalized weighted least square (PWLS) optimization procedure on both the K-L (Karhunen-Loeve) transformed and non K-L transformed sinogram data. By doing so, the noise level of the sinogram space was effectively reduced, and hence the image quality of reconstructed CT images could be improved. According to the previously mentioned noise model, Li et al. (Li, et al., 2004) also proposed a nonlinear sinogram smoothing method for low-dose X-ray CT. They applied Maximum-A-Posteriori (MAP) probability estimation to maximize a penalized likelihood which resulted in a set of nonlinear object functions. An iterated conditional model (ICM) was then employed to achieve a local maximal solution during a rational computing time. La Rivière and Pan (La Rivière, et al., 2000) developed a nonparametric sinogram smoothing approach for emission tomography using penalized Poisson-likelihood functions to smooth the projection data. Three link functions were also investigated in their study in order to achieve better resolution-noise tradeoffs. Recently, La Rivière (La Rivière, et al., 2005) introduced an approximate compound Poisson likelihood function, which was the combination of Poisson and Gaussian distribution, to replace the assumed noise distribution. The author also extended spline-based penalized likelihood approach to a more generalized one so that the overall performance in terms of the noise reduction could be improved. Not like image based noise reduction approach, the sinogram based method directly deals with the noise source, and hence has better performance in terms of noise reduction. It is also more computationally efficient than the statistical reconstruction in the image space.

Although more and more efforts have been made to the sinogram based noise reduction in the low-dose CT research, most of such researches are focused on the conventional stop-and-shoot CT, and still deal with one-dimensional projection profile. As for multi-slice helical CT, the projection data among adjacent detectors or channels is highly correlated, making it feasible to model the projection data and hence suppress the noise in the sinogram of multi-slice helical low-dose CT through a 2D signal processing method. Wang et al. (Wang, et al., 2006) applied Karhunen–Loéve (KL) transform along the axial direction to address the associated correlation among adjacent projection data. A penalized weighted least-squares (PWLS) solution was then proposed in the KL domain as a SNR-adaptive noise reduction scheme. The experiment results showed the KL-PWLS noise-reduction method could efficiently restore large volume helical CT sinograms. Although this method considered the correlation along the axial direction, it was applied for single-slice helical CT.

The objective of this research is to decrease the noise levels and streak artifacts in multi-slice low-dose helical CT images, and to find an alternative way to reconstruct the CT image from multi-slice low-dose helical CT sinogram. In this chapter, a 2D block based nonparametric smoothing model with thin plate splines and the roughness penalty is introduced to restore the multi-slice helical low-dose CT raw data. Each projection panel was first divided into blocks, and then, the 2D data in each local block was fitted to a thin-plate smoothing splines' surface by minimizing a roughness-penalized least squares objective function. By doing so, the noise in each low-dose CT projection was reduced by leveraging the information contained not only within each individual projection profile, but also among nearby profiles. Finally the image reconstruction was fulfilled by standard filtered back projection (FBP) algorithm. The reconstructed images as well as both objective and subjective evaluations will be given in the results and discussions section to show the effectiveness of proposed approach. Although the proposed approach was used for the multi-slice helical CT, it can be equally applied to single-slice helical or conventional stop-and-shoot CT.

2.3 Ultra-low-dose CT system

The ultra-low-dose CT raw data were acquired through Siemens SOMATOM Sensation 16-Slice helical CT provided by VA Maryland Health Care System, Baltimore. The pixel pitch of CT scanner is 1.5mm along 16 module row direction with 0.4mm between rows at a speed of 0.4 second per rotation. Radius of the focal spot circle is 570mm and the scanner is operated in non-FFS mode with tube angle increment is about 0.31 degree. Patients with different ages and genders were scanned with z-position covered from about 85mm to 400mm by the Sensation 16 under both conventional dose (120 kVp/119 mAs) and ultra-low dose (120 kVp/10 mAs) protocols. All other settings were the same in both scans. The scanned raw data were obtained after logarithmic transform and system calibrations according to equation (2.1).

$$I_C = m_0 \log \frac{I}{I_0} \tag{2.1}$$

where I_C is the calibrated intensity, I_0 and I stands for the primary and attenuated intensities respectively. $m_0 < 0$ is a calibration constant. Notably, I is always smaller than I_0, since it is the "leftover" radiation after the main beam X-ray I_0 penetrates through the human body. Therefore, the bigger the I_C value is, the thicker or denser the human body that X-ray passes through.

2.4 Methods

Nonparametric regression, especially the roughness penalty based nonparametric regression, has received an upsurge of interest in general area of curve or surface estimation in statistics. Previous researchers (Li, et al., 2004) has proved that the noise model in low-dose CT projection profiles after system calibration follow a Gaussian distribution and stated the roughness penalty based nonparametric regression has been one of the most optimal choice in low-dose CT projection profile smoothing. As for multi-slice helical CT, the aforementioned work has been extended into 3D analysis (Jiang, et al., 2007c) of low-dose CT projection cube as shown in figure 2.6, where *X* axis is the detector row coordinates, *Y* axis is the detector channel coordinates, and *Z* axis is X-ray tube rotation angle.

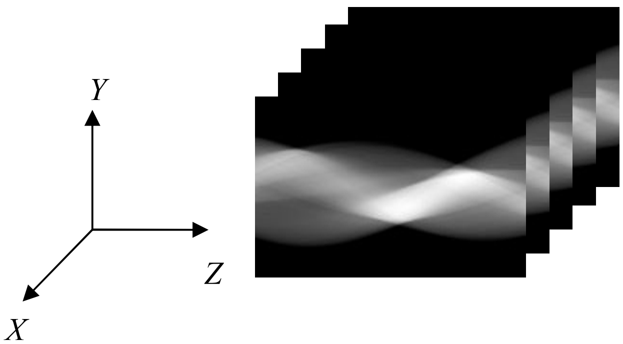

Figure 2.6. 3D low-dose multi-slice helical CT projection data.

A natural generalization of smoothing splines, which is called thin plate splines in equation (2.2), was applied to 3D sinogram cubic.

$$g(x,y,z)=\sum_{i=1}^{n}c_i\phi\left(\sqrt{(x-X_i)^2+(y-Y_i)^2+(z-Z_i)^2}\right) \tag{2.2}$$

Where $\{(X_i,Y_i,Z_i)|i=1,2,...,n\}$ is a set of control point in the cube, and the kernel function ϕ is thin plate splines radial basis function, c_i is a set of parameters to be determined.

Given data values Y_i at the point $P(x_i, y_i, z_i)$ in 3D projection, where x_i is the detector row coordinates at point P, y_i is the detector channel coordinates at point P, and z_i is the index of X-ray tube rotation angle at point P. The penalized residual sum of squares of a surface g (Green, et al., 1994) can be defined in equation (2.3):

$$S(g)=\sum_{i}\{Y_i-g(x_i,y_i,z)\}^2+\alpha J(g) \tag{2.3}$$

and

$$J(g)=\iint_{\Re^2}\left\{\left(\frac{\partial^2 g(x,y,z)}{\partial x^2}\right)^2+2\left(\frac{\partial^2 g(x,y,z)}{\partial x\partial y}\right)^2+\left(\frac{\partial^2 g(x,y,z)}{\partial y^2}\right)^2\right\}dxdy \tag{2.4}$$

where R^2 is an infinite region. The same as in one dimension, the function *S(g)* combines a term quantifying the lack of fit of surface *g* to the data and a roughness penalty term *J(g)*. α >0 is a smoothing parameter. The penalized least squares estimator $\hat{g}$ is defined as the minimum of the function *S(g)* over the class of all twice-differentiable function *g*.

$$\hat{g}(x,y,z)=\arg\min_g S(g) \tag{2.5}$$

Wahba (Wahba, et al., 1990) has proved that the local minimization solution of equation (2.3) is unique. Furthermore, thin plate splines has a nice property that it can always be decomposed into a global affine and a local non-affine component. Plus, the separation of the affine and non-affine warping space can be done by QR decomposition. The optimized parameters $\hat{c}$ in thin plate splines can be solved through applying Tikhonov regularization to the decomposed penalized least squared cost function.

Although the 2D thin plate splines utilize the information both within each single projection profile and among nearby profiles so that the better results can be obtained comparing to the 1D cubic splines based smoothing, the computation time of proposed 2D thin plate splines smoothing is quite demanding. To solve this problem, the block based processing scheme was used instead of applying the thin plate splines to the entire sinogram data.

The flow chart of blocked based nonparametric thin plate splines smoothing algorithm for low-dose multi-slice helical CT is given in Figure 2.7. The implementation procedure of the smoothing scheme can also be summarized as following four steps:

Step 1: Dividing the original multi-slice low-dose CT sinogram into N frames with each frame corresponding to each X-ray tube rotation angle;

Step 2: Dividing each frame into M fitting blocks with block size $B \times B$;

Step 3: Computing the local minimal solution of equation (2.2) to do the surface smoothing in each block;

Step 4: Applying filtered back projection (FBP) algorithm to the smoothed multi-slice CT sinogram to reconstruct CT images.

Given restored ultra-low-dose CT sinogram, the B10f filtered back projection (FBP) reconstruction kernel which was provided by Siemens Medical Solutions was applied in this research. In order to show the effectiveness of proposed approach, the adaptive filtering option, which was included in the reconstruction kernel, was turned off during the study.

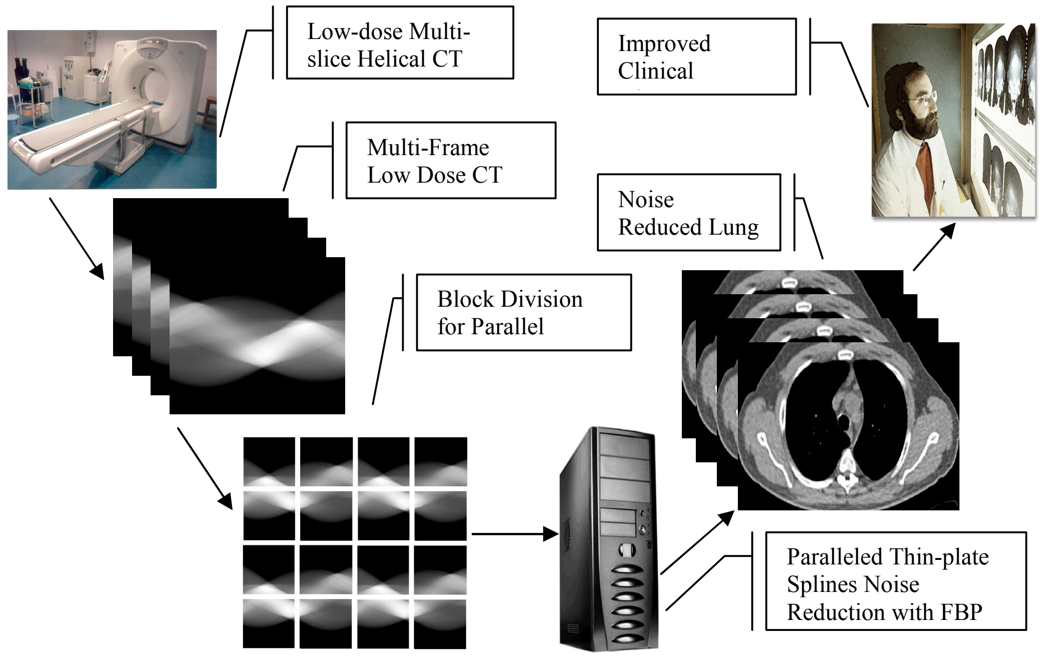

Figure 2.7 Flow chart of blocked nonparametric thin plate splines smoothing algorithm.

2.5 Results and Discussions

Patient thorax CT scan data with ultra-low-dose (10 mAs) sinogram were studied in this research. The conventional CT (119 mAs) data at same body position were also acquired for reference purposes. Three patients including two males and one females, with different ages range from 50 to 80 were enrolled into this research. Each patient was scanned twice under different settings with fixed body position. Figure 2.8 presents the single projection profile for conventional CT raw data (red), ultra-low-dose CT raw data (blue), nonparametric cubic spline smoothed CT data (green) and nonparametric thin-plate splines smoothed CT data (black). According to equation (2.1), the higher value of calibrated detector reading is in Figure 2.8, the thicker or denser body part presents. Therefore, the noise in the ultra-low dose CT data (blue) mainly come from the thick/dense body part, which is expectable due to the photon starvation phenomenon in the low-dose CT imaging. By comparing the three low-dose CT profiles, it can be seen that both of the nonparametric smoothing methods works very well in terms of noise reduction. Some details around the peak area are also reserved by aforementioned two approaches. However, it is hard to tell the difference between two nonparametric based smoothing methods by simply looking at the Figure 2.8(c) and 2.8(d). Further comparisons as well as the quantitative analysis are necessary.

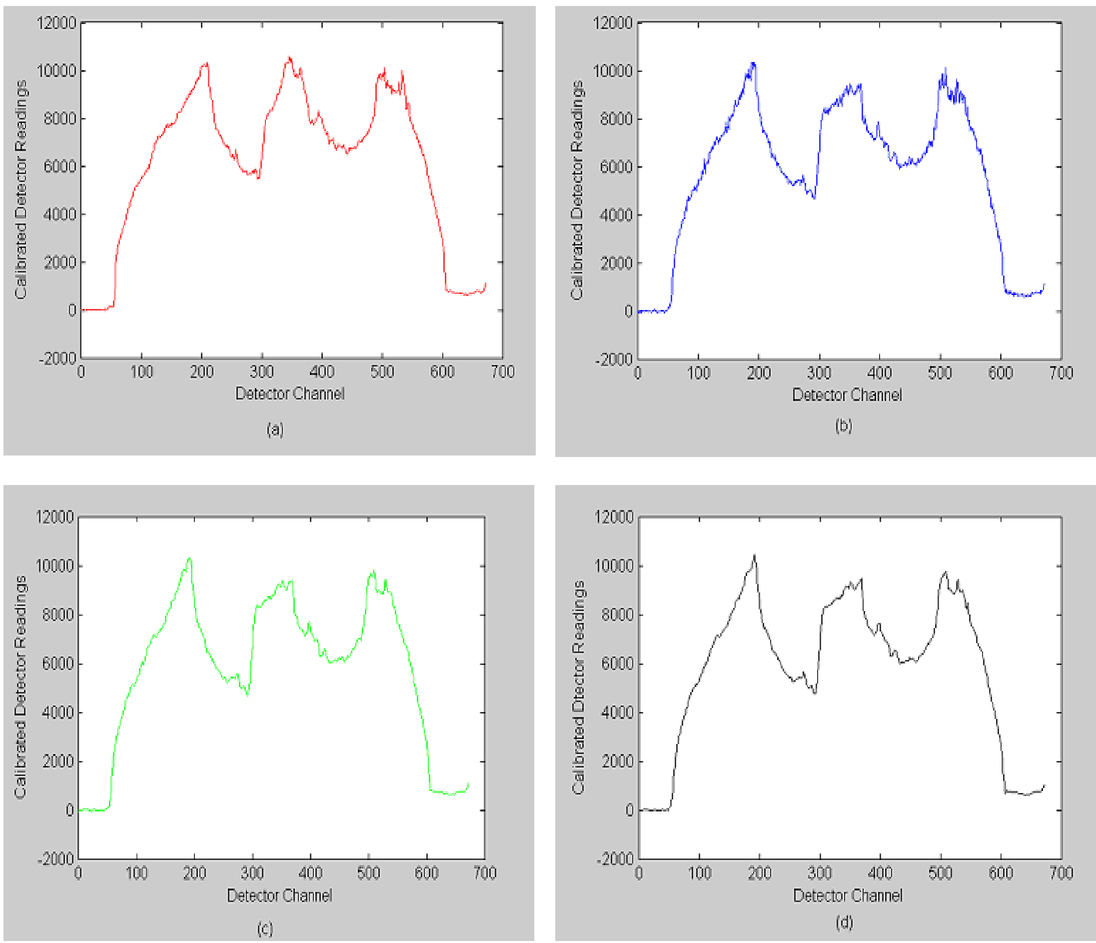

Figure 2.8. One projection profile in (a) conventional CT data; (b) low-dose CT data; (c) nonparametric cubic spline smoothed CT data; (d) nonparametric thin-plate splines smoothed CT data.

In order to further evaluate the performance of proposed approach, the 2D original and processed sinogram CT data are given in the Figure 2.9. Seen from

Figure 2.9, the conventional CT sinogram (a) seems much smoother, and has the better resolution than the original ultra-low-dose CT sonogram (b). This is expectable since the low-dose data have the increased noise level, and hence the degraded sinogram image quality. The two restored sinograms (c) and (d) have less noise than the original low-dose CT sinogram, which show the effectiveness of the smoothing methods. Furthermore, the restored CT sinogram with thin-plate splines (d) has better resolution than the one smoothed with cubic spline (c), especially in some bright area indicated by the red arrows in Figure 2.9. Given the four sinograms, it is obvious that the proposed smoothing method gives the best resolution referring to the conventional CT sinogram (a), and the original low-dose data have the worst resolution.

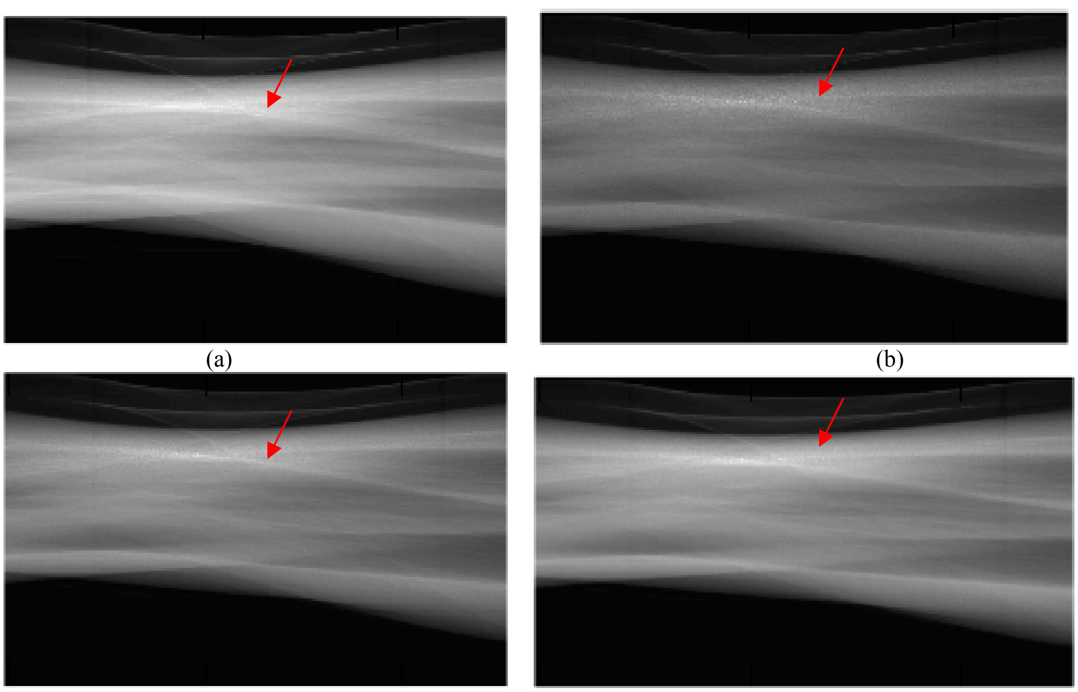
(a) (b)
(c) (d)

Figure 2.9 Multi-slice CT sinogram in one row: (a) Conventional CT sinogram; (b) Low-dose CT sinogram; (c) Restored CT sinogram by nonparametric cubic smoothing spline; (d) Restored CT sinogram by blocked nonparametric thin-plate smoothing splines.

Two different display window levels are used in this research, including both mediastinal display window and lung parenchymal display window. Mediastinal display window is a display setting with 350 HU wide at the center of 75 HU, and this display window is used to evaluate the quality of muscle area in CT images. Lung parenchymal display window is a display setting with 2200 HU wide at the center of -500 HU, and this display window is utilized to assess the quality of lung area in CT images. Figure 2.10 and 2.11 demonstrate the same reconstructed images in mediastial display window and lung parenchymal display window, respectively.

Figure 2.10 demonstrates the final reconstructed images in mediastinal (window width, 350 HU/center, 75 HU) display window levels, from (a) conventional CT sinogram, (b) original ultra-low-dose CT sinogram, (c) restored CT sinogram smoothed with cubic spline and (d) restored CT sinogram smoothed with thin-plate splines, respectively. It is obvious that the conventional CT image shows highest image quality among all the recovered images, and the original ultra-low-dose CT image gives the poorest image quality with a lot of streak artifacts and lowest contrast. Both smoothed images shown in (c) and (d) have better image quality than the original ultra-low-dose image. They successfully suppress the streak artifacts presented in the image (b). However, the cubic spline smoothed image looks blurrier than the thin-plate smoothed one, especially around the muscle conjunction area indicated by the yellow arrow. Actually the better contrast around aforementioned conjunction area is clinically very meaningful, since they play an important role during some CT image guided operations. In addition, the noise level in the cubic spline smoothed image seems higher than the thin-plate smoothed one, which clearly indicates that the proposed approach can reduce more noise than the conventional cubic spline based smoothing.

Another very interesting phenomena, which can be observed by comparing the conventional CT image with the nonparametric thin-plate splines restored image, is that the conventional CT image may also present some streak artifacts around bone area, which is indicated by the red arrow. However, in the nonparametric thin-plate splines restored image, those streak artifacts become invisible, which can be considered a positive byproduct of proposed method.

Similarly, the same images are shown in lung parenchymal(window width, 2200 HU/center, –500 HU) window settings in Figure 2.11, the streak artifacts are significantly reduced by proposed approach Figure 2.11(d) comparing to Figure 2.11(b) and (c). Figure 2.11 (d) also has the better resolution in the lung areas comparing to Figure 2.11 (c) processed by traditional method.

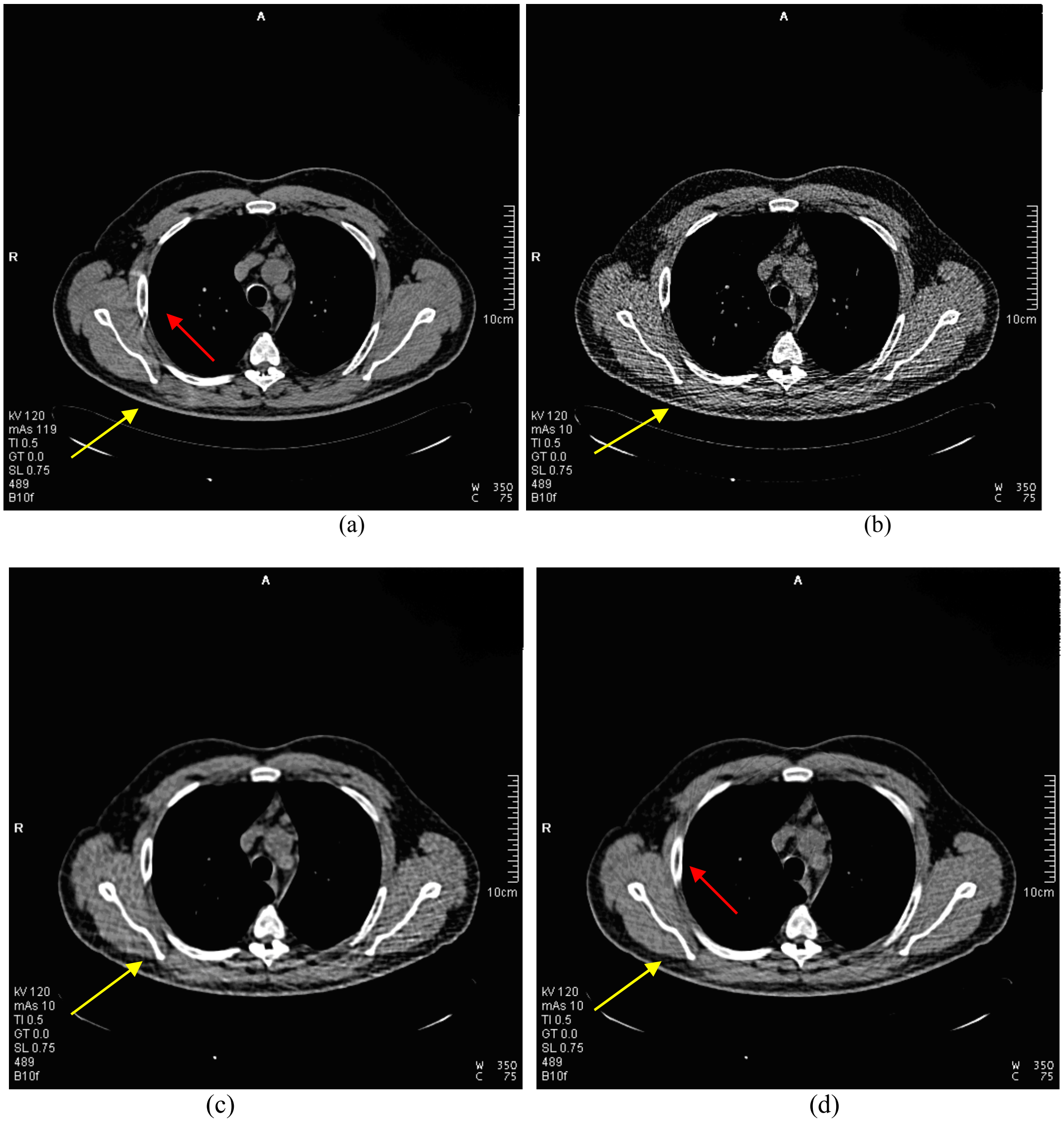

Figure 2.10 Reconstructed image in mediastinal display window: (a) Conventional CT reconstructed image; (b) Low-dose CT reconstructed image; (c) Reconstructed image from restored CT sinogram by nonparametric cubic smoothing spline; (d) Reconstructed image from restored CT sinogram by blocked nonparametric thin-plate smoothing splines.

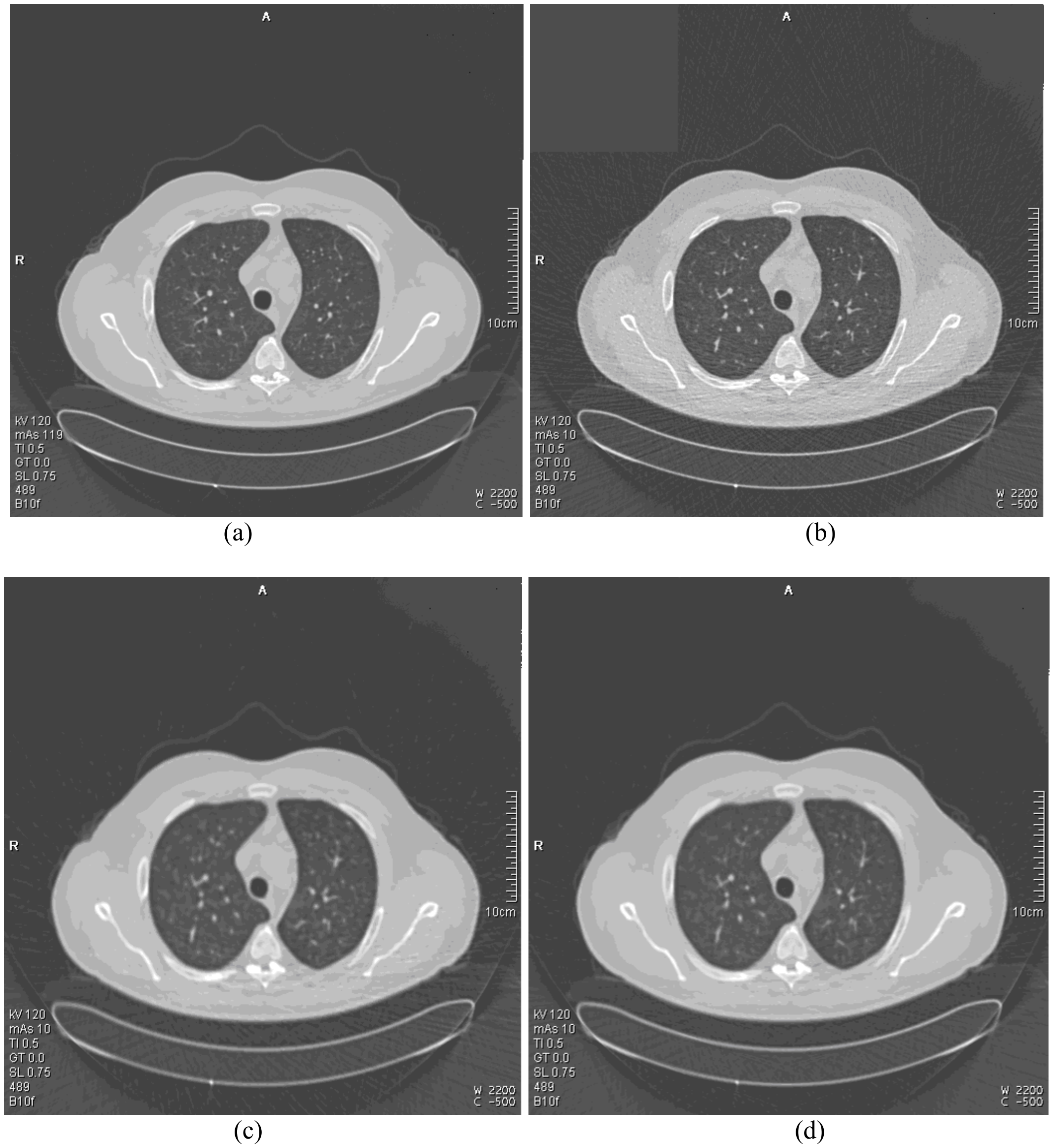

Figure 2.11 Reconstructed image in lung parenchymal display window: (a) Conventional CT reconstructed image; (b) Low-dose CT reconstructed image; (c) Reconstructed image from restored CT sinogram by nonparametric cubic smoothing spline; (d) Reconstructed image from restored CT sinogram by blocked nonparametric thin-plate smoothing splines.

To quantitatively evaluate the performance of proposed approach, the mean squared error (*MSE*) was also computed for all three low-dose sinograms according to the equation (2.6):

$$MSE = \frac{\sum_{c=1}^{C}\sum_{r=1}^{R}(S(r,c) - S_{REF}(r,c))^2}{R \times C} \tag{2.6}$$

where S refers to the low-dose sinogram image, S_{REF} is the reference sinogram image, which is the conventional CT data in this research, and R, C stand for the row and column size of the sinogram image respectively. The computed *MSE* value is given in Figure 2.12:

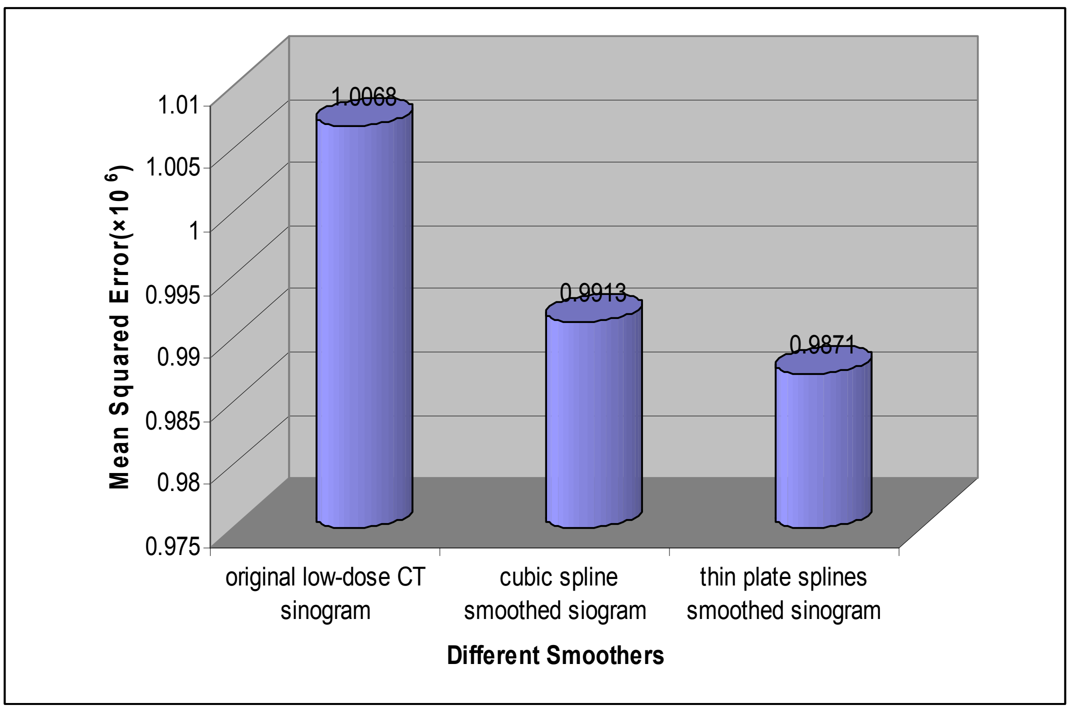

Figure 2.12 MSE value of three low-dose CT sinogram data.

According to Figure 2.12, the proposed method has the lowest mean squared error comparing to the other two low-dose data, and the original low-dose CT sinogram has the highest *MSE*.

Although the better sinogram data can be restored from original ultra-low-dose data according to the proposed 2D thin-plate based approach, it does not guarantee a better reconstructed CT image in a clinical point of view. In order to show the effectiveness of proposed method, Figure 2.13 calculated the *MSE* between the final reconstructed CT images under difference smoothing strategies and the conventional dose CT images. Obviously, original low dose CT reconstructed image has the highest *MSE* among all the methods. And the proposed non-parametric blocked thin plate smoothing splines method has the lowest *MSE* than the others.

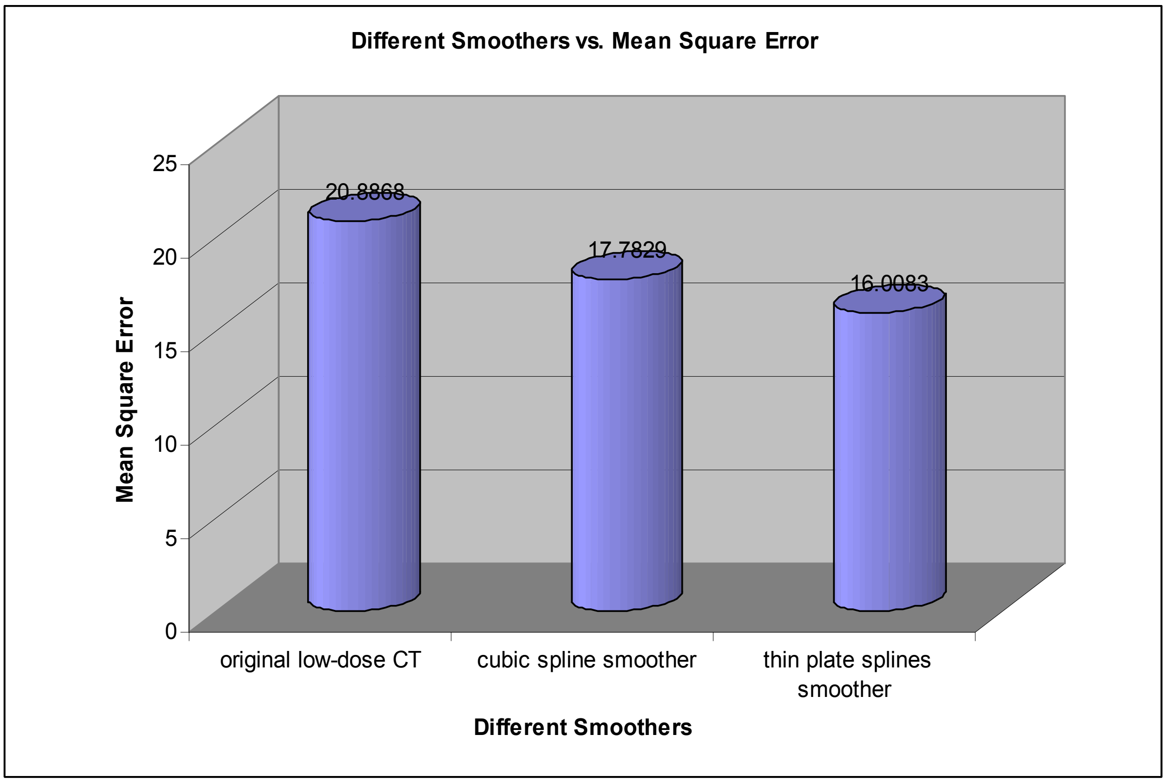

Figure 2.13 Different Smoothers vs. Mean Squared Error for reconstructed image.

Besides the objective evaluation, the experimental results were also evaluated subjectively from clinical aspect by experts (Jiang, et al., 2007d) such as radiologists in the hospital. In this research, total 23 experts were enrolled in the subjective evaluation study, including 7 faculties, 6 fellows and 10 residents at the Radiology Department of Medical School, University of Maryland. The average age of these experts is 33. The detailed composition of the evaluation experts including 2 females and 21 males is shown in Figure 2.14.

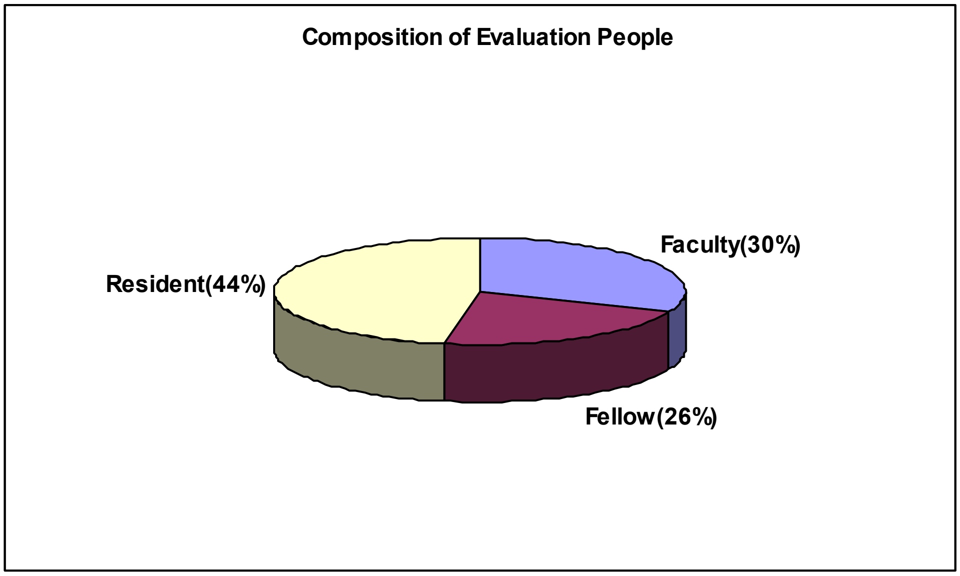

Figure 2.14 Composition of the test subjective group.

The raw data were processed by the two different methods: traditional nonparametric roughness penalized least squares regression with cubic smoothing spline (CSS) method and the proposed blocked roughness penalized least squares regression with thin-plate splines (TSS) method. 2500 pairs of ultra-low-dose CT images were reconstructed by FBP method from the smoothed sinograms and viewed in both mediastinal (window width, 350 HU/center, 75 HU) and lung parenchymal (window width, 2200 HU/center, –500 HU) window settings. 50 pairs of images were randomly selected (25 pairs with mediastinal and 25 pairs with lung parenchymal window settings). The experts were asked to compare the image pairs reconstructed by both CSS and TSS smoothed sinograms, which are CSS-IM and TSS-IM respectively, on the following five questions:

1. Which of the images do you prefer with regard to overall image quality?

2. Which image is superior for review of the lungs?

3. Which image is superior for review of the muscles?

4. Which image has less streak artifacts?

5. Which image has less noise?

The experts must choose one of the following three answers to each question given above:

1. First image* is preferred.

2. Second image* is preferred.

3. No difference.

* Note: The order of each image pair was also randomly provided. In other words, given an image pair, whether the first image was processed by TSS or CSS approach was randomly determined, and such information was not available to the experts who did the evaluation.

The web address of our ultra-low-dose CT images quality evaluation study is http://lowdose.skullone.net. Some of the web pages are shown in the supplemental A. (Figure S1 and Figure S2)

Figure 2.15 and Figure 2.16 show all the evaluation results to the aforementioned five different questions in mediastinal display window and lung parenchymal display window, respectively. It is obvious that the dominant responses preferred the proposed TSS approach in terms of better overall image quality (Question 1), less streak artifacts (Question 4) and less image noise (Question 5) under both display window settings. For question 2, 93.2% of the total responses considered there were no differences between TSS and CSS processed ultra-low-dose

CT images under mediastinal display window setting. This is expectable because mediastinal display window usually focuses on the muscle and bone areas which have much higher image intensity values than the lung tissue. As a result, the lung under mediastinal display window setting will become black, and hence unobservable. When the reconstructed images were reviewed under lung parenchymal display window setting, the lung turned to be visible, and the majority responses (60.6% comparing to 15.5%) preferred the proposed method for reviewing lungs. Similarly, under lung parenchymal display window setting, the bone and muscle areas become saturated, and hence are not feasible for the evaluation. Therefore, 59.7% responses considered there were no differences between the reconstructed images under two approaches. However, if the bone and muscle are evaluated under mediastinal display window setting, 91.9% of the total responses preferred proposed TSS method.

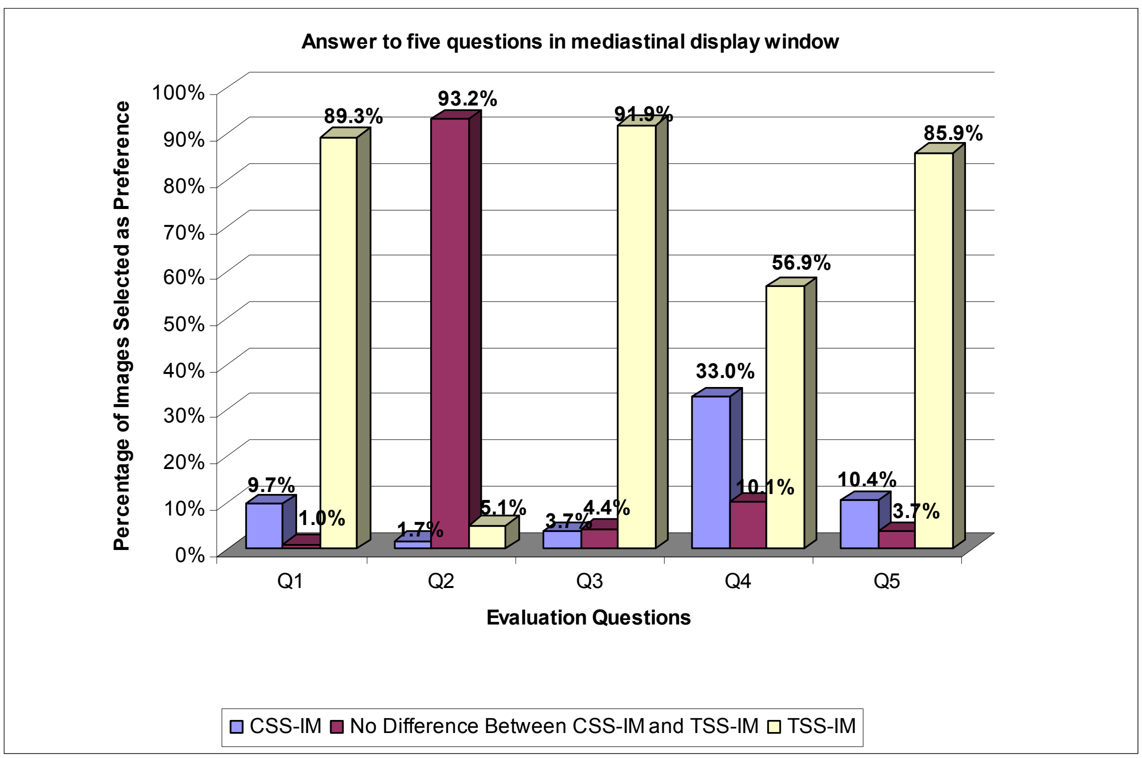

Figure 2.15 Experts answers to five questions in mediastinal display window.

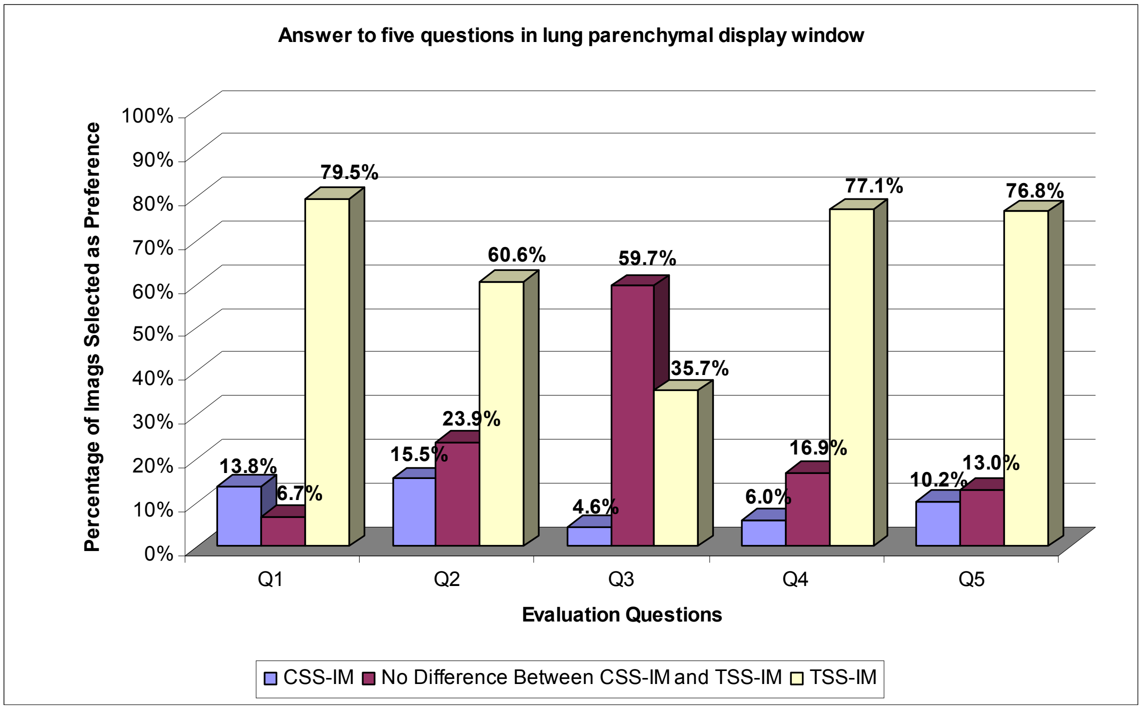

Figure 2.16 Experts answers to five questions in lung parenchymal display window.

To further evaluate the consistency of the test results under two different window settings, the average percentages of TSS-IM images selected as the preference in two different display window sizes were fed into one-way ANOVA statistical analysis for the comparison purposes. Table 2.2 shows the one-way ANOVA results. The large p-value of 0.9572 indicates that differences between the mean percentages of TSS-IM images selected as the preference in two different display window sizes are not significant (above 95% confident). The test therefore strongly supports the null hypothesis which is there are no significant differences between mean percentages of TSS-IM images selected as the preference given two display window sizes.

Table 2.2 ANOVA table for comparing means of percentage of TSS-IM images as preference in two different display window sizes.

Source	SS	DF	MS	F	Prob.> F
Groups	5.8039e-005	1	5.8039e-005	0.0029134	0.95724
Error	0.75701	38	0.019921		
Total	0.75706	39			

Figure 2.17 shows the box plot of aforementioned ANOVA test graphically. The lower and upper lines of the "box" are the 25th and 75th percentiles of the data. The distance between the top and bottom of the box is the interquartile range. The red line in the middle of the box is the data median. Seen from figure 2.17, the medians of the data in both display windows are almost the same, which is consistent with results of ANOVA. For both display windows, the median of the data is not centered in the box, which indicates some skewness of the data. The whiskers show the extent of the rest of the data except outliers. The red plus sign at the top of the plot indicates there is an outlier in the data for mediastinal display window.

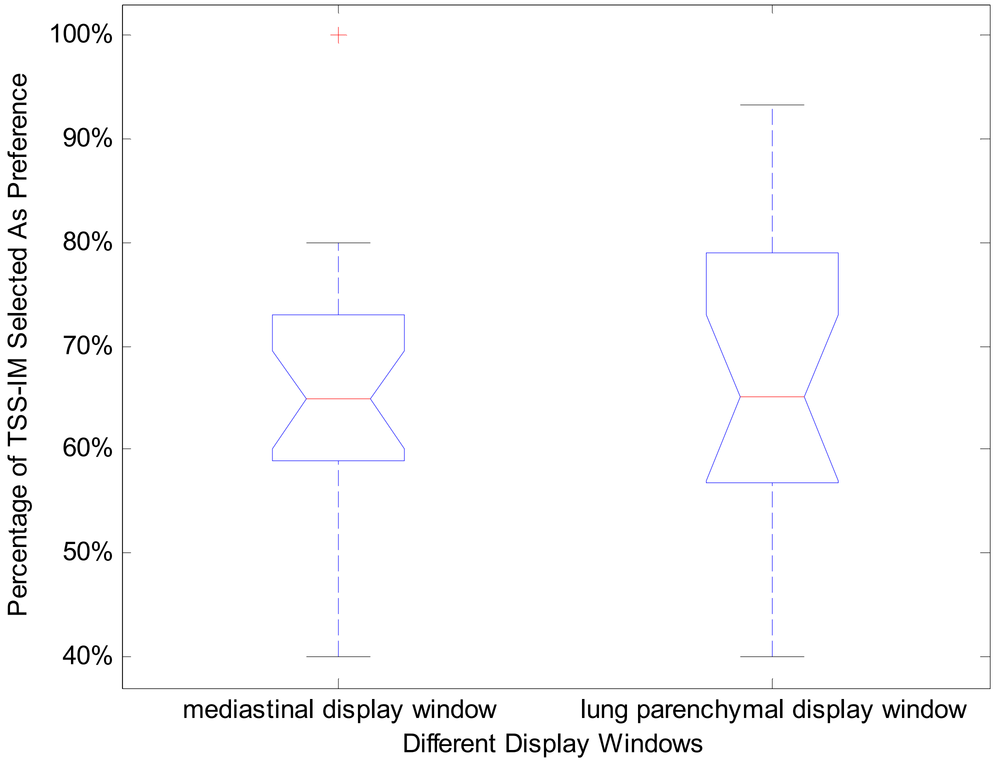

Figure 2.17 Plot box of percentage of TSS-IM selected as preference in two different display windows.

As a result, radiologists preferred TSS processed ultra-low-dose CT images of the thorax in terms of all five preset criteria including whole image quality, lung quality, muscle quality, streak artifacts and noise level in comparison with the traditional CSS-IM. These results demonstrate the proposed novel TSS sinogram restoration approach produces improved subjective image quality in comparison to the traditional CSS method.

2.6 Conclusions

In this research, a nonparametric smoothing method with thin plate smoothing splines and the roughness penalty was proposed to restore the ultra-low-dose CT raw data acquired under 119 kVp and 10 mAs protocols. Each projection frame was firstly divided into blocks, and then 2D block data were fitted to a thin-plate smoothing spline surface by minimizing a roughness-penalized least squares objective function. The results showed the effectiveness of proposed approach, which not only suppressed the noises presented in the original ultra-low-dose sinogram, but also preserved the valid high frequency information, such as boundaries, etc. An objective comparison between proposed method and the conventional 1D sinogram based cubic spline smoothing approach was conducted. The results favor the proposed method, which gave a reconstructed CT image with better contrast and less noise comparing to the 1D based approach. Furthermore, a subjective comparison between the proposed method and the 1D cubic spline smoothing approach was also performed. Radiologists strongly preferred TSS-IM images of the thorax in terms of whole image quality, lung quality, muscle quality, streak artifacts and noise level in comparison with traditional method.

3 Walnut Shell and Meat Classification in Hyperspectral Fluorescence Imagery

3.1 Introduction

The Eastern black walnut, which was found growing throughout the central and eastern parts of the U.S., has a rich and distinctive flavor and is often used as an additive in value-added foods. There are approximately over 15.4 million acres of black walnut with each acre producing about 1000 to 1700 pounds of raw nuts in the U.S (Hatcher, 1998; Jones, 1998). However, only about 20 millions pounds of the raw Eastern black walnuts are commercially processed every year (Hammons Products Company, 1998). The reason that growers were not motivated to process the nuts is that the raw nuts usually are sold to the nut processors for \$0.08 per pound and there is not enough nut processing capacity available in the U.S. The growers can gain satisfactory economic benefit if they can process the raw nut themselves. The current market price of the black walnut meat is about \$12 and up per pound depending on the quality and physical size of the meat (Hammons, 2008). The black walnut shell is especially hard and hazardous to the consumer if it is mixed with or un-separated from meat in the walnut processing plant. In the current walnut processing plant, after cracking and removing the majority of shells by air lathe, the plant workers remove any remaining shells by hand in order to reach the required quality level. Therefore, developing an automated walnuts shell fragments detection system becomes necessary.

3.2 Literature Review

3.2.1 Overview of walnuts shell fragments detection

Due to the restricted USDA standard, most of walnuts cracking work is done by a cracker and sorted by hands. That's very labor demanding and inefficient. Currently, walnut cracking machines remove the majority of shells by air lathe, and human intervention is still necessary to manually pick up the walnut shell fragments in order to reach the strict government regulations. This is a very eye-demanding and difficult process because shell and meat fragments can be very similar in size and color (Krishnan and Berlage, 1984). Therefore, there is a need to develop an effective method to discriminate the walnut shell from the meat.

3.2.2 Current walnuts shell fragments detection techniques and their limitations

A lot of efforts have been made by researchers in order to separate the walnuts, almonds, and other kind of nut meat from shells since the last century. As shown in Figure 3.1, Krishnan and Berlage (1984) investigated the feasibility of using iron powder and magnetic fluid to remove shells from walnut meat. In this work, two coating materials (iron powder and magnetic fluid) for the walnuts were used and compared. The coated nuts were cracked in a commercial nut cracker and then were conditioned over the permanent magnetic drum separator. Their research indicated that the method was successful in removing the shell fragments from nut meat. However, this method cannot be adopted by the industry immediately since both coating materials require Food and Drug Administration approval as food additives.

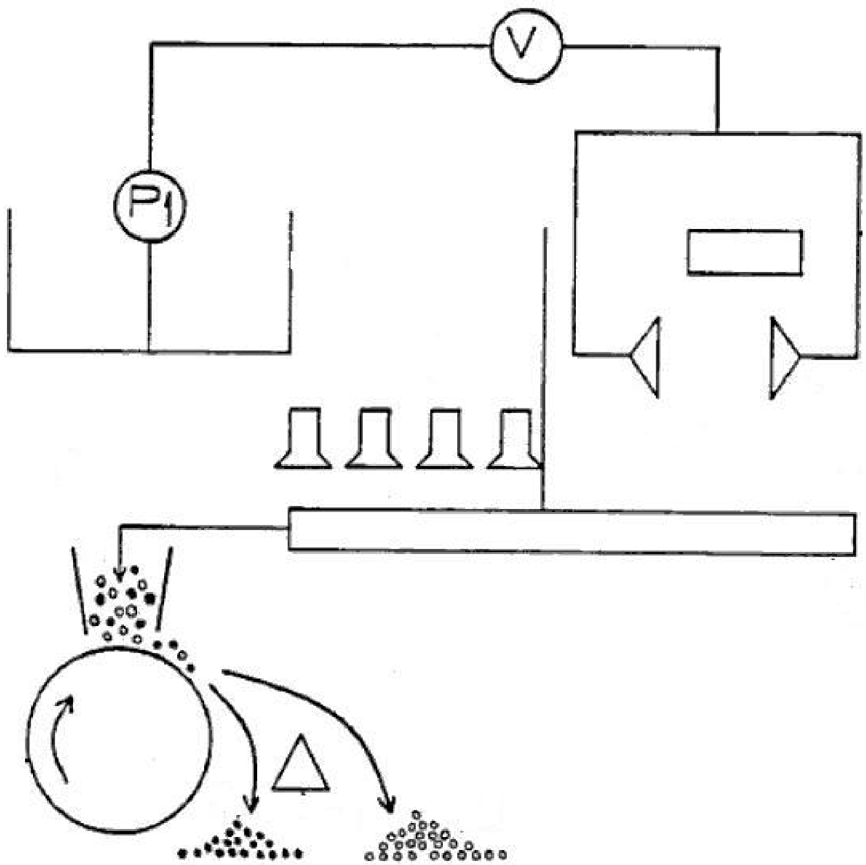

Figure 3.1. Schematic drawings of system which applied iron powder and magnetic fluid based coating materials to remove shells from walnut meat (Patent number: 4765486). A method for obtaining a purified fraction from a mixture using a magnetic fluid wherein the mixture is contacted with the magnetic fluid to preferentially absorb the fluid onto selected components so they become magnetized and the magnetic components in the so-contacted mixture are separated from the nonmagnetic components by passing the mixture through a magnetic field.

A noticeable study was presented by Pearson and Young (2002) who tried to automatically sort almonds with embedded shells by laser transmittance imaging (Figure 3.2). Their research work was based on the fact that a shell fragment blocks the laser ray while the almond meats don't. The shell fragments could be detected as dark pixels in the image. However, this method cannot be applied to walnut meat and shell separation because walnut meat is thicker than the almond, and laser light may not pass through the meat even when no shell fragments are present. Some other imaging techniques have also been used to separate the shell and meat for almond, but are not widely used for walnuts. Even for the almond meat and shell differentiation, some shells could be falsely classified as meat and vice versa, i.e., the false alarm rate is very high. Therefore, an accurate method needs to be developed to discriminate the shell from the meat, particularly for black walnut.

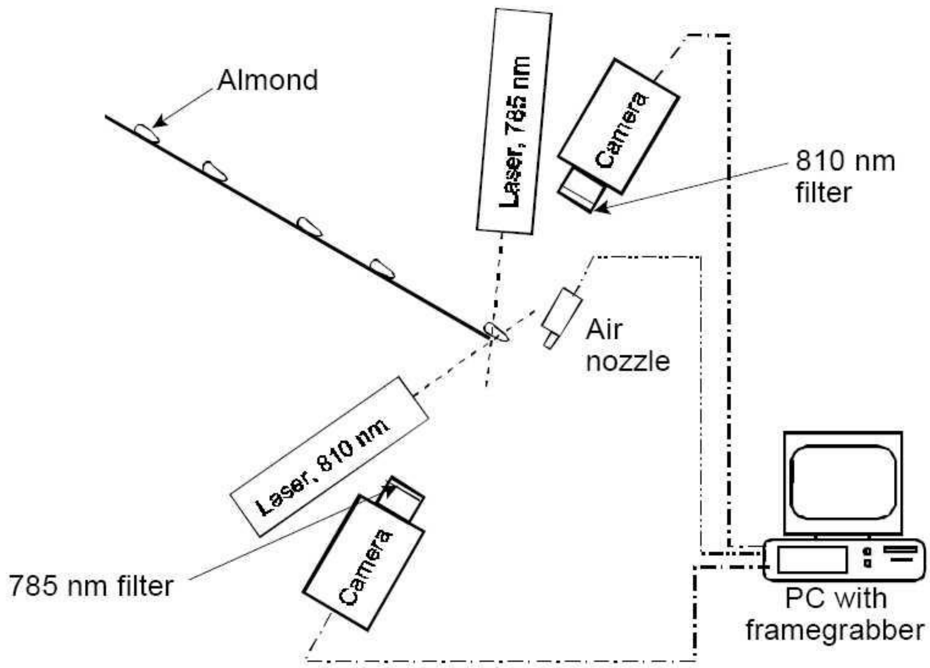

Figure 3.2. Schematic of laser transmittance imaging system. A sorting system using two lasers and two cameras was developed to detect almond kernels with embedded shell. The lasers used were 1000mW near infrared diode lasers. These lasers emitted light at 785 nm and 810 nm respectively. The cameras were fitted with optical bandpass filters matching the emission wavelength of the corresponding laser on the opposite side of the kernel from the camera. With this arrangement, reflected light was rejected and only light transmitted through the kernel was imaged.

3.2.3 Hyperspectral imaging technology and its applications

Machine vision technology can not only illustrate geometric and statistical features, but also represent chemical ingredient characteristic of an object. This technology has been widely used in quality and safety inspection of agricultural products such as fruit (Zhu, et al., 2005; Zhu, et al., 2007; Wen and Tao, 2000) and poultry meat (Chen, et al., 2003; Jing and Tao, 2001; Chao, et al., 2002). Hyperspectral imaging has been paid more attention in the food processing and inspection fields in the last several years. Kim, et al. (2001) designed a hyperspectral reflectance and fluorescence imaging system, with high spatial and spectral resolution, for food quality and safety inspection. Park, et al. (2001) developed a hyperspectral imaging system to detect fecal and ingesta contamination on poultry carcasses. Yao, et al. (2001) used an aerial hyperspectral imaging system in the precision farming field, and the goal of their work was to calibrate the geometric distortions in the whole system. Other researchers have investigated the feasibility of hyperspectral imaging technology for agricultural applications from the software analysis point of views. Lu (2003) used two different apple cultivars to study the potential of near-infrared (NIR) hyperspectral imaging to detect bruises on apples. The principal component and minimum noise fraction transforms were used in the data analysis. Vargas, et al. (2004a) used a hyperspectral imaging system to detect animal fecal contamination on cantaloupes and strawberries. Results showed that fluorescence images at 680 nm exhibited the greatest contrast between contaminated and uncontaminated surfaces. For cantaloupes and strawberries, the detection rates could be improved by using ratio images of 560 nm/660 nm and 745 nm/680 nm, respectively. Cheng, et al. (2004) presented a novel method that combined principal component analysis (PCA) and Fisher's linear discriminate (FLD) method to show that the hybrid PCA-FLD method maximized the representation and classification effects on the extracted new feature bands. Based on experiments of different types of samples, the new hybrid PCA-FLD method performed better than both individual PCA and FLD methods for inspecting cucumber chilling damage under reflective hyperspectral imagery. Park, et al. (2002) applied visible/NIR spectroscopy to detect fecal and ingesta contaminants on the poultry carcasses. Principal component analysis was used to select four most important spectra (434, 517, 565, and 628 nm) to detect fecal and ingesta contaminants on hyperspectral imagery. Band ratios of dual wavelength (565 nm/517 nm) images and histogram stretching were applied in the experiment. Results showed that the detection rate could reach up to 100% by nonlinear histogram stretching. Hyperspectral imaging has also been shown to be a powerful technique in many other research fields such as remote sensing and medical diagnosis (Chang, et al., 2004; Cohen, et al., 1999; Zuzak, et al., 1999; Casasent, et al., 2004).

Notable research can also be found in the area of hyperspectral fluorescence imaging for food processing purposes. Vargas, et al. (2004b) used a hyperspectral fluorescence imaging system to evaluate the potential for detection of animal fecal contamination on cantaloupes and strawberries. Kim, et al. (2002) evaluated the use of fluorescence imaging techniques to detect fecal contamination on apple surfaces. Experimental results showed that multispectral fluorescence techniques at four bands (450, 530, 685, and 735nm) were the optimum spectrum to detect fecal contamination on apple surfaces, and the simple band ratio could reduce the variation in normal apple surfaces while accentuating differences between contaminated and uncontaminated areas.

To solve aforementioned challenging walnuts shell fragments detection problem, both hyperspectral and fluorescence imaging technologies were combined together, and such combination was found to be very effective to differentiate walnuts shell and meat target given precise spectral information. The motivation of using hyperspectral fluorescence imaging technique mainly came from the following two facts:

1. The fluorescence imaging technique is powerful in chemical component identification (Lakowicz, 1999; Haugland, 1996). Fluorescence occurs when a certain wavelength light hits an object with fluorescent components. The emitted light has the spectrum and intensity that is related to its composition. Because the nut meat and the shell are of different chemical compositions, and the nut meat appears much more sensitive to the fluorescence spectra than the shell, the fluorescence imaging method can be effective and accurate in discriminating the shell fragments from nut meat.
2. For a specific subject, the image information at a large number of spectra can be acquired simultaneously using hyperspectral imaging technology. With such rich hyperspectral information, it is possible to gain otherwise unavailable insights into the chemical and/or physical characteristics of the subject.

3.3 Hyperspectral Fluorescence Imaging System for Walnuts Shell Fragments Detection

The image data was obtained by a hyperspectral imaging system (Figure 3.3a) which was developed by Instrumentation and Sensing Laboratory (ISL) at USDA (Kim, et al., 2001). Figure 3.3b shows a block diagram of the hyperspectral imaging system.

The whole system is divided into three modules: the sensor module, optics module, and lighting and sample module. The sensor module includes a back-illuminated CCD camera with 512×512 pixel resolution and a control unit that interfaces with a personal computer. The optics module includes a spectrograph with a prism-grating-prism (PGP) construction and a C-mount lens, which is attached to the CCD camera head. The function of the optic module is to disperse incoming light into a spectral-spatial matrix and let the light matrix into the CCD. Two different illumination sources are included in the third module: two line lights with two 150W halogen lamps transmitted by two rectilinear fiber bundles to supply near uniform sample illumination; and two UV-A line fluorescent lamps (365 nm at peak) with low-pass filters in front to eliminate spectral contamination by pseudo-fluorescence. In this research, the fluorescent lamp based illumination source was used and the images were captured line by line as a tray incrementally moved the samples past the field of view of the electron multiplying CCD camera under UV light at wavelengths ranging from 425nm to 775nm with 4.5nm increments. The image data acquired by the hyperspectral imaging system were arranged as a three-dimensional image cube, with two spatial dimensions and one spectral dimension.

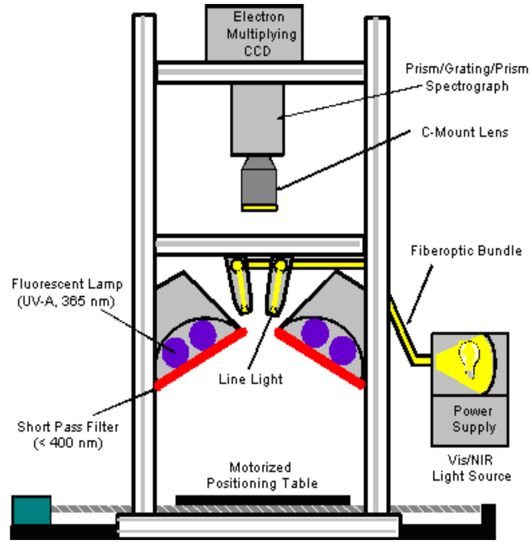

(a) Hyperspectral imaging system (b) Block diagram

Figure 3.3 Hyperspectral imaging system developed at the Instrumentation and Sensing Laboratory at the United States Department of Agriculture in Beltsville, MD.

3.4 Materials and Methods

3.4.1 Image acquisition

The intact black walnuts of both two-year and one-year old after harvest were provided by the USDA Agriculture Marketing Servies. Each intact walnut was cracked by a hammer, and a total of four categories based on different sample conditions were considered, which were light meat, dark meat, inner shell and outer shell. Figure 3.4 shows the RGB images of each category. Light meat refers to the innermost part of the meat that is very light in color (Figure 3.4(a)). Dark meat means the meat with a dark skin (Figure 3.4(b)). Inner shell (Figure 3.4(c)) refers to the in side of the nut shell, and outer shell (Figure 3.4(d)) refers to the out side of the shell. The inner shell is often lighter and smoother compared to the outer shell.

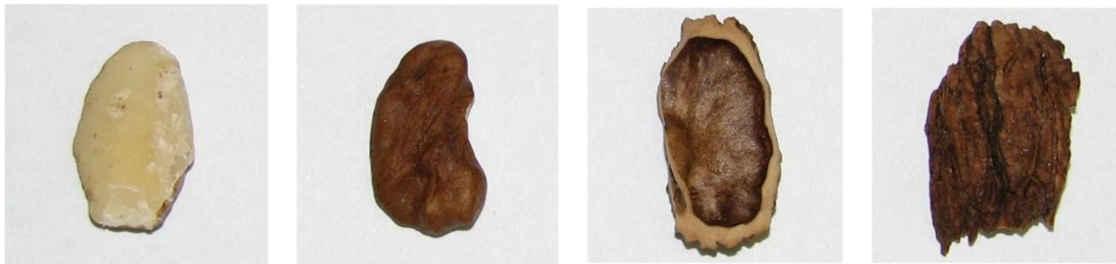

(a) (b) (c) (d)

Figure 3.4. Color images of each category. Light meat refers to the innermost part of the meat that is very light in color (a). Dark meat means the meat with a dark skin (b). Inner shell (c) refers to the in side of the nut shell, and outer shell (d) refers to the out side of the shell. The inner shell is often lighter and smoother comparing to the outer shell.

Samples were scanned by a hyperspectral fluorescent imaging system developed by the Instrumentation and Sensing Laboratory (ISL) at USDA (Kim, et al., 2001). Figure 3.3(a) shows the block diagram of the whole hyperspectral imaging system. Hyperspectral fluorescence images were taken at 79 different fluorescence wavelengths ranging from 425 nm to 745 nm at the 4.5nm increments. The calibrated images were captured line by line as a tray incrementally moved the samples past the field of view of the CCD camera under UV light. The spectral used in this research were based on each pixel in region of interest (ROI) which was segmented by the image processing software. The image data acquired by the hyperspectral imaging system were arranged as a three-dimensional image cube, with two spatial dimensions and one spectral dimension, as shown in Figure 3.5.

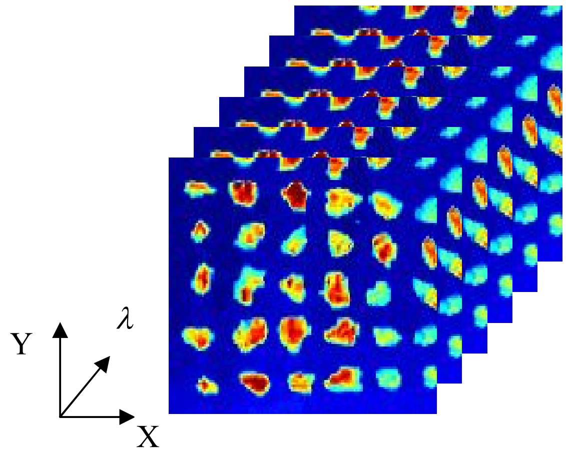

Figure 3.5 A typical image cube acquired by hyperspectral imager, with two spatial dimensions and one spectral dimension (X, Y, λ).

3.4.2 Feature Extraction

In hyperspectral image analysis, the dimension of the data is high (For example, in this research, total 79 dimension/wavebands data need to be analyzed). As a result, it is necessary to reduce the redundant information of the data and efficiently represent the structure of data. As a classical projection based method, principal component analysis (PCA) (Campbell, 2002; Fukunaga, 1990) is often used for the feature selection and data dimension reduction. The PCA approach can be formulated as the following: Let S_T be the covariance matrix of the hyperspectral samples, which is:

$$S_T = \frac{1}{n}\sum_{k=1}^{n}(x_k - \boldsymbol{\mu})(x_k - \boldsymbol{\mu})^T \tag{3.1}$$

where S_T is an N by N covariance matrix, x_k is an N-dimensional hyperspectral grayscale vector, μ is the sample's mean vector, and n is the total number of training samples. In PCA the projection $\boldsymbol{\eta}_{opt}$ is chosen to maximize the determinant of the total covariance matrix of the projected samples. That is

$$\boldsymbol{\eta}_{opt} = \arg\max_{\eta} \left| \boldsymbol{\eta}^T S_T \boldsymbol{\eta} \right| = [\eta_1\, \eta_2 \ldots \eta_m] \tag{3.2}$$

where $\{\eta_i \mid i = 1,2,\ldots,m\}$ is the set of N-dimensional eigenvector of S_T corresponding to the m largest eigenvalues (Fukunaga, 1990). In general the eigenvectors of S_T corresponding to the first three largest eigenvalues have preserved more than 90% energy of the whole dataset. However, the selection of the parameter m is still an important challenge because the performance of the classifier becomes better and better as the principal components increase to some extent, on the other hand, the computation time also increases as the number of principal components used increases. As a result, there is a tradeoff among the number of selected principal components, the performance of classifier and the computation time.

3.4.3 Gaussian Mixture Model

Mixture models, such as Gaussian Mixture Model (GMM) (Duda, et al., 2001), have been widely used in many data modeling applications such as time series classification (Povinelli, et al., 2004), and image texture detection (Permuter, et al., 2006), etc. The key points of Gaussian Mixture Model are the following: Firstly, GMM assumes that each class-conditional probability density is subject to Gaussian distributions with different parameters. Secondly, under Gaussian Mixture model, the feature points from each specific object or class are generated from a pool of Gaussian models with different prior mixture weights.

Let the complete input data set be: $D=\{(x_1,y_1),(x_2,y_2)\ldots(x_n, y_n)\}$, which contains both vectors of observations $x_i \in R^N$ and its corresponding class label $y_i \in \{1,2,\ldots c\}$, where R^N refers to the N-dimensional space of the observations, and c stands for the total number of classes, the j^{th} class-conditional probability density can be written as $p(x|y_j,\theta_j)$, which is subject to multivariate Gaussian distribution with the parameter $\theta_j = \{u_j, \Sigma_j\}$, where u_j is the mean vector, and Σ_j is the covariance matrix. Assume the input data was obtained by selecting a state of nature (class) y_j with prior probability $P(y_j)$, the probability density function of the input data x is given by

$$p(x|\theta) = \sum_{j=1}^{c} p(x|y_j,\theta_j)P(y_j) \tag{3.3}$$

Equation (3.3) is called mixture density, and $p(x|y_j,\theta_j)$ is named the component density. The multivariate Gaussian probability density function in the N-dimensional space can be written as

$$p(x|y_j,\theta_j) = \frac{1}{(2\pi)^{N/2}|\Sigma_j|^{1/2}}\exp[-\frac{1}{2}(x-\mu_j)^T\Sigma^{-1}(x-\mu_j)] \tag{3.4}$$

In Gaussian Mixture model, both θ_j and $P(y_j)$ are unknowns and need to be estimated. A maximum-likelihood estimate approach was used to determine above mentioned parameters θ_j and $P(y_j)$. Assume the input data are sampled from random variables which are independent and identically distributed (i.i.d.), the likelihood function, which is the joint density of input data, can be expressed as

$$p(D|\theta) \equiv \prod_{i=1}^{n} p(x_i|\theta) \tag{3.5}$$

Taking log transform on both sides of equation (3.5), the log-likelihood can be written as:

$$l = \sum_{i=1}^{n} \ln p(x_i|\theta) \tag{3.6}$$

The maximum-likelihood estimates of θ and $P(y_j)$, which are $\hat{\theta}$ and $\hat{P}(y_j)$ respectively, can be defined as

$$\hat{\theta} = \arg\max_{\theta\in\Theta} l = \arg\max_{\theta\in\Theta} \sum_{i=1}^{n} \ln p(x_i|\theta)$$

$$\text{Subject to: } \hat{P}(y_i) \geq 0 \text{ and } \sum_{i=1}^{c} \hat{P}(y_i) = 1\,. \tag{3.7}$$

An expectation-maximization algorithm (EM) (Hogg, et al., 2005; Dempster, et al., 1977) was applied to solve the maximum-likelihood estimation problem.

3.4.4. Bayesian Minimum Risk Classifier

Given an appropriate data model, a classifier is then needed in order to do the discrimination among classes. The Bayesian minimum risk classifier (Duda, et al., 2001; Langley, et al., 1992; Fukunaga, 1990), which deals with the problem in making optimal decisions in pattern recognition, is employed in this research. Bayesian classifier is used to categorize testing data into given classes such that the total expected risk is minimized. In Gaussian Mixture model, once the maximum-likelihood estimate is used, both the prior probabilities $P(y_j)$ and the class-conditional probability density $p(x|y_j)$ are known. According to Bayesian rule, the posteriori probability $p(y_i|x)$ is given by

$$p(y_i \mid x) = \frac{p(x \mid y_j)P(y_i)}{\sum_{j=1}^{c} p(x \mid y_j)P(y_j)} \tag{3.8}$$

The expected loss (i.e. the risk) associated with taking action α_k is defined as:

$$\Re(\alpha_k \mid x) = \sum_{i=1}^{c} \Gamma(\alpha_k \mid y_i)P(y_i \mid x) \tag{3.9}$$

where $\Gamma(\alpha_k \mid y_i)$ is the loss function, which stands for the loss incurred for taking action α_k when the state of nature is y_i. So the overall expected risk is written as

$$\Re = \int \Re(\alpha(x) \mid x)p(x)dx \tag{3.10}$$

It is easy to show that the minimum overall risk, also called Bayes risk, is:

$$\Re^* = \min_{\alpha_k} \Re(\alpha_k \mid x) \tag{3.11}$$

The 0-1 loss function was used in this study, which means

$$\Gamma(\alpha_k \mid y_i) = \begin{cases} 0 & k = i \\ 1 & k \neq i \end{cases} \qquad i, k = 1, \ldots\ldots c \tag{3.12}$$

Then, the Bayesian risk can be given through the following equation:

$$\Re(\alpha_k \mid x) = 1 - P(y_i \mid x) \tag{3.13}$$

So the final minimum-risk Bayesian decision rule becomes:

$$d(x) = \arg\max_{y_i \in \{1,2,\ldots c\}} p(y_i \mid x) \tag{3.14}$$

where *d(x)* refers to the predicted class label of sample *x*.

3.4.5 Cross-Validation

In order to evaluate the performance of the classifier, the Cross-validation (Duda, et al., 2001; Goutte, 1997; Zhu and Rohwer, 1996) technique, which is widely used in pattern recognition field, was applied in this research. More specifically, the *l-folds* cross-validation technique was used in the experiment. This technique randomly divided the experimental data into l disjoint sets of equal size n/l, where n was the total number of samples in the dataset. Then, $l-1$ data sets were selected as the training set to estimate the model parameters in the classifier. The remaining data set called validation set was used to calculate the generalization error. The above procedure was then repeated $l-1$ times, each time with a different set held out as a validation set. The estimated performance of the classifier was computed as the mean of these l errors. In this research, cross-validation was used not only to estimate the optimal number of components m in PCA feature extraction, but also to evaluate the performance of the whole classification strategy.

In order to determine the optimal parameter m as mentioned in section 3.4.2, the number of folds in cross-validation was set to a fixed value. Given different parameter m, the total classification error e would be different, and the optimum parameter m^* was selected by minimizing the total classification error $e(m)$, i.e.

$$m^* = \arg\min_m e(m) \tag{3.15}$$

3.4.6 Implementation of PCA-GMM based Bayesian classification

The flow chart of proposed PCA-GMM approach was given in figure 3.6. The procedure of the PCA-GMM based Bayesian classification can also be summarized as following steps:

Step 1: Using PCA to do the feature extraction according to equation (3.2);

Step 2: Estimating the parameters of Gaussian mixture model according to equation (3.7);

Step 3: Computing the decision boundary using Bayesian minimum risk classification rule according to equation (3.14);

Step 4: Categorizing the test data based on decision boundary provided by step 3.

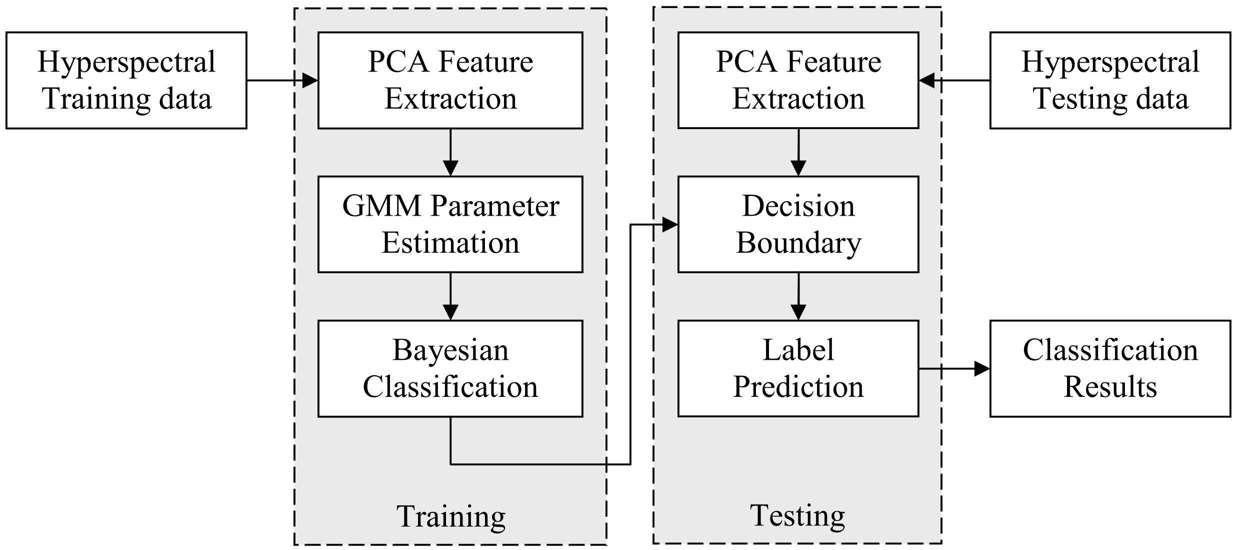

Figure 3.6 Flow Chart of PCA-GMM based Bayesian classification. Basically it include two phases: one is training phase, the other one is testing phase.

3.4.7 Kernel Function and Support Vector Machine (SVM) Classifiers

As a statistical learning method in data mining (Duda, et al., 2001; Fukunaga, 1990), Support Vector Machine (Burges, 1998) has been applied in applications such as object recognition (Guo, et. al, 2000) and face detection (Osuna, et. al, 1997). The basic idea of SVM is to find the optimal hyperplane as a decision surface that correctly separates the largest fraction of data points while maximizing the margins from the hyperplane to each class. The simplest support vector machine classifier is also called a maximal margin classifier. This approach is designed to overcome the specific characteristic of hyperspectral images, which are high number of spectral channels and relative few numbers of labeled training samples.

The optimal hyperplane, *h*, that is searched in the input space can be defined by equation (3.16):

$$h = \Omega^T x + b \tag{3.16}$$

where x is the input vector, Ω is the adaptable weight vector, *b* is the bias, and T is the transpose operator.

Another advantage of SVM is that the above mentioned maximization problem can be solved in any high-dimensional space other than the original input space by introducing a kernel function. The principle of the kernel method was addressed by Cover's theorem on separability of patterns (Cortes and Vapnik, 1995). The probability that the feature space is linear separable becomes higher when the low-dimensional input space is nonlinearly transformed into a high-dimensional feature space. Theoretically, the kernel function is able to implicitly and not explicitly map the input space, which may not be linearly separable, into an arbitrary high-dimensional feature space that can be linearly separable. In other words, the computation of the kernel method becomes possible in high-dimensional space, since it computes the inner product as a direct function of the input space without explicitly computing the mapping.

Suppose the input space vector $x_i \in \Re^n$ ($i = 1,...l$) with its corresponding class label $y_i \in \{-1, 1\}$ in the two-class case, *l* is the number of total input data. Cortes and Vapnik (1995) showed the above maximization problem was equal to solve the following primal convex problem:

$$\min_{\Omega,b,\xi} \ \frac{1}{2}\Omega^T\Omega + C\sum_{i=1}^{l}\xi_i$$

$$\textit{Subject to} \quad y_i(\Omega^T\phi(x_i)+b) \ge 1-\xi_i \qquad \xi_i \ge 0, \quad i=1,...l. \qquad (3.17)$$

where ξ_i is the slack variable, *C* is a user-specified positive parameter, and Ω is the weight vector. By mapping function ϕ, the input vector x_i is mapped from the input space $\Re^n$ into a higher dimensional feature space *F*. Thus, its corresponding dual problem is:

$$\min_{\alpha}\frac{1}{2}\alpha^T Q\alpha - e^T\alpha \qquad 0 \le \alpha \le C,\ i=1,...,l,$$

$$\textit{Subject to} \qquad y^T\alpha = 0, \qquad (3.18)$$

where *e* is the vector of all ones, *Q* is an *l* by *l* positive semi-definite matrix and can be defined as:

$$Q_{ij} = y_i y_j K(x_{i,}x_j) \qquad (3.19)$$

where $K(x_i,x_j) \equiv \phi(x_i)^T\phi(x_j)$ is the kernel matrix calculated by a specified kernel function $k(x,y)$. α can be obtained by solving this dual problem.

In general, three common kernel functions (Table 3.1), which allow one to compute the value of the inner product in feature space *F* without having to carry out the mapping ϕ, are widely used in SVM. In these functions, *d* is the degree of freedom of polynomial kernel, σ is a parameter related to the width of Gaussian kernel. κ is the inner product coefficient in hyperbolic tangent function.

Table 3.01 Three common kernel functions used in SVM

Kernel Name	Kernel Equations
Polynomial Kernel	$k(x, y) = < x,\ y >^d,\quad d \in R.$
Gaussian Kernel	$k(x, y) = \exp(-\frac{\lVert x - y \rVert^2}{2\sigma^2}),\quad \sigma > 0$
Sigmoid Kernel	$k(x, y) = \tanh(\kappa < x,\ y > + \vartheta), \kappa > 0, \vartheta \geq 0$

Assuming the training vectors x_i were projected into a higher dimensional space by the mapping ϕ, then Cortes and Vapnik (1995) showed that the discriminant function of SVM was:

$$f(x) = \mathrm{sgn}(\sum_{i=1}^{l} y_i \alpha_i K(x_i, x) + b) \tag{3.20}$$

In this research, the above three kernel functions were tested individually, and the kernel with the best performance was selected as the kernel function for the walnut meat and shell differentiation in hyperspectral imagery. More details are discussed below in Section 3.5.

3.5 Results and Discussions

Figure 3.7 shows some examples of hyperspectral walnut images in different categories using different bands. As illustrated in figure 3.7, each image at particular wavelength has its own contribution to the walnut shell and meat differentiation. However, using only single or limited number of wavelength will not be sufficient enough to differentiate the shell and meat unless all the spectral contributions are carefully considered and efficiently combined. By extracting and combining effective wavelengths from hyperspectral imaging through pattern recognition and data mining algorithms, the differentiation of shell and nuts are obtained consequently.

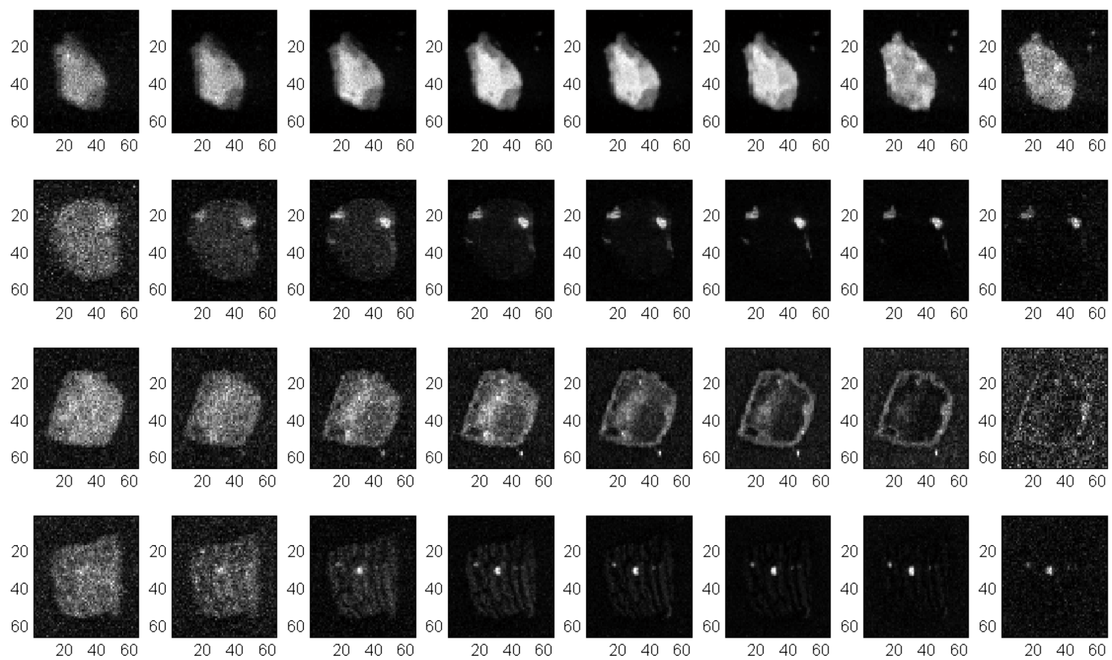

Figure 3.7 Hyperspectral walnut image examples in different categories using different wavebands: each row represents different objects of walnut meat and shell, and each column represents the spectral images at different wavelengths (from 1st to 8th column: 425nm, 470nm, 515nm, 560nm, 615nm, 660nm, 745nm, and 775nm).

The spectral curves of four different walnut categories are given in figure 3.8. The light meat appears much more sensitive to the fluorescence spectral than the other three, which was consistent with the observation. However, it was impractical to differentiate dark meat and shells using only a single threshold method. The proposed PCA-GMM and SVM approach showed its feasibility to solve aforementioned classification problem.

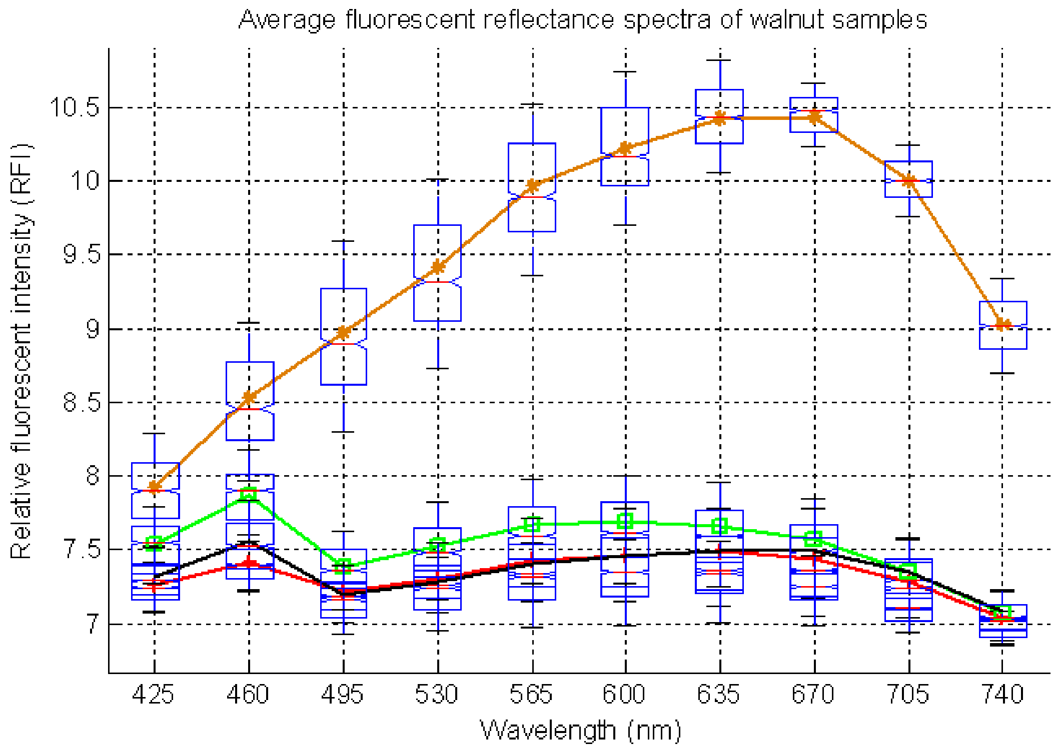

Figure 3.8 Fluorescence spectrum of walnut shell and meat. Each line represents different categories. Orange line: White meat; Green line: Inner shell; Black line: Dark Meat; Red line: Outer shell.

The training and testing spectral samples were randomly selected from the dataset, and all the samples were assumed independently identically distributed (i.i.d.) from the population. The total number of pixel samples was 5496, which included 1079 light meat, 1472 dark meat, 1276 inner shell and 1669 outer shell pixel samples. Training sample and testing sample are randomly selected from each category. The detailed composition of data was shown in table 3.2.

Table 3.02 Training and test samples in experiments of GMM method

Class	Training	Testing	Totals
C1: Light Meat	552	527	1079
C2: Dark Meat	738	734	1472
C3: Inner Shell	646	630	1276
C4: Outer Shell	812	857	1669
Totals	2748	2748	5496

In order to determine the optimal number of PCA components, 2-folds cross-validation was used in the data set. K nearest neighborhood clustering method (K=5) was applied as a classifier in this experiment. The relationship between selected components m and the overall error rate of all four classes was plotted in figure 3.9. As shown in figure 3.9, the overall error rate reached its minimum, which was about 10%, at $m = 6$. The optimal number of PCA components was then chosen as 6 in this research. Another interesting phenomenon, which could be observed in the figure 3.9, was that when m was very small, such as 1, the total error rate was very high (above 30%). However, when m was equal to or greater than 2, the total error rate reduced significantly (less than 15%). That means, if even only the three most significant components were selected as the projection vectors in PCA, the classification performance would still reach above 85%. One of the advantages of using small number of PCA components is that it could save the computation time. The high recognition rate under relatively small number of PCA components also showed the efficiency and robustness of proposed approach.

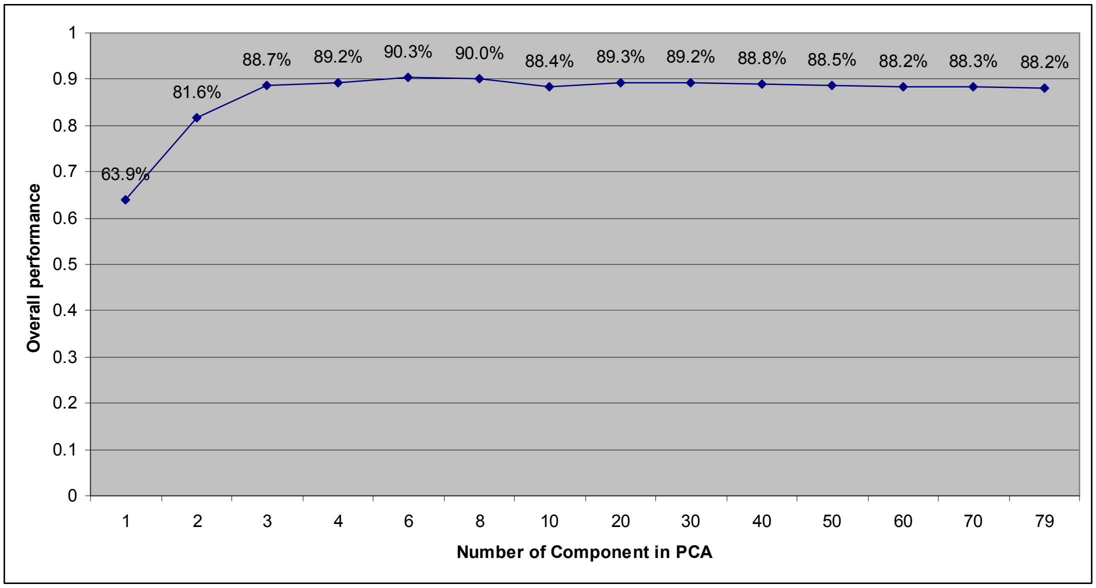

Figure 3.9 Number of components in PCA vs. overall error rate based on all four classes.

In order to evaluate the effectiveness of PCA feature extraction, both the PCA-GMM based and pure GMM based Bayesian classifier were tested and compared in the experiment. Based on the total 5496 samples, which included 2748 training samples and 2748 test samples, the confusion matrix was given in table 3.3 to show the performance of PCA-GMM based Bayesian classifier as well as the comparison between above mentioned classifier with (numbers after symbol '/') and without (numbers before the symbol '/') PCA feature extraction. In table 3.3, the diagonal cells represented the number of correctly classified samples in each class, while the off-diagonal cells demonstrated the number of misclassified samples in each class.

Table 3.03 Confusion matrix of classification result by PCA-GMM and GMM. The corresponding error rate plots are in figure 3.10 and 3.11.

True Labels	Estimated Labels (GMM/ PCA-GMM)				Totals
	Light Meat	Dark Meat	Inner Shell	Outer Shell	
Light Meat	514/519	4/5	5/2	4/1	527/527
Dark Meat	8/10	620/685	2/0	104/39	734/734
Inner Shell	0/0	0/0	606/614	24/16	630/630
Outer Shell	1/5	45/21	33/14	778/817	857/857
Totals	523/534	669/711	646/630	910/873	2748/2748

Type I and II errors (Lyman, 2001) are the most common statistics to evaluate the performance of a classification procedure in pattern recognition. Type I error is the error rate of missing classified sample in each category, for example in category light meat, the type I error is the number of pixels of light meat that were misclassified as being of another classes divided by the total number of light meat. Type II error is the error rate of false classified samples in each category, for example in category light meat, the type II error is the number of pixels falsely classified as light meat divided by the total number of light meat. According to the table 3.3, the type I and II errors in each categories as well as the total error was plotted in figure 3.10 and figure 3.11, respectively. As shown in figure 3.10, in all four categories light meat, dark meat, inner shell and outer shell classes, the type I error of PCA-GMM was lower than that of GMM. Especially in dark meat class, the type I error rate was reduced significantly from 15.5% to 6.7%. Although the total error of PCA-GMM was lower than that of GMM, the total errors of both classification methods (PCA-GMM and GMM) were lower than 10%, which showed not only the improvement after PCA feature extraction, but also the effective and robustness of the Gaussian Mixture Model itself. Similarly, for type II error (figure 3.11), in dark meat, inner shell and outer shell class, the type II error of PCA-GMM was lower than that of GMM alone. However, in light meat class, the type II error of PCA-GMM was higher than that of GMM. In general, the total error rates of both classifications were less than 10%, which was the same as figure 3.10.

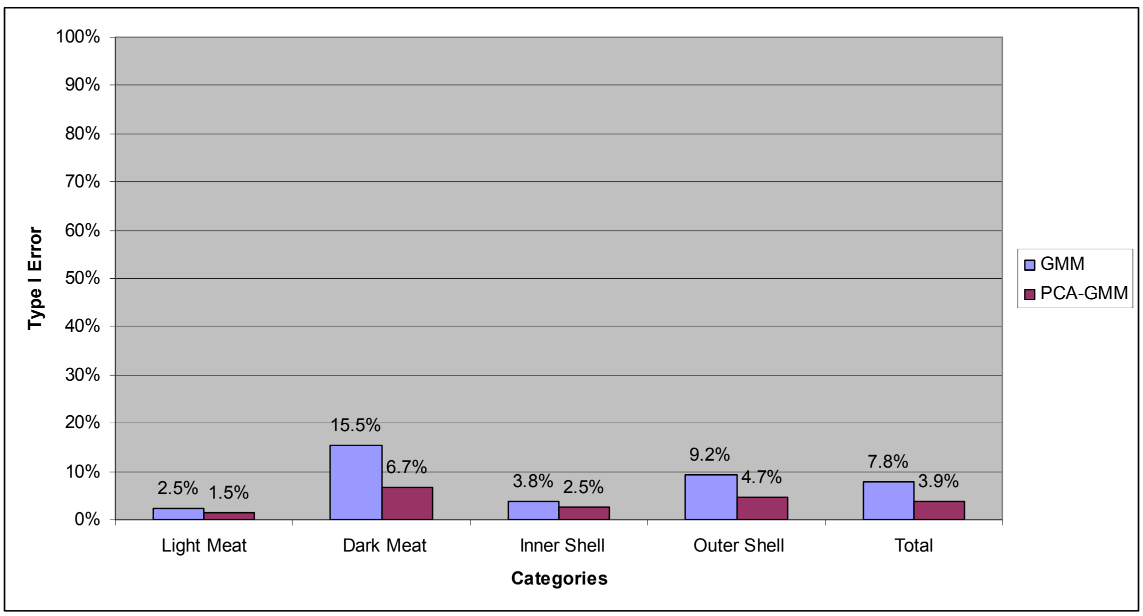

Figure 3.10 Type I error under different categories using GMM model and PCA-GMM model.

From figure 3.10 and 3.11, two conclusions could be drawn: Firstly, the overall error rate was low (below 8%) whether the PCA feature extraction was applied or not. The GMM based Bayesian classifier could achieve at least 92.2% recognition rate, which not only showed the Gaussian Mixture Model had a decent overall performance, but also made it a capable approach for walnut meat and shell discrimination. Secondly, a lower 3.9% total type I error could be achieved by PCA-GMM comparing to the 7.8% error rate by pure GMM. And similarly a lower 3.9% total type II error could be obtained by PCA-GMM comparing to the 7.5% type II error rate by pure GMM. The comparison between with and without using PCA feature extraction demonstrated that the PCA-GMM outperformed the GMM, which showed the effectiveness of PCA feature extraction.

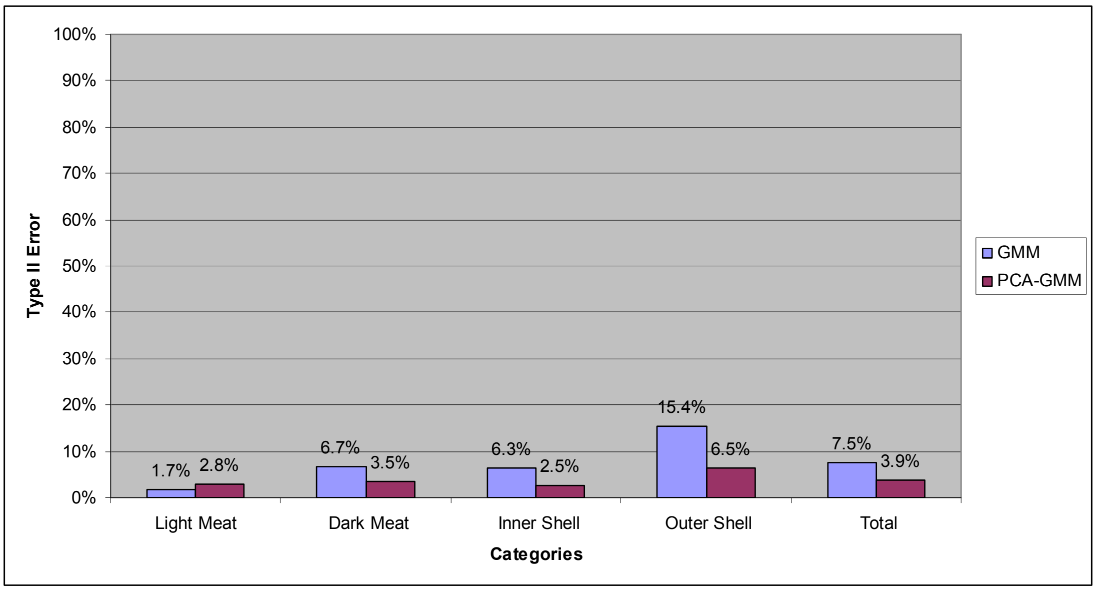

Figure 3.11 Type II error under different categories using GMM model and PCA-GMM model.

To further evaluate the performance the above mentioned classification methods, cross-validation technique was also applied in this study. The total 5496 samples were divided into 2, 4, 6, and 8 cross-validation folds respectively, and the relationship between the number of validation folds and recognition rate under different categories with and without PCA feature extraction was shown in figure 3.12 and in figure 3.13, accordingly.

As seen from figure 3.12, no matter which category was considered, or which cross-validation setting was used, the recognition rate was always greater than 80%. Especially in the light meat class, the recognition rate could achieve as high as 98% even the PCA feature extraction was not used. In figure 3.13, all the recognition rates were greater than 90% regardless of the categories and fold settings. In the light meat class, the recognition rate could even reach 99.7% given PCA feature extraction was employed. As the fold numbers in cross-validation varied, the total recognition rate of two methods did not change too much, and always stayed above 90% for GMM, and 95% for PCA-GMM. So both of these two approaches were robust and had a good generalization in application of classifying walnuts' shell and meat. In addition, improvements could be obtained if PCA feature extraction was used, which agreed with the findings in figure 3.10 and 3.11.

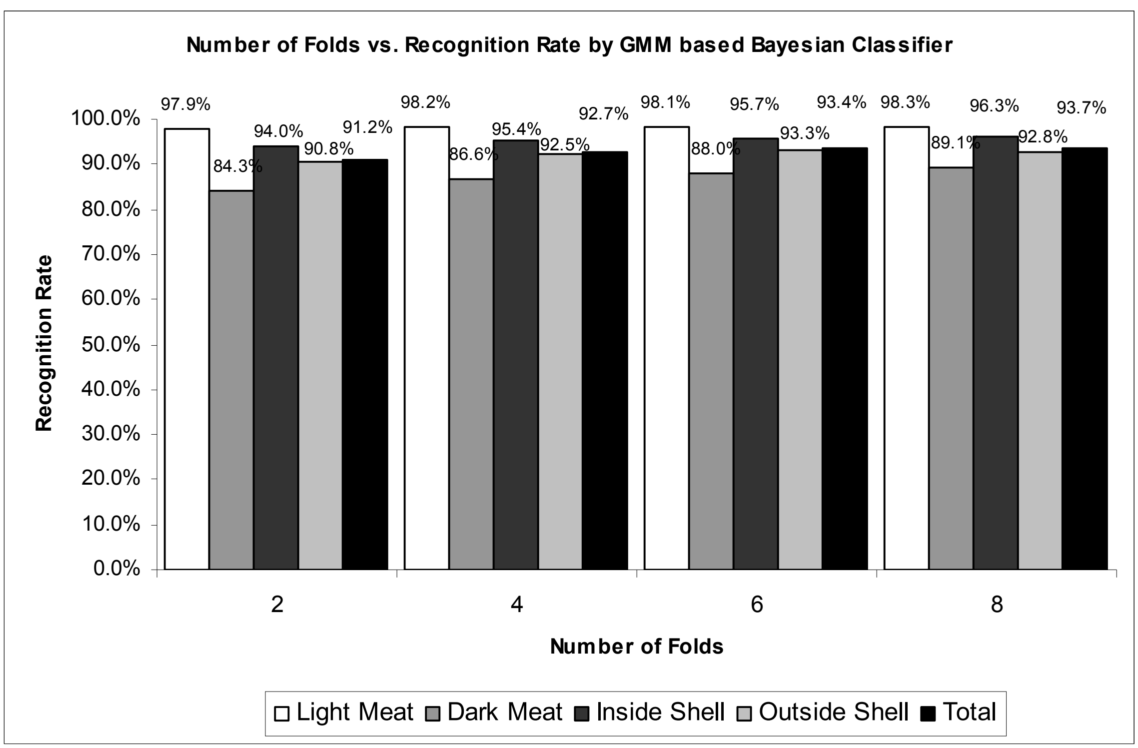

Figure 3.12 Number of validation folds vs. recognition rate by GMM based Bayesian classifier.

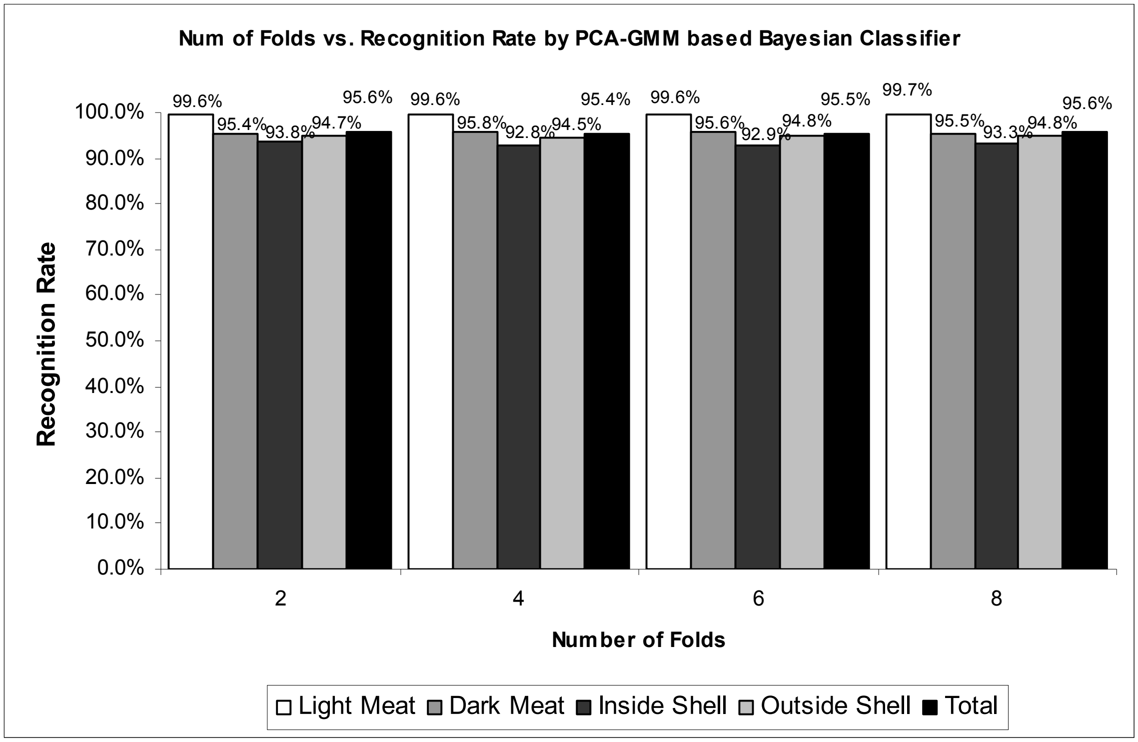

Figure 3.13 Number of validation folds vs. recognition rate by PCA-GMM based Bayesian classifier.

In order to choose the optimal kernel in the SVM method, the classification performance of three kernel functions with different parameters (2-folds cross validation) were tested based on the random selected training samples from the dataset (Figure 3.14) using 2-folds cross-validation method. As seen in Figure 3.14, the sigmoid kernel function obtained the lowest classification performance among the three kernel functions, and polynomial kernels with degree of freedom d equal to 1 and 2 did not get high classification performance. However, Gaussian kernels with σ greater than or equal to 0.1 have better performance than other kernels and the SVM with Gaussian kernel has the best classification result.

Once Gaussian kernel in SVM has been selected as the kernel function used in this research, different parameter σ settings in Gaussian kernel was tested based on the training samples set using 2-folds cross-validation method as shown in figure 3.15. Seen from figure 3.15, the classification performance could be up to maximum when σ is equal to 0.1. As a result, SVM with Gaussian kernel (σ=0.1) was selected as a classifier for the walnut meat and shell differentiation in hyperspectral imagery in the following experiments.

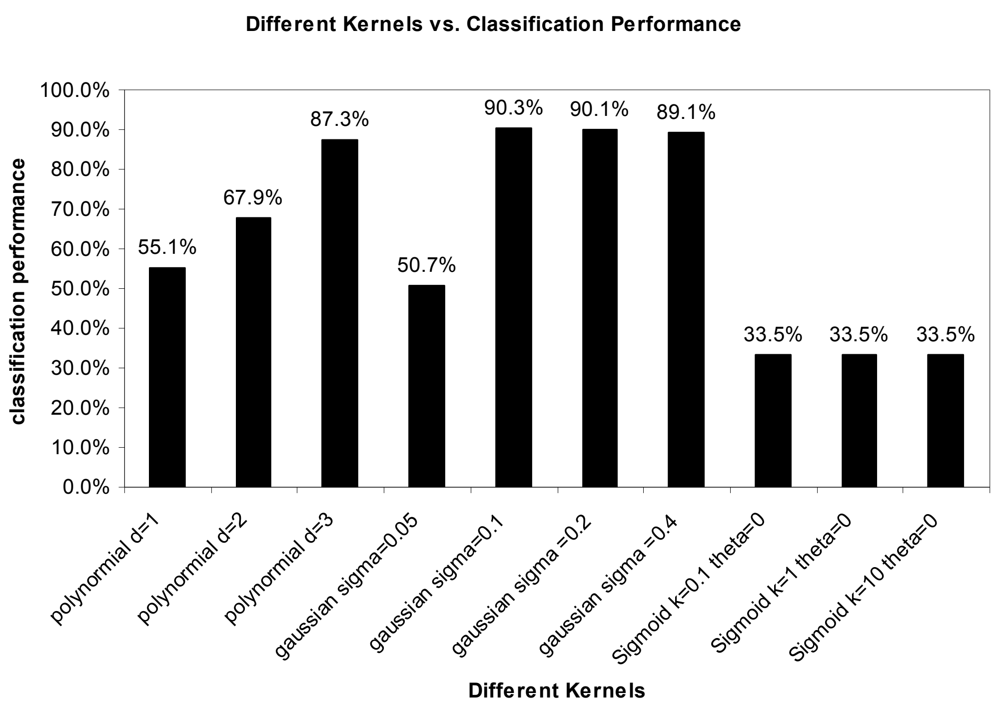

Figure 3.14 Comparison of the classification performance of different kernels. Gaussian kernels with σ greater than or equal to 0.1 have better performance than other kernels and the SVM with Gaussian kernel has the best classification result

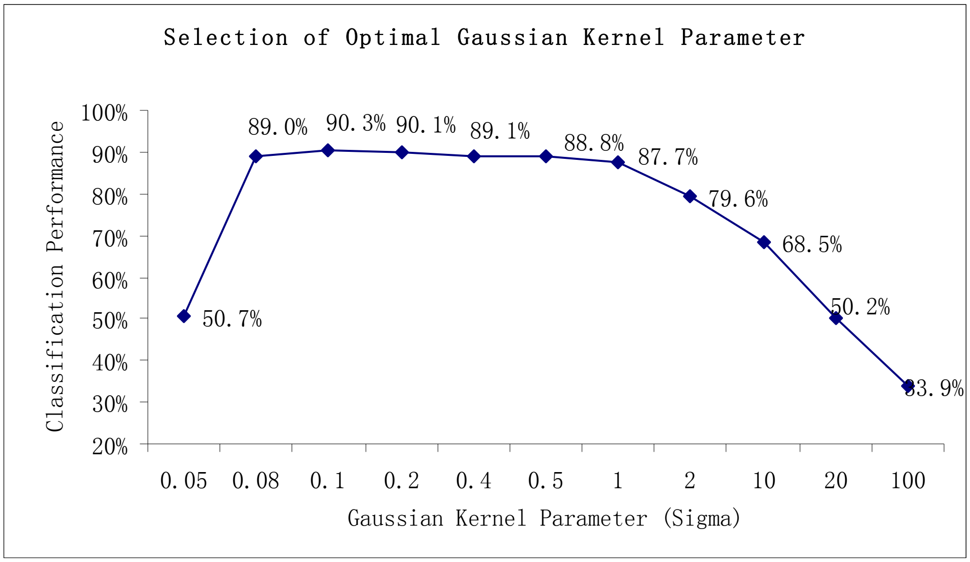

Figure 3.15 Selection of optimal Gaussian kernel parameter σ, the classification performance could be up to maximum when σ is equal to 0.1.

In this experiment, the training and testing data set is the same with the one used in GMM method which is shown in Table 3.2. Table 3.4 present the confusion matrix of classification results under SVM with Gaussian kernel (σ = 0.1) methods. The total recognition rate of the SVM method with Gaussian kernel (σ = 0.1) is about 97%.

Table 3.04 Confusion matrix of classification result with SVM with Gaussian kernel (σ = 0.1)

	Estimated Labels (SVM)				
True Labels	**Light Meat**	**Dark Meat**	**Inside Shell**	**Outside Shell**	**Totals**
Light Meat	517	3	0	7	527
Dark Meat	7	715	0	12	734
Inside Shell	0	0	615	15	630
Outside Shell	4	31	8	814	857
Totals	528	749	623	848	2748

Furthermore, type I and type II errors of each class for Gaussian kernel based SVM method calculated from Tables 3.4 are shown in Figure 3.16. Seen from figure 3.16, the recognition error for each category including type I and type II error is less than 5.0%. And the overall error is about 3%.

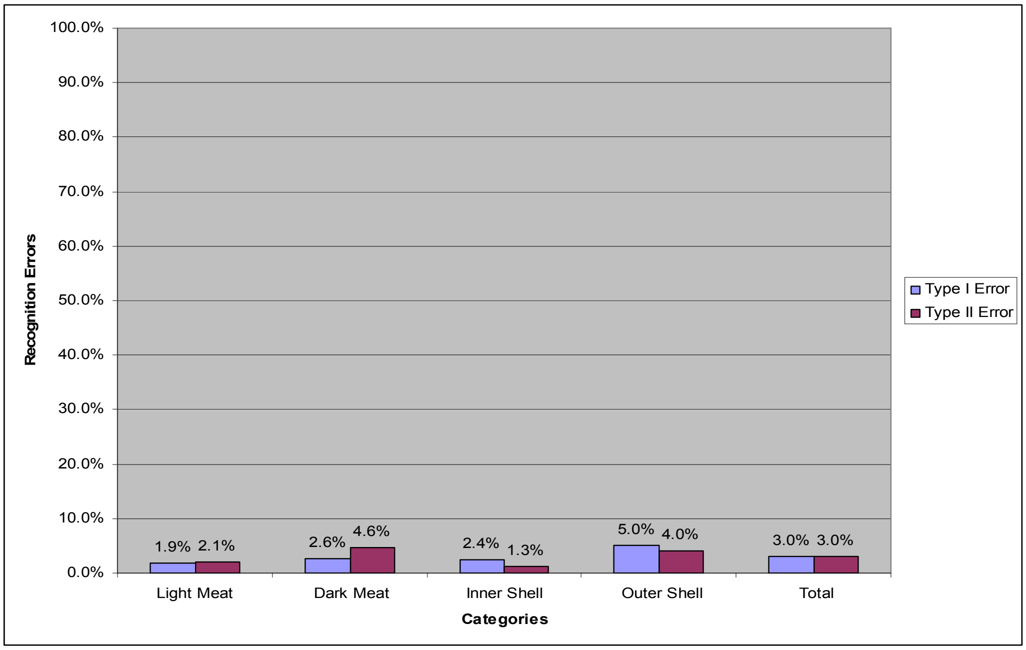

Figure 3.16 Type I and type II errors in Gaussian kernel based SVM method.

Cross-validation technique was conducted to the data in table 3.2 to test the robustness of Gaussian kernel based SVM method. The recognition result in 2, 4, 6 and 8 folds cross validation by SVM method was shown in figure 3.17. Seen from figure 3.17, no matter which category was considered, or which cross-validation setting was used, the recognition rate was always greater than 90%. Categories light meat, dark meat and inner shell are above 95%, and out shell class is a little lower than 95%. Especially in the light meat class, the recognition rate can achieve as high as 99%, and the overall recognition rate is about 97%.

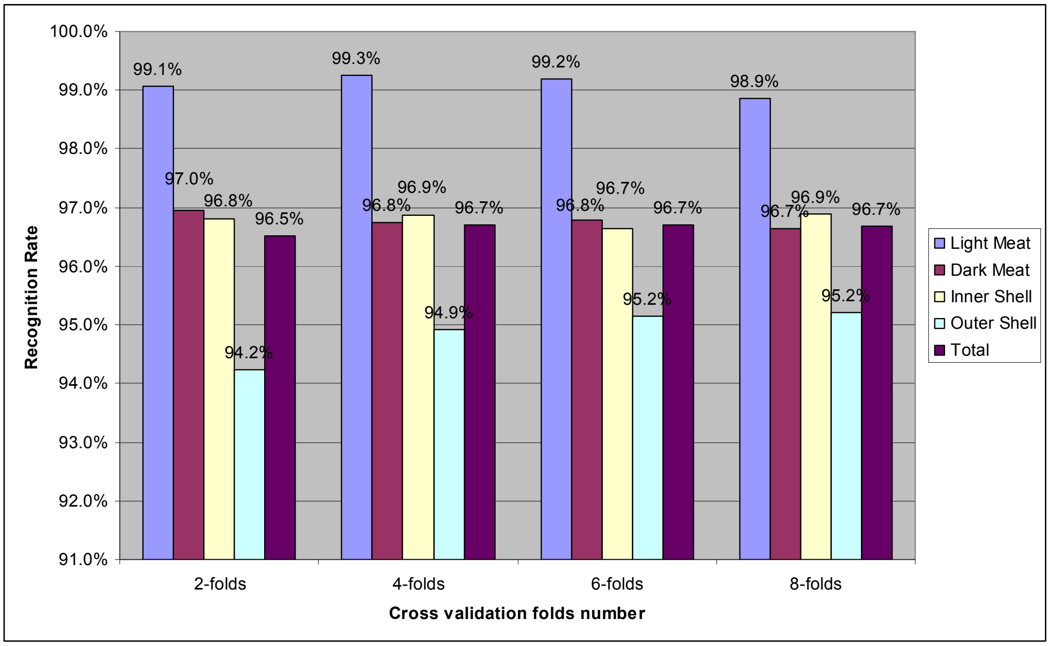

Figure 3.17 Number of validation folds vs. recognition rate by Gaussian kernel based SVM classifier.

Figure 3.18 shows an example of walnuts meat hyperspectral fluorescence image classification results. In this hyperspectral walnuts meat image, there are about total 65 objects. All the objects in the image are walnuts meats including both light meat and dark meat. The left side image (a) is the original hyperspectral image at 447.5 nm wavelength. The middle image (b) is the pixel based image classification result corresponding to the image (a). And the right side image (c) is the object based image classification by majority rule. From this result, we can see only 1 meat was misclassified as shell and all other meat was correctly classified.

Similarly figure 3.19 shows an example of walnuts' shell hyperspectral image classification results. All the objects in this image are walnuts shells including both inner shell and outer shell. The left side image (a) is the original hyperspectral image at 447.5 nm wavelength. The middle image (b) is the pixel based image classification result corresponding to the image (a). And the right side image (c) is the object based image classification by majority rule. Seen from this result, all the shells were correctly classified.

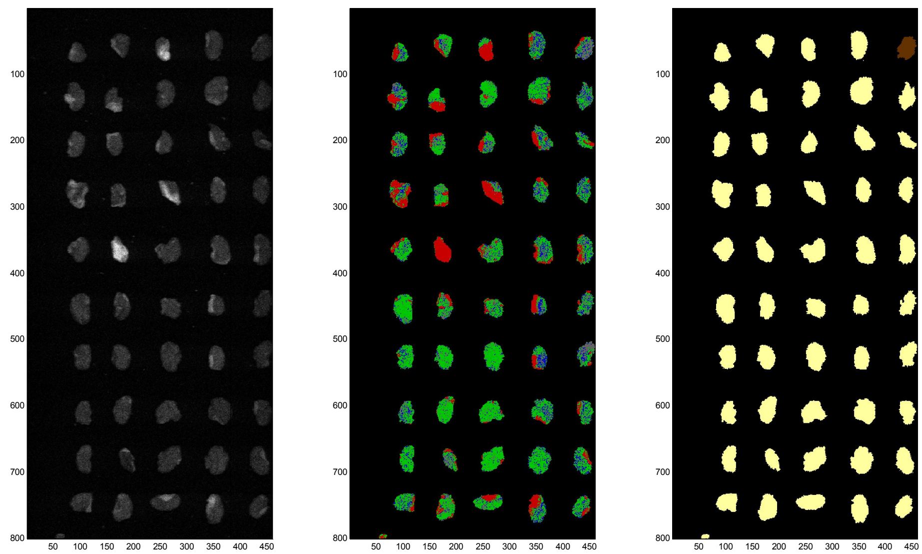

(a) (b) (c)

Figure 3.18 An example of walnuts meats hyperspectral fluorescence image classification results. (a): Original hyperspectral image at 447.5 nm wavelength. (b): Pixel based image classification result. Red color represents light meat. Green color represents dark meat. Blue color represents inner shell. Gray color represents outer shell. (c) Object based image classification result by using majority rule. Yellow color represents walnuts meat category. Brown color represents walnuts shell category.

To further evaluate the effectiveness of hyperspectral fluorescence imaging in identifying walnuts shells and the effectiveness of the proposed classification methods, total 228 walnuts including 50 light meats, 65 dark meats, 69 inner shells and 44 outer shells were tested to get the object based image classification results shown in figure 3.20 by PCA-GMM method and Gaussian kernel based SVM method respectively. Seen from figure 3.20, detection rate of meat is above 99%, and about 98% of detection rate of shells is obtained. Total detection rate by PCA-GMM method is about 98.2% and total detection rate by support vector machine is about 98.7%.

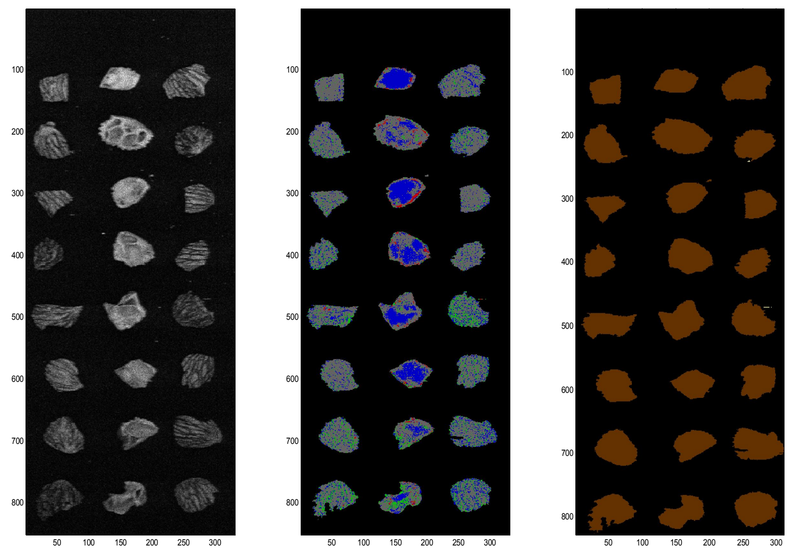

(a) (b) (c)

Figure 3.19 An example of walnuts shell hyperspectral fluorescence image classification results. (a): Original hyperspectral image at 447.5 nm wavelength. (b): Pixel based image classification result. Red color represents light meat. Green color represents dark meat. Blue color represents inner shell. Gray color represents outer shell. (c) Object based image classification result by using majority rule. Yellow color represents walnuts meat category. Brown color represents walnuts shell category.

Object based type I and type II error rate by PCA-GMM and Gaussian kernel SVM classification was calculated in figure 3.21 and figure 3.22, respectively. The type I and type II error of meat category by PCA-GMM approach is about 0.9% and 2.6%, respectively, while the type I and type II error of shells category by PCA-GMM is about 2.7% and 0.9%, respectively. Similarly, the type I and type II error of meat category by SVM is about 0.9% and 1.7%, and the type I and type II error of shells category by SVM is about 1.8% and 0.9%, respectively. The total error rate by SVM approach is about 1.3%, and by PCA-GMM method is 1.8%. Both approaches achieve a fairly low error rate, below 2%.

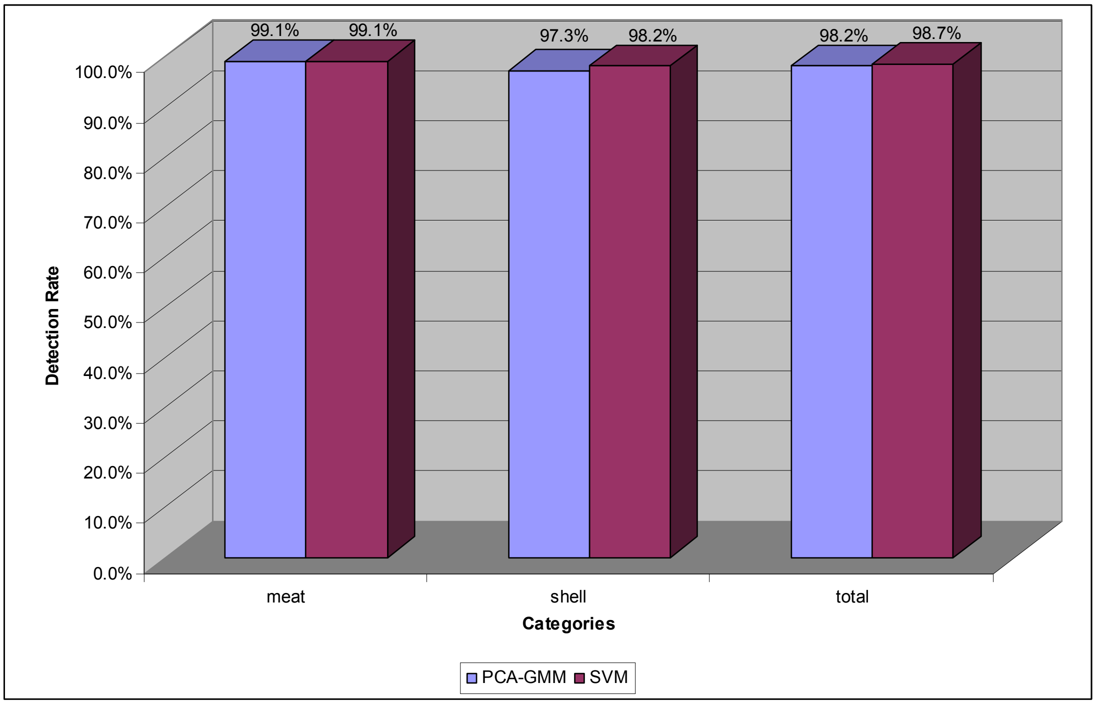

Figure 3.20 Detection rate by PCA-GMM and Gaussian kernel based SVM classifier, respectively.

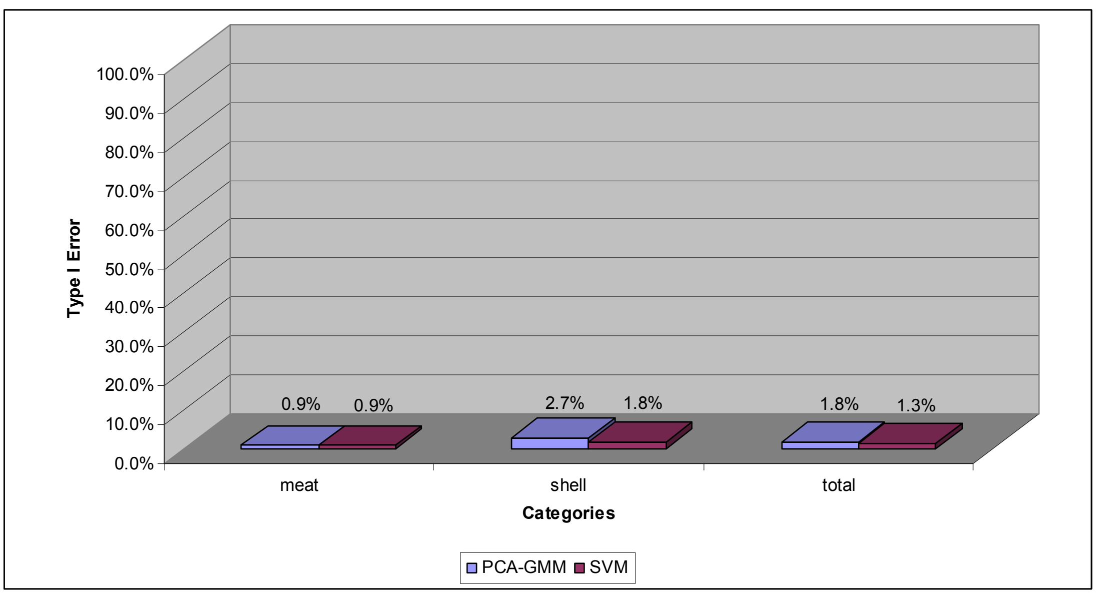

Figure 3.21 Object based Type I error rate by PCA-GMM and Gaussian kernel based SVM classifier, respectively.

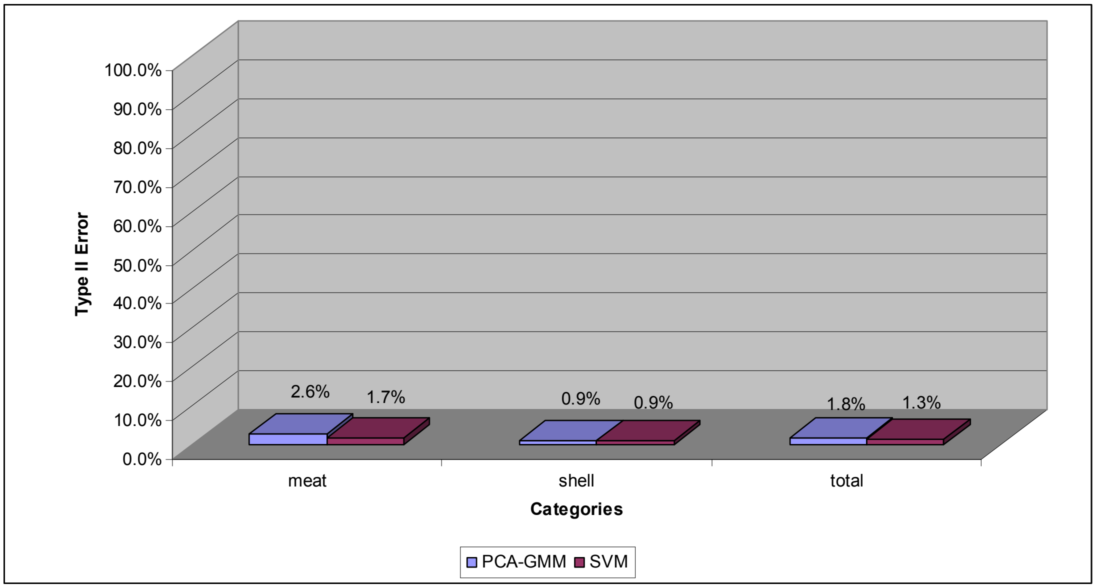

Figure 3.22 Object based Type II error rate by PCA-GMM and Gaussian kernel based SVM classifier, respectively.

3.6 Conclusions

Although the eastern black walnut grows throughout the Central and Eastern U.S., farmers are currently unable to reach their economic potential because of the lack of cost effective and efficient methods for black walnut shell and meat differentiation. To overcome this challenge, the use of hyperspectral fluorescence imaging to analyze the differences between walnut shell and meat is suggested. The PCA-GMM based Bayesian classifier was presented to identify the walnuts' shell and meat in hyperspectral fluorescence imagery. The recognition results showed that the proposed approach was effective for the walnut shell and meat classification. A total of 5496 walnuts' pixel samples were studied in this research and an overall recognition rate of 95.6% was achieved by the PCA-GMM method. Furthermore, the SVM classifier with Gaussian kernel was evaluated in the experiments. The experimental results showed that the SVM method with Gaussian kernel function was also effective in classifying walnut shell and meat using hyperspectral fluorescence imagery. An overall recognition rate of 96.7% was achieved using the SVM approach. To further evaluate the effectiveness of the proposed approaches, total 228 walnuts were tested to get the object based image classification result, which shows the total recognition rate by PCA-GMM method is about 98.2% and total detection rate by SVM is about 98.7%.

4 Optimal Band Selection for Differentiation of Walnuts Meat and Shell in Hyperspectral Fluorescence Imagery

4.1 Introduction

Recently, machine vision technology has been widely used in many food processing areas, such as fruit (Cheng, et al., 2004; Vargas, et al., 2004a) and poultry (Ma, et al., 2005; Tao, et al., 2004). As one of the very promising machine vision technologies, hyperspectral fluorescence imaging is found to be effective to solve previously mentioned challenging problem because of its ability to discriminate walnut shell and meat target by providing precise spectral information from their chemical compositions. We proposed a Gaussian-kernel based Support Vector Machine (SVM) approach to identify walnut shell from meat according to all the 79 wavelengths information acquired by a hyperspectral fluorescence imaging device (Jiang, et al., 2007a). The hyperspectral image data was first mapped to a high-dimensional linear feature space. And then, the SVM classifier was applied to do the differentiation on aforementioned high-dimensional space. An overall 96.7% recognition rate was achieved, and showed the effectiveness of proposed method. We also introduced a Principal Component Analysis - Gaussian Mixture Model (PCA-GMM) based method, which model the whole hyperspectral data cube as a combined Gaussian distribution, to discriminate walnut shell from meat space (Jiang, et al., 2007b). Principal Component Analysis (PCA) was first used to extract features and reduce the redundancy of the input data. Then the PCA-GMM-based Bayesian classifier was applied to differentiate the walnut shell and meat given the class-conditional probability and the prior estimated by the Gaussian mixture model. Other than walnut processing area, hyperspectral fluorescence imaging is also widely used in many food processing fields such as fruit (Lu, 2003; Vargas, et al., 2004b), and poultry (Park, et al., 2002).

Although hyperspectral fluorescence imaging has been shown to be an effective technology in many food processing areas, one persistent problem associated with this approach must be solved in order to meet the industry requirements of real-time inspection –How to deal with the huge amount of data obtained by the hyperspectral imaging device, and hence improve the efficiency of the application system. A typical hyperspectral image consists of one hundred or so contiguous spectral bands, which means even for a very small image size, for example, 100 ×100 ×8 bit, there will be a total of 1 megabytes data to be processed for that single sample. On the other hand, there must be some redundancies in the hyperspectral image data sets, since the information among individual band can not be totally unrelated. Furthermore, the cost and the scanning speed of hyperspectral imaging system are the other two issues which prevent this technology being accepted by the walnut processing plants. As a result, how to select the optimum wavelengths for walnut shell and meat classification, and meanwhile not sacrifice too much classification performance becomes very important.

4.2 Literature Review

4.2.1 Overview of band selection in hyperspectral imaging

Hyperspectral sensors can image an object with hundreds of spectral channels at different wavelength for identification of composition of various materials. As a result, each image scene represents an image cube with the third dimension specified by spectral range. Such 3D representation creates enormous amounts of data for computer processing and data transmission. Band selection for hyperspectral image data is an effective way to mitigate the curse of dimensionality. Taking advantage of spectral correlation to achieve optimal band selection is one of the unique features in multispectral/hyperspectral images.

4.2.2 Current band selection techniques in hyperspectral imaging and their limitations

A lot of efforts have been made by the researchers to perform the optimal band selection for food quality inspection purposes. Park, et al. (2002) extracted four dominant wavelengths (434, 517, 565, and 628 nm) from hyperspectral image data acquired between 400 and 900 nm with 512 spectral bands in order to detect fecal and ingesta contamination on poultry carcasses. They applied PCA on visible/near-infrared spectroscopy to select the optimal wavelengths in hyperspectral imagery. The experiments results showed that the band ratio of dual-wavelength (565/517) was effective to identify the fecal contamination on poultry carcasses. Haff and Pearson (2006) introduced a nearest-neighbor based classification scheme to choose two optimal spectral bands from NIR spectra for sorting pistachio nuts defects. The results of 1.20% false negative for small inshell and 1.80% false negative for half shells with 0.15% false positive were achieved according to the selected wavelengths. They also compared sorting accuracy of selected optimal bands to the bands recommended by the manufacture. The comparison showed that the proposed optimal bands could replace the recommend bands in commercially available nuts sorting machines. Delwiche and Gaines (2005) applied single- and all combinations of two-wavelength linear discriminant analysis models to remove Fusarium Head Blight (FHB) infected soft red winter wheat kernels. The optimal wavelengths were selected from visible and near-infrared spectrum region. The best models occurred near the wavelengths of 500/550 nm for the visible region with a 94% accuracy, 1152/1248 nm for the near-infrared region with a 97% accuracy, and 750/1476 nm for the hybrid region with an 86% accuracy. Xing, et al. (2006) used chemometrics tools to extract the effective wavebands for bruises detection on tomatoes under hyperspectral imagery. The hyperspectral image ranging from 400 and 1000 nm were studied in their research. Peng and Lu (2006) set up a compact multispectral imaging system to do the apple firmness estimation. The multispectral images with wavelength ranging from 650 to 1000 nm were acquired through abovementioned system. Optimal wavelengths for firmness prediction were obtained by multi-linear regression (MLR) and cross-validation methods. They also compared proposed approach to the one using a visible/near-infrared spectrometer (Vis/NIRS), and the results showed the proposed approach had better performance than the latter one.

Although hyperspectral fluorescence image data is quite useful for discriminating subtle differences between walnut shell and meat, it has redundant information at the band level. The objective of this research was to identify optimal bands that contain the key information needed for walnut shell and meat classification while keeping the redundancy minimal. The optimal band selection was performed with the Independent Component Analysis (ICA) approach. The k Nearest Neighbors classifier (kNN) was followed to do the discrimination between walnut shell and meat according to selected wavelengths. The proposed ICA-kNN approach was also compared to the directly kNN method without ICA. The comparison showed the effectiveness of the proposed method in the walnut shell and meat classification.

4.3 Materials and Methods

It is known that independent component analysis (ICA) has become one of the most important methods in blind source separation (BSS), feature extraction/analysis and many other pattern recognition related areas. Among the band selections methods in hyperspectral imagery, ICA is also one of the most popular techniques. It was first introduced by Herault and Jutten (1986) and was refined by Comon (1994). It extracts independent source signals by looking for a linear or nonlinear transformation that minimizes the statistical dependence between components.

Given the observed signal $X = (X_1, X_2, ..., X_n)^T$, which is the spectral profile of the hyperspectral image pixels in this research, and the source signal $S = (S_1, S_2, ..., S_m)^T$ with each component corresponding to the existing material or classes in the hyperspectral image, a linear ICA unmixing model can be expressed as:

$$S_{m\times p} = W_{m\times n} X_{n\times p} \tag{4.1}$$

Where W is the weight matrix in the unmixing model, and p is the number of pixels in the hyperspectral images.

As seen from equation (4.1), the system mixing model with additive noise can be written as:

$$X_{n\times p} \equiv Y_{n\times p} + N_{n\times p} = A_{n\times m}S_{m\times p} + N_{n\times p} \tag{4.2}$$

Assume the additive noise $N_{n\times p}$ is a stationary, spatially white, zero-mean complex random process independent of source signal. Also assume the matrix A to have full column rank and the component of source S to be statistically independent, and no more than one component is Gaussian distributed, the weight matrix A can be estimated by the second order blind identification ICA (SOBIICA) algorithm which was introduced by Belouchrani, et al., (1997) and Ziehe, et al., (1998).

SOBI is defined as the following procedure:

(1) Estimate the covariance matrix R_0 from p data samples. R_0 is defined as

$$R_0 = E(XX^*) = AR_{s0}A^H + \sigma^2 I \tag{4.3}$$

where R_{s0} is the covariance matrix of source S at initial time, H denotes the complex conjugate transpose of matrix. Denote by $\lambda_1, \lambda_2......\lambda_m$ the m largest eigenvalues and $u_1, u_2.......u_m$ the corresponding eigenvectors of R_0. Under the white noise assumption, an estimate of σ^2 the noise variance is the average of the smallest n-m eigenvalues of R_0.

(2) Calculate the whitened signal $Z = [z_1, z_2,......z_m] = BX$, where $z_i = (\lambda_i - \sigma^2)^{-\frac{1}{2}} u_i^* x_i$ for $1 \le i \le m$. This is equal to forming a whitening matrix B by

$$B = [(\lambda_1 - \sigma^2)^{-\frac{1}{2}} u_1, (\lambda_2 - \sigma^2)^{-\frac{1}{2}} u_2, \ldots\ldots, (\lambda_l - \sigma^2)^{-\frac{1}{2}} u_m] \tag{4.4}$$

(3) Estimate the covariance matrix R_τ from p data samples by calculating the covariance matrix of Z for a fixed set of time lag, such as $\tau = [1,2,\ldots\ldots,K]$.

(4) A unitary matrix U is then obtained as joint diagonalizer of the set $\{R_\tau | \tau=1,2,\ldots\ldots,K\}$.

(5) The source signals are estimated as $S = U^H BX$ and the mixing matrix A is estimated by $A = B^{\#}U$, where # denote the Moore-Penrose pseudoinverse.

If the number of materials in the n-band hyperspectral images is m, the related weight matrix W is approximated by SOBIICA algorithm. The source component S_{ij} with $i = 1, \ldots, m$ can be expressed as the following equation according to the ICA unmixing model.

$$\begin{bmatrix} s_{11} & . & . & . & s_{1p} \\ . & . & . & . & . \\ . & . & s_{ij} & . & . \\ . & . & . & . & . \\ s_{m1} & . & . & . & s_{mp} \end{bmatrix} = \begin{bmatrix} w_{11} & . & . & . & w_{1n} \\ . & . & . & . & . \\ . & . & w_{ik} & . & . \\ . & . & . & . & . \\ w_{m1} & . & . & . & w_{mn} \end{bmatrix} \times \begin{bmatrix} x_{11} & . & . & . & x_{1p} \\ . & . & . & . & . \\ . & . & x_{kj} & . & . \\ . & . & . & . & . \\ x_{n1} & . & . & . & x_{np} \end{bmatrix} \tag{4.5}$$

That is,

$$s_{ij} = \sum_{k=1}^{n} w_{ik} x_{kj} \tag{4.6}$$

Seen from equation (4.6), the ith material in the source is the weighted sum of the kth band in the observed signal X with corresponding weight w_{ik}, which means the weight w_{ik} shows how much information the kth band contribute to the ith material class. Therefore, the significance of each spectral band for all the classes can be calculated as the average absolute weight coefficient $\overline{w_k}$, which is written as (Du, et al., 2003):

$$\bar{w}_k = \frac{1}{m}\sum_{i=1}^{m}|w_{ik}| \qquad k = 1,2,...,n \tag{4.7}$$

As a results, an ordered band weight series as

$$[\bar{w}_1, \bar{w}_2, \bar{w}_3, ..., \bar{w}_n] \text{ with } \bar{w}_1 > \bar{w}_2 > \bar{w}_3, ... > \bar{w}_n \tag{4.8}$$

can be obtained by sorting the average absolute coefficients for all the spectral bands. In this sequence the band with the higher averaged absolute weights contributes more to ICA transformation. In other words, the band with the higher averaged absolute weights contains more spectral information than the other band. Therefore, the bands with the top highest averaged absolute weights will be selected as the optimal bands for walnuts shell and meat differentiation.

Instead of projecting the original hyperspectral images into the other linear space, ICA band selection method evaluates the weight matrix to observe how each band contributes to the ICA unmixing procedure. It compares the average absolute weight coefficients of individual spectral bands and selects bands that contain more unmixable information. As a significant benefit, the ICA-based band selection retains most physical features of the spectral profiles given only the observations of hyperspectral images.

After the dimensionality reduction of hyperspectral images, k-Nearest Neighbor (kNN) approach was applied to classify the data into four categories, which are light meat, dark meat, inner shell and outer shell. In the test phase of the classification, Euclidean distances from the test sample to all the training samples are calculated and the *k* closest samples are selected. The test sample is predicted into the most frequent class within the dataset. As the size of data grows bigger and bigger, the kNN algorithm can approach an error rate no worse than twice the Bayesian error rate, which is the achievable minimum error in pattern classification. In this research, k is set to be equal to 9.

4.4 Results and Discussions

In this research, training and testing pixel samples were randomly selected from the dataset, and all the samples were assumed independently identically distributed (i.i.d.) from population. The detailed composition of the complete dataset is shown in Table 4.1.

Table 4.1. Detailed composition of complete experiment dataset

Class	Training	Testing	Totals
C1: Light Meat	554	525	1079
C2: Dark Meat	725	747	1472
C3: Inner Shell	629	647	1276
C4: Outer Shell	840	829	1669
Totals	2748	2748	5496

In order to show the different fluorescence spectral responses with respect to four walnut sample categories, the spectral curves of each category are given in Figure 4.1. As seen from Figure 4.1, the light meat, which is fairly easy to tell from other categories, appears much more sensitive to the fluorescence spectrum almost in all the spectral range compared to the other three. At the low-end of the spectral range especially between 425 nm and 470 nm, the differences can be found among all four categories, however those differences may not be observed consistently in the aforementioned spectral range. For example, in 434 nm (the first peak at the low-end), the fluorescence intensities of both inner shell and light meat are very similar, and hence can not tell the differences from each other. As the wavelength increases from 470 nm to 650 nm, the two spectra curves for dark meat and outer shell are mixed together, making them hard to distinguish, however, the inner shell is still differentiable. When the wavelength increases even further, three categories (dark meat/inner shell/outer shell) merge altogether, and can not be identified from each other.

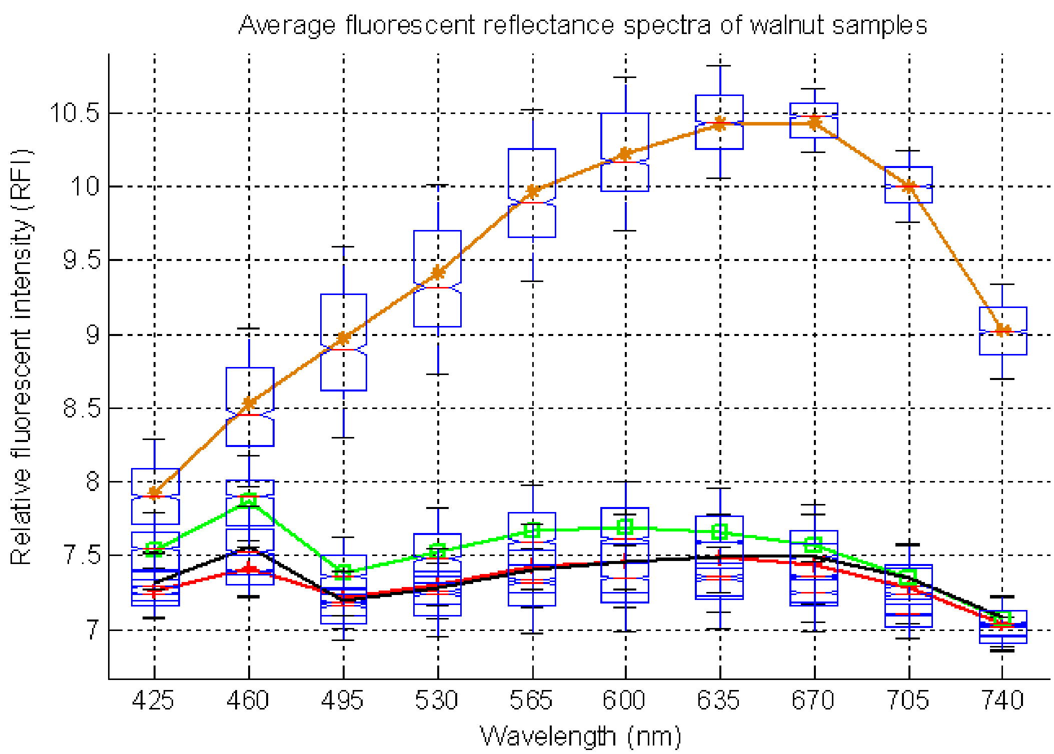

Figure 4.1. Fluorescence Spectrum of Walnuts Shell and Meat. Each line represents different categories. Orange line: White meat; Green line: Inner shell; Black line: Dark Meat; Red line: Outer shell.

Based on above facts, the low-end spectra might contain the most important information for the walnut shell and meat classification. As a result, quantitative study was needed to evaluate the contribution of each wavelength, and hence gave the optimal choice of wavelengths which contain the key information needed for walnut shell and meat classification while keeping the redundancy to be minimal. To fulfill this goal, the ICA-based optimal band selection approach was used to rank all the wavelengths according to their contributions to the all categories. The top five wavelengths selected by ICA are given in Figure 4.2.

As seen from Figure 4.2, the top 5 optimal wavelengths are coming from the previously mentioned low-end spectral range between 425 nm and 470 nm. In addition, the 434 nm wavelength, at which the fluorescence intensities of both inner shell and light meat are very similar, wasn't picked as one of the top 5 optimal wavelengths by the ICA approach. Actually, this wavelength was only ranked as 69^{th} among all 79 wavelengths. The above ICA based results seem consistent with what was found in Figure 4.1.

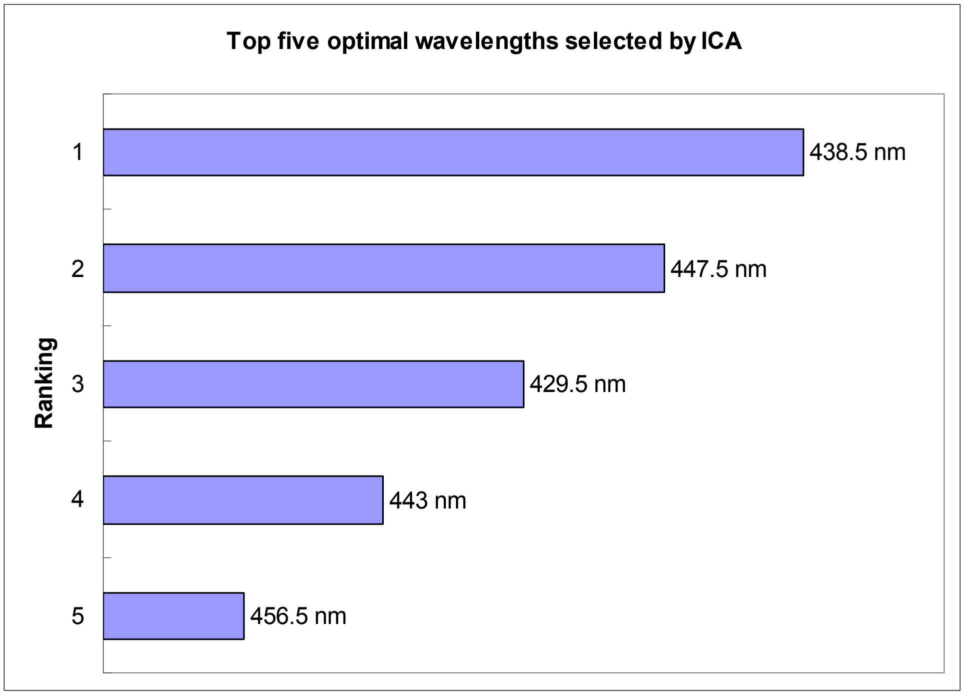

Figure 4.2. Top five optimal wavelengths selected by ICA.

To further evaluate the performance of proposed approach, the kNN classifier was employed to do the walnut shell and meat differentiation according to the ICA selected optimal wavelengths. A total of 2748 samples with top 4, 6, 8 and 10 optimal wavelengths were tested in this study. The relationship between selected number of bands and recognition rate for each walnut category is plotted in Figure 4.3.

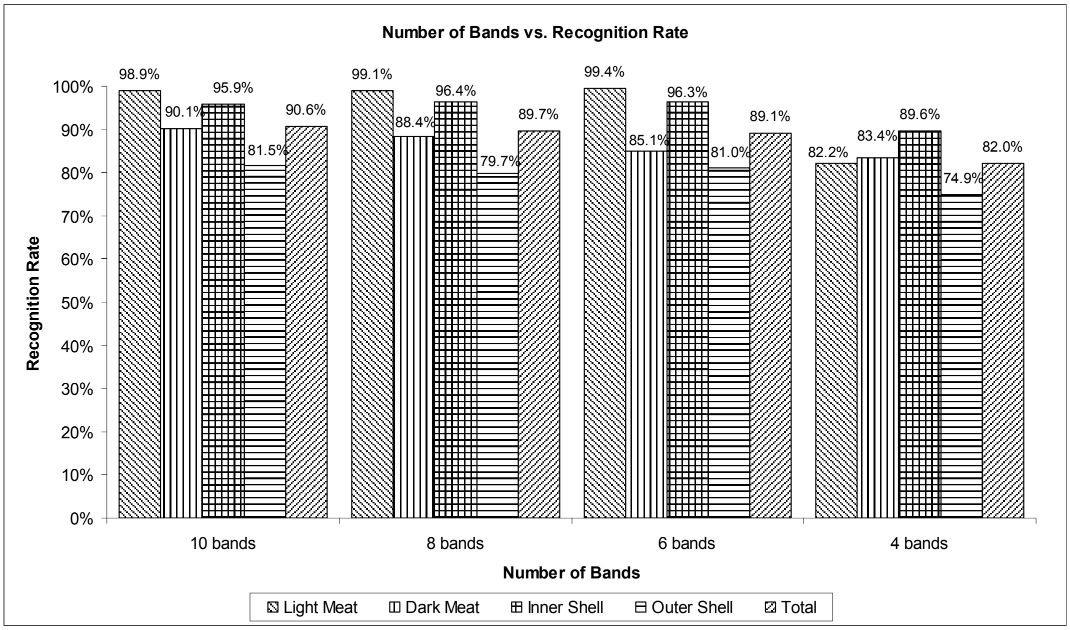

Figure 4.3 The relationship between number of selected optimal bands and corresponding recognition rate for each category. Notice: the recognition rates shown on the image are the ones after the cross validation was performed for total 5496 samples.

As seen from Figure 4.3, generally the recognition rates increase as the number of selected bands increases, which is expectable since more and more information will be included, and hence contributed to the classification when the number of selected bands goes up. For each walnut category, the light meat has the best outcome, and the outer shell has the worst outcome among all four categories, which agrees with what was found during the experiment. As the number of selected bands reaches 10, which represents only 13% of total acquired hyperspectral image data, the overall recognition rate rises above 90%. Given the top 10 optimal wavelengths selected by ICA, the confusion matrix of test result is given in Table 4.2. The recognition errors of proposed ICA-kNN approach with 10 optimal wavelengths are also shown in Figure 4.4.

Table 4.2. Confusion matrix of test results

True Labels	Estimated Labels				Totals
	Light Meat	Dark Meat	Inner Shell	Outer Shell	
Light Meat	521	1	0	3	525
Dark Meat	13	677	0	57	747
Inner Shell	0	0	622	25	647
Outer Shell	4	119	16	690	829
Totals	538	797	638	775	2748

In Figure 4.4, both type I and type II errors were calculated for each walnut category. Type I error is the error rate of missing classified samples in each category. While the type II error is the error rate of false classified samples in each category. As seen in Figure 4.4, the light meat has the lowest error rates, and both dark meat and outer shell have relative high error rates, which is because these two categories have the similar hyperspectral responses under most wavelengths (This can also be seen in Figure 4.1), and hence can be mixed up during the classification.

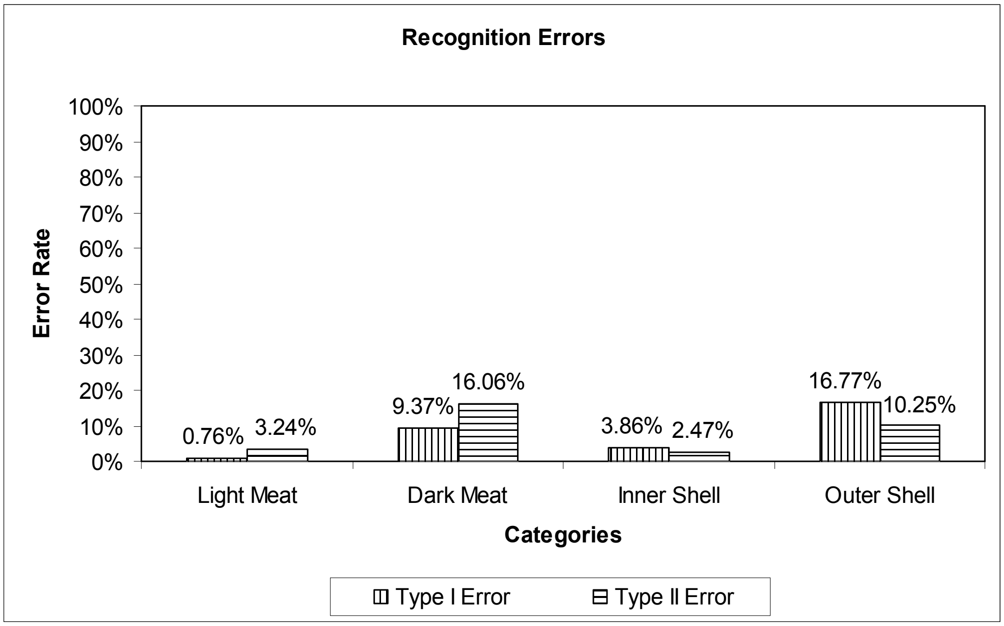

Figure 4.4 The relationship between walnut categories and error rates according to the proposed ICA-kNN approach with selected 10 optimal wavelengths.

Although proposed ICA-kNN approach gives promising results in terms of extracting the most important information for the classification while keeping the redundancy to be minimal, a detailed comparison between proposed method and direct kNN classifier is still needed in order to quantitatively evaluate the effectiveness of ICA-kNN classifier. To fulfill this goal, the direct kNN classifier employing all 79 bands was also tested during the study, and then compared to the ICA-kNN method. The results are shown in Figure 4.5.

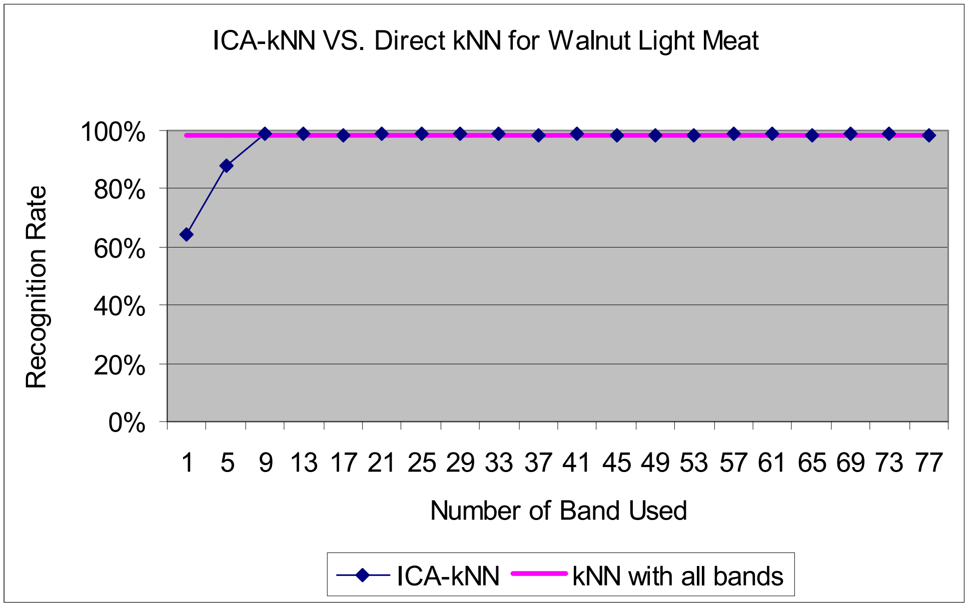
ICA-kNN VS. Direct kNN for Walnut Light Meat
100%
80%
60%
40%
20%
0%
Recognition Rate
1 5 9 13 17 21 25 29 33 37 41 45 49 53 57 61 65 69 73 77
Number of Band Used
ICA-kNN
kNN with all bands

(a)

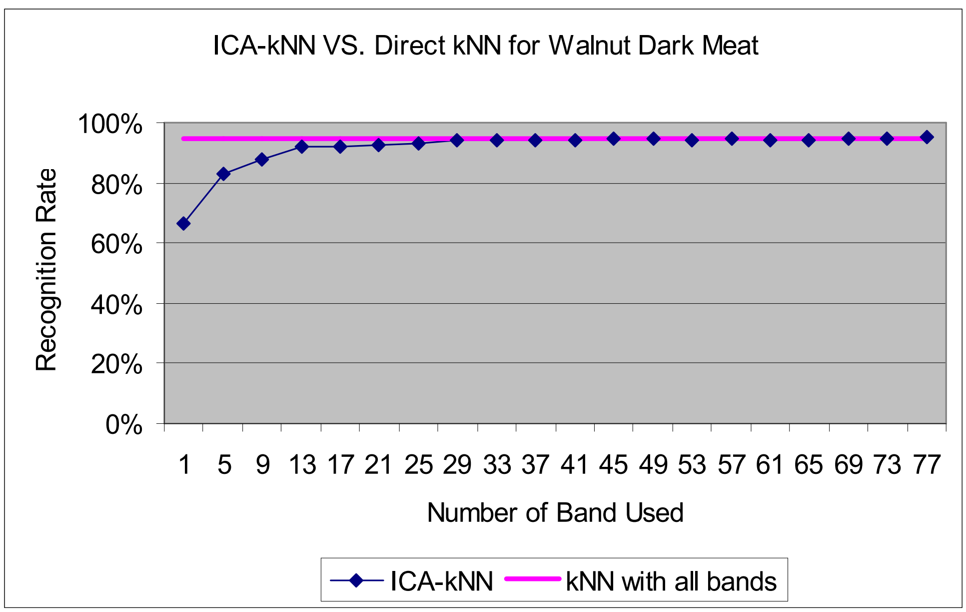
ICA-kNN VS. Direct kNN for Walnut Dark Meat
100%
80%
60%
40%
20%
0%
Recognition Rate
1 5 9 13 17 21 25 29 33 37 41 45 49 53 57 61 65 69 73 77
Number of Band Used
ICA-kNN
kNN with all bands

(b)

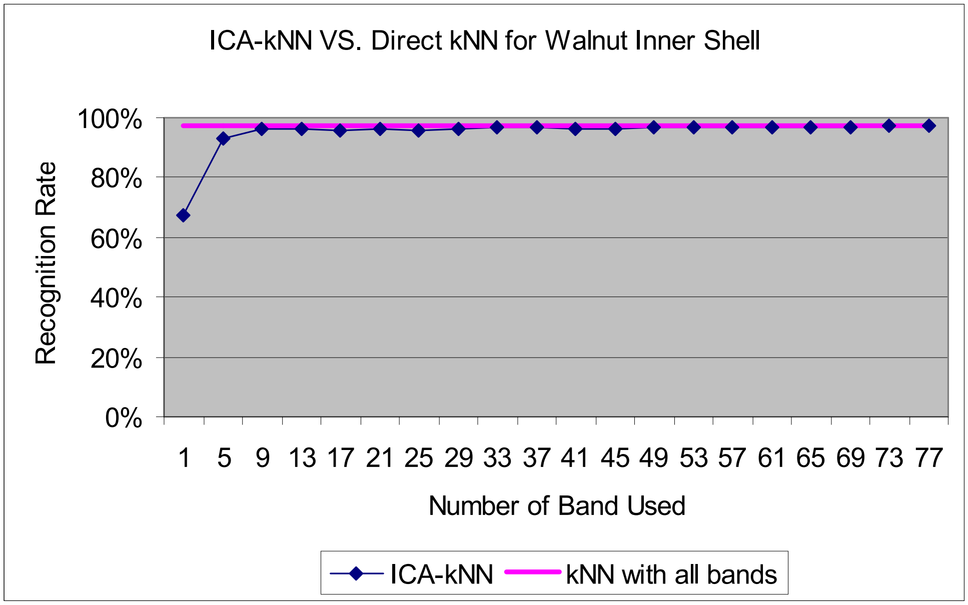
ICA-kNN VS. Direct kNN for Walnut Inner Shell
Recognition Rate
100%
80%
60%
40%
20%
0%
1 5 9 13 17 21 25 29 33 37 41 45 49 53 57 61 65 69 73 77
Number of Band Used
ICA-kNN
kNN with all bands

(c)

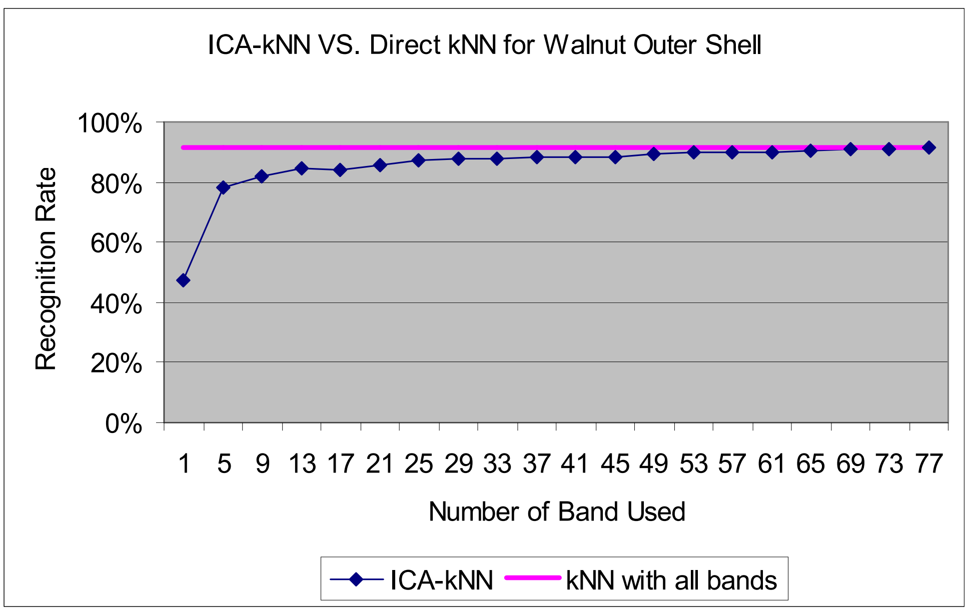
ICA-kNN VS. Direct kNN for Walnut Outer Shell
Recognition Rate
100%
80%
60%
40%
20%
0%
1 5 9 13 17 21 25 29 33 37 41 45 49 53 57 61 65 69 73 77
Number of Band Used
ICA-kNN
kNN with all bands

(d)

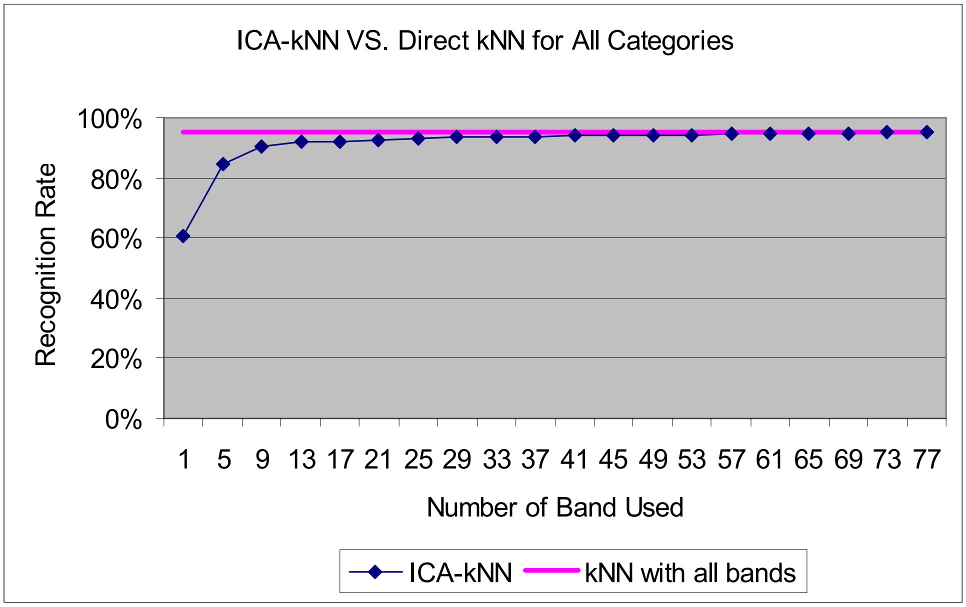

(e)

Figure 4.5. The comparison between proposed ICA-kNN approach and the direct kNN classifier using all 79 bands information. (a) Walnut light meat; (b) Walnut dark meat; (c) Walnut inner shell; (d) Walnut outer shell; (e) All categories. Notice: Every point on the horizontal purple line was calculated from all 79 wavelengths, while the blue curve was plotted according to the corresponding number of bands shown on the x axis.

As seen from figure 4.5, as the number of used band increases, the recognition rate of ICA-kNN approach tends to reach the result of direct kNN classifier for each walnut category. This agrees with what was found in the experiment, and is also expectable since the performance of ICA-kNN must be improved as more and more band information is involved into the classification. However, the value of ICA-kNN method is it matches the recognition rate of direct kNN classifier very "quickly". In other words, the proposed ICA-kNN approach can match the performance of direct kNN, which employs all 79 bands data, with significantly reduced band information. In figure 4.5 (a), only top 9 optimal bands information is needed for proposed ICA-kNN approach to match the performance of direct kNN method, about 98.6% recognition rate for light meat category. Similarly, in figure 4.5 (c), only top 9 optimal bands are need for ICA-KNN approach to match the performance of direct kNN method, which is about 94.6% recognition rate for inner shell category. In other words, the band redundancy is quite high (about 89%) in both walnut light meat and inner shell. In figure 4.5 (b), the recognition rate of ICA-kNN reaches that of direct kNN when top 25 optimal bands are employed for the walnut dark meat category, which is about 93.2% recognition rate and not as easy to match the direct kNN method in terms of classification. However, 68% of the original band data can still be reduced to keep the same the recognition performance comparing to the direct kNN method. Seen from figure 4.5 (d), for the walnut outer shell category, which is the toughest group to be classified, only 90.4% recognition rate was obtained even under direct kNN classifier with all 79 bands used. This agrees with what was found during the study. Meanwhile, more band information (top 53 optimal bands) is also necessary for the ICA-kNN to match the performance of direct kNN. However 33% of the bands data can still be squeezed out without sacrificing the recognition rate when ICA based optimal band selection approach was involved. When overall recognition rate is considered in figure 4.5 (e), the top 29 optimal bands are needed for the ICA-kNN to achieve the same recognition performance as the direct kNN method (about 93.8%), which is a 63% reduction of the original band data. In addition, only 10 optimal bands can make the classification rate go above the 90%, which was also demonstrated in figure 4.3. Given the detailed comparison described above, the ICA based optimal band selection approach shows its capability to extract the key information from the high dimensional hyperspectral image data while keeping redundancy minimal.

4.5 Conclusions

Currently hyperspectral imaging technology received more and more attention in the food quality and safety research area due to its ability to provide the rich information, which made it possible to gain otherwise unavailable insights into the chemical and/or physical characteristics of the walnut samples. However, one persistent problem associated with this technology is how to deal with the huge amount of data acquired by the hyperspectral imaging device, and hence improve the efficiency of the application system. In this chapter, an ICA based optimal band selection approach was presented in order to extract the most important information for the walnut shell and meat differentiation. The kNN classifier was followed to evaluate the performance of ICA approach. The experimental results showed that, with the proposed ICA-kNN only the top 10 optimal bands, compared to the total of 79 band, were necessary to achieve the 90.6% overall recognition rate. Furthermore, detailed comparisons between the proposed method and the direct kNN classifier with a total of 79 bands used were also conducted. The consistent results of the ICA-kNN method were obtained among all the walnut categories: the percentage of hyperspectral data reduction ranging from 33% to 89% was achieved for each walnut category without losing classification performance compared to the direct kNN classifier. Both the experimental results and the comparison showed that the ICA optimal band selection method successfully extracts the key information from the high dimensional hyperspectral image data while keeping the redundancy minimal, and the proposed ICA-kNN approach is efficient for the application of walnut shell and meat differentiation under fluorescence hyperspectral imagery.

5 Summary

In this Ph.D. research, two meaningful topics have been investigated. One is sinogram restoration for ultra-low-dose multi-slice helical CT. The other is automated walnuts shell fragments detection using hyperspectral fluorescence imaging technology. The following conclusions can be drawn:

(1) In the first topic, a nonparametric smoothing method with thin plate smoothing splines and the roughness penalty was proposed to restore the ultra-low-dose CT raw data acquired under 119 kVp and 10 mAs protocols. Both objective and subjective comparisons between proposed method and the conventional 1D sinogram based cubic spline smoothing approach were conducted. The results favor the proposed method, which gave a reconstructed CT image with better contrast and less noise comparing to the 1D based approach.

(2) In the second topic, we employed hyperspectral fluorescence imaging for sensitive detection of shell fragments in walnuts meat. Results demonstrated the feasibility of applying hyperspectral fluorescence imaging to walnuts shell fragments detection system. We found that the hyperspectral fluorescence imaging technique was an effective way to identify walnuts shell fragments from the meats.

(3) The PCA-GMM based Bayesian classifier and Gaussian Kernel based SVM method were presented to identify the walnuts' shell and meat in hyperspectral fluorescence imagery. The recognition results showed that the

proposed approaches were effective for the walnut shell and meat classification.

(4) In order to deal with huge amount of data acquired by the hyperspectral imaging device, and improve the efficiency of the application system, an ICA based optimal band selection approach was introduced to extract the most important information for the walnut shell and meat differentiation. The experiment results showed that ICA optimal band selection method successfully extract the key information from the high dimensional hyperspectral image data while keeping the redundancy minimal.

6 Suggestions for Further Study

Further research and development efforts are necessary to extend the existing research. An automated walnut shell fragment detection system can be studied and developed, with functionalities including parallel on-line hyperspectral image processing, and real-time tracking and rejection sub-system controls. Currently, walnut samples studied in this research have the same harvest age and are from the same growing region. In the future, samples with different harvest age, cultivar, and growing regions can be investigated. Additional experiments can be done to explore the relationships between different fluorescence response of the shell and meat as a function of different humidity content, harvest age, cultivar, and growing region. Meanwhile, statistical models other than Gaussian Mixture model can be further evaluated to find a better fit of the image data.

In the ultra-low dose CT research, the proposed sinogram restoration method has been evaluated by the radiologists. In the future, a clinical study involving both radiologists and patients can be conducted. More CT data regarding other diseases may be further evaluated. The computational efficiency of proposed method can also be improved.

7 Publications during Ph.D. Study

Jiang, L., K. Siddiqui, B. Zhu, Y. Tao, and E. Siegel. Sinogram Restoration for Ultra-Low-dose X-ray Multi-slice Helical CT by Block-based Thin-Plate Smoothing Splines and Performance Evaluation with Real Patients Data. Journal of Digital Imaging. (Submitted).

Jiang, L., B. Zhu, X. Rao, G. Berney, and Y. Tao. Discrimination of Black Walnut Shell and Pulp in Hyperspectra1 Fluorescence Imagery using Gaussian Kernel Function Approach. J. of Food Engineering. Vol. 81(1): 108-117, 2007.

Jiang, L., B. Zhu, H. Jing, X. Chen, X. Rao, and Y. Tao. Gaussian Mixture Model Based Walnut Shell and Meat Classification in Hyperspectral Fluorescence Imagery. Trans. of ASABE. Vol.50 (1): 153-160, 2007.

Zhu, B., L. Jiang, F. Jin, L. Qin, and Y. Tao. ICA-kNN based Optimal Wavelength Selection and Walnuts Shell and Meat Differentiation under Fluorescence Hyperspectral Imagery. Sensing and Instrumentation for Food Quality and Safety. Vol. 1:123–131, 2007.

Jiang, L., K. Siddiqui, B. Zhu, Y. Tao, and E. Siegel. 2007. Sinogram Restoration for Low-dose X-ray Helical CT by Nonparametric Regression. Proc. SPIE. Medical Imaging, Feb. 2007.

Jiang, L., K. Siddiqui, B. Zhu, Y. Tao, and E. Siegel. A Comparative Evaluation Study for Ultra-low Dose CT Images Reconstructed by 2 Different Sinogram Restoration Methods. 93rd RSNA Annual Meeting, Chicago, Dec. 2007.

Jiang, L., B. Zhu, X. Rao, G. Berney, and Y. Tao. Black Walnut Shell and Meat Classification using Hyperspectral Fluorescence Imaging. ASABE 2007 Annual Meeting, Minnesota, Jun. 2007.

Jiang, L., B. Zhu, X. Rao, G. Berney, and Y. Tao. ICA Based Band Selection for Black Walnut Shell and Meat Classification in Hyperspectral Fluorescence Imagery. ASABE 2007 Annual Meeting, Minnesota, Jun. 2007.

Jin, F., L. Qin, L. Jiang, B. Zhu, and Y. Tao. Novel separation method of black walnut meat from shell using invariant features and a supervised self-organizing map. J. of Food Engineering, Vol. 88 (1): 75-85, 2008.

Bibliography

Belouchrani, A., K.Abed-Meraim, J.F. Cardoso, and E. Moulines. (1997). A blind source separation technique using second order statistics. *IEEE Trans. on Signal Processing.* 45(2): 434-444.

Biersack, H. and L. M. Freeman (2007). *Clinical Nuclear Medicine*. Springer, New York, 2007.

Board on Radiation Effects Research (BRER), (2006). *Health Risks from Exposure to Low Levels of Ionizing Radiation: BEIR VII Phase 2*.

Brenner, D. J. and E. J. Hall (2007). Computed Tomography — An Increasing Source of Radiation Exposure. *The New England Journal of Medicine.* 357(22):2277-2284.

Brenner, D. J. et al. (2001). Estimated Risks of Radiation-Induced Fatal Cancer from Pediatric CT. *American Journal of Roentgenology* 176: 289–296.

Burges, C. J. C. (1998). A Tutorial on Support Vector Machines for Pattern Recognition. *Data Mining and Knowledge Discovery,* 2(2): 121-167.

Campbell, J. B. (2002). *Introduction to Remote Sensing.* 3rd ed. Oxford, UK: Taylor & Francis Group.

Casasent, D., and X.-W. Chen. (2003). Waveband selection for hyperspectral data: optimal feature selection. *Proc. SPIE.* 5106: 256-270.

Casasent, D., and X.-W. Chen. (2004). Feature selection from high-dimensional hyperspectral and polarimetric data for target detection. *Proc. SPIE.* 5437: 171-178.

Chang, C. -I, H. Ren, C. -C. Chang, J. O. Jensen, and F. D. Amico. (2004). Estimation of subpixel target size for remotely sensed imagery. *IEEE Transaction on Geoscience and Remote Sensing*, 42(6): 1309-1320.

Chao, K., Y. R. Chen, W. R. Hruschka, and F. B. Gwozdz. (2002). On-line inspection of poultry carcasses by dual-camera system. *J. Food Eng.*, 51: 185-192.

Chen, X., H. Jing, and Tao, Y. (2003). High-resolution real-time X-ray and 3D imaging for physical contamination detection in de-boned poultry meat. *SPIE Photonics East.* Providence, RI.

Cheng, L., Y. Chen, T. Fang and J. Tyan. (2006). Fast Iterative Adaptive Reconstruction in Low-Dose CT Imaging, *IEEE International Conference on Image Processing*. 8-11 Oct. 2006.

Cheng, X., Y. R. Chen, Y. Tao, C. Wang, M. Kim, and A. Lefcourt. (2004). A Novel Integrated PCA and FLD Method on Hyperspectral Image Feature Extraction for Cucumber Chilling Damage Inspection. *Transactions of the ASAE*, 47(4): 1313-1320.

Cohen, D., M. Arnoldussen, G. Bearman, and W. S. Grundfest. (1999). The Use of Spectral Imaging for the Diagnosis of Retinal Disease. *IEEE Lasers and Electro-Optics Society 1999 12th Annual Meeting*, Washington DC, USA, 1: 220-221.

Comon P. (1994). Independent Component Analysis, a new concept? *Signal Processing.* 36(3): 287-314.

Cortes, C. and V. Vapnik. (1995). Support vector networks. *Machine Learning,* 20: 273-297, U.S.A.

Creagh, D. C. and J. H. Hubbell. (1992), X-Ray Absorption (or Attenuation) Coefficients, Sec. 4.2.4. in *International Tables for Crystallography,* Vol. **C,** A.J.C. Wilson, ed. (Kluwer Academic Publishers, Dordrecht), 189-206.

Delwiche, S.R., and C.S. Gaines. (2005). Wavelength selection for monochromatic and bichromatic sorting of fusarium-damaged wheat. *Applied Engineering in Agriculture*. 21(4):681-688.

Dempster, A. P., N. M. Laird, D. B. Rubin. (1977). Maximum Likelihood from Incomplete Data via the EM Algorithm. *Journal of the Royal Statistical Society. Series B (Methodological)* 39 (1): 1–38.

Dendy, P. P., and B. Heaton. (1999). *Physics for Diagnostic Radiology*. USA: CRC Press.

Donnelly, L.F. , K. H. Emery, A. S. Brody, T. Laor, V. M. Gylys-Morin, C. G. Anton, S. R. Thomas and D. P. Frush. (2001). Minimizing Radiation Dose for Pediatric Body Applications of Single-Detector Helical CT. *American Journal of Roentgenology* 176 (2): 303–306.

Dove, E., (2004). *Physics of Medical Imaging – An Introduction*. Biomedical Engineering, University of Iowa.

Du, H., H. Qi, X. Wang, R. Ramanath, and W. E. Snyder. (2003). Band selection using independent component analysis for hyperspectral image processing. *Proceedings of the 32nd Applied Imagery Pattern Recognition Workshop (AIPR '03).* 93–98, Washington, DC, USA, October 2003.

Duda, R., P. Hart, and D. Stork. (2001). *Pattern Classification* (2nd ed.). Wiley-Interscience, U.S.A.

Elbakri, I. and J. Fessler. (2002). Statistical image reconstruction for polyenergetic X-ray computed tomography. *IEEE Trans. Med. Imag.* 21(2): 89-99.

Elbakri, I. and J. Fessler. (2003). Efficient and accurate likelihood for iterative image reconstruction in X-ray computed tomography. *SPIE Medical Imaging*. 5032: 1839-1850.

FDA (U. S. Food and Drug Administration). 2009. Computed Tomography (CT). [On-line]. Available: WWW: http://www.fda.gov/cdrh/CT/risks.html

Fessler, J. A. (1994). Penalized weighted least-squares image reconstruction for positron emission tomography. *IEEE Trans. Med. Imag.* 13(2), 290-300.

Feynman, R., R. Leighton and M. Sands. (1963). *The Feynman Lectures on Physics,* 1. USA: Addison-Wesley.

Fukunaga, K., (1990). *Introduction to Statistical Pattern Recognition* (2nd ed.). Acedemic, New York, U.S.A.

Goldman, L. W., (2007) Principles of CT: Radiation Dose and Image Quality *Journal of Nuclear Medicine Technology,* 35(4): 213-225.

Goutte, C. (1997). Note on free lunches and cross-validation. *Neural Computation*, 9, 1211-1215.

Green P. and B. Silverman. (1994). *Nonparametric Regression and Generalized Linear Models*, Chapman Hall, London.

Guo, G., S. Z. Li, and K. Chan. (2000). Face Recognition by support vector machines. *Proc. 4th IEEE International Conference on Automatic Face and Gesture Recognition,* 196-201, Grenoble, France.

Haertel, V. and D. A. Langrebe. (1999). On the classification of classes with nearly equal spectral response in remote sensing hyperspectral image data. *IEEE Transactions on Geoscience and Remote Sensing*, 37(5): 2287-2294.

Haff, R.P., and Pearson, T.C. (2006). Spectral Band Selection for Optical Sorting of Pistachio Nut Defects. *Transactions of the ASABE*. 49(4): 1105-1113

Hammons Products Company. 1998. World Consumption and Production Trends. International Nut Council.

Hammons Products Company. 2008. [On-line]. Available: WWW: http://www.black-walnuts.com/.

Hart, D and B. F. Wall (2004). UK population dose from medical X-ray examinations. *European Journal of Radiology*. 50(3): 285–291.

Hatcher, R., L. Johnson, G. Hopper, J. Pease, and J. Johnson. (1998). Tree crops for Marginal Farmland Black Walnut. *Virginia Cooperative Extension*. 446-602.

Haugland, R. P. (1996). Introduction to Fluorescence Techniques, in *Handbook of Fluorescent Probes and Research Chemicals*, Molecular Probes, Inc., Eugene, OR, pp. 1–4.

Health Alliance. 2009.Lung Cancer. [On-line]. Available: WWW: http://www.health-alliance.com/cancer/Lung/detection.html

Henke, B.L., E. M. Gullikson, and J. C. Davis. (1993). X-ray interactions: photoabsorption, scattering, transmission, and reflection at E=50-30000 eV, Z=1-92, *Atomic Data and Nuclear Data Tables* 54(2):181-342.

Herault, J. and C. Jutten. (1986). Space or time adaptive signal processing by neural network models. *Neural Networks for Computing.* Snowbird, Utah.

Hogg, R., J. McKean, and A. Craig. (2005). *Introduction to Mathematical Statistics*. 359-364. Upper Saddle River, NJ: Pearson Prentice Hall.

Hsieh, J. (1998). Adaptive streak artifact reduction in computed tomography resulting from excessive X-ray photon noise. *Med. Phys.* 25, 2139–2147.

Hsieh, J., (1997). Nonstationary noise characteristics of the helical scan and its impact on image quality and artifacts, *Med. Phys*. 24: 1375-1384.

Jiang, L., B. Zhu, H. Jing, X. Chen, X. Rao, and Y. Tao. (2007b). Gaussian Mixture Model Based Walnut Shell and Meat Classification in Hyperspectral Fluorescence Imagery. *Trans. of ASABE*. 50(1): 153-160.

Jiang, L., B. Zhu, X. Rao, G. Berney, and Y. Tao. (2007a). Discrimination of Black Walnut Shell and Pulp in Hyperspectra1 Fluorescence Imagery using Gaussian Kernel Function Approach. *J. of Food Engineering*. 81(1): 108-117.

Jiang, L., K. Siddiqui, B. Zhu, Y. Tao and E. Siegel. (2007c). Sinogram restoration for ultra-low-dose X-ray multi-slice helical CT by nonparametric regression, *SPIE Medical Imaging*, 6510: 65105L.

Jiang, L., K. Siddiqui, B. Zhu, Y. Tao and E. Siegel. (2007d). A Comparative Evaluation Study for Ultra-low Dose CT Images Reconstructed by two Different Sinogram Restoration Methods, RSNA. 25-30 November 2007, Chicago.

Jing, H., and Y. Tao. (2001). Scattering Laser Line Image Recovery for 3D Poultry Meat Processing. *ASAE paper,* 01-3161.

Jones, J., R. Mueller, and V. Sambeek. (1998). *Nut Production Handbook for Eastern Black Walnut*. Southwest Missouri Resources. Conservation & Development (RC&D), Inc.

Jung, K., K. Lee, S. Kim, Y. Pyeun and J. Lee, (2000). Low-dose, volumetric helical CT: image quality, radiation dose, and usefulness for evaluation of bronchiectasis, *Invest. Radiology*. 35: 557-563.

Kalra, M. K., M. M. Maher, D. V. Sahani, M. A. Blake, P. F. Hahn, G. B. Avinash, T. L. Toth, E. Halpern and S. Saini. (2003). Low-Dose CT of the Abdomen: Evaluation of Image Improvement with Use of Noise Reduction Filters—Pilot Study, *Radiology.* 228, 251-256.

Kim, M., A. M. Lefcourt, Y. R. Chen, I. Kim, D. E. Chan, and K. Chao. (2002). Multispectral Detection of Fecal Contamination on Apples Based on Hyperspectral Imagery: Part II. Application of Hyperspectral Fluorescence Imaging. *Transaction of ASAE*, 45(6): 2039-2047.

Kim, M., Y. Chen, and P. Mehl. (2001). Hyperspectral Reflectance and Fluorescence Imaging System for Food Quality and Safety. *Transactions of the ASAE*, 44(3): 721-729.

Krishnan, P., and A. Berlage. (1984). Separation of Shells from Walnut Meats Using Magnetic Methods. *Trans. ASAE.* 27: 1990-1992.

La Rivière, P. and D. Billmire. (2005). Reduction of noise-induced streak artifacts in X-ray computed tomography through spline-based penalized-likelihood sinogram smoothing, *IEEE Trans. Med. Imag.* 24: 105–111.

La Rivière, P. and X. Pan. (2000). Nonparametric regression sinogram smoothing using a roughness-penalized Poisson likelihood objective function. *IEEE Trans. Med. Imag.* 19: 773-786.

Lakowicz, J. R. (1999). *Principles of Fluorescence Spectroscopy*, 2nd ed, Plenum Publishing, New York.

Langley, P., W. Iba, and K. Thompson. (1992). An analysis of Bayesian classifiers. *Proc. Tenth National Conference on Artificial Intelligence.* 223-228. San Jose, CA: AAAI Press.

Larson, D. B., S. B. Rader, H. P. Forman, and L. Z. Fenton (2007). Informing parents about CT radiation exposure in children: it's OK to tell them. *American Journal of Roentgenology* 189 (2): 271–275.

Li, T., X. Li, J. Wang, J. Wen, H. Lu, J. Hsieh and Z. Liang. (2004). Nonlinear Sinogram Smoothing for Low-Dose X-ray CT, *IEEE Trans. Nucl. Science*. 51: 2505-2513.

Lu, H., X. Li and Z. Liang. (2002). Analytical Noise Treatment for Low-dose CT Projection Data by Penalized Weighted Least-square Smoothing in the K-L Domain *SPIE Medical Imaging*, 4682, 146-152.

Lu, R., (2003). Detection of Bruises on Apples Using Near-Infrared Hyperspectral Imaging. *Trans. ASAE.* 46(2): 523-530.

Lyman, O., (2001). *An Introduction to Statistical Methods and Data Analysis*. 5th ed. Michael Longnecker.

Ma, L. and Y. Tao. (2005). An Infrared and Laser Range Imaging System for Non-invasive Estimation of Internal Temperatures in Cooked Chicken Breasts. *Trans. ASAE*. 48(2): 681-690.

Mozumdar, B. C. (2003). The Control Of Radiation Exposure From CT Scans . *The Internet Journal of Radiology.* 3:1-10.

Novelline, R., (1997) *Squire's Fundamentals of Radiology*. Harvard University Press. 5th edition.

Osuna, E., R. Freund, and F. Girosi. (1997). Training Support Vector Machines: an Application to Face Detection. *Proc. of CVPR'97,* Puerto Rico.

Park, B., K. C. Lawrence, W. R. Windham, and R. J. Buhr. (2002). Hyperspectral Imaging for Detecting Fecal and Ingesta Contaminants on Poultry Carcasses. *Transactions of the ASAE*, 45(6), 2017-2026.

Park, B., K. Lawrence, W. Windham, and R. Buhr. (2001). Hyperspectral Imaging for Detecting Fecal and Ingesta Contamination on Poultry Carcasses. ASAE paper no. 01-3130 presented at the ASAE 2001 International Annual Meeting. July 30-August 1, Sacramento, California.

Pearson, T., and R. Young. (2002). Automated Sorting of Almonds with Embedded Shell by Laser Transmittance Imaging. *App. Eng. Agric.* 18(5): 637-641.

Peng, Y. and R. Lu. (2006). An Lctf-Based Multispectral Imaging System for Estimation of Apple Fruit Firmness: Part Ii. Selection of Optimal Wavelengths and Development of Prediction Models. *Trans. ASAE.* 49(1): 269-275.

Permuter, H., J. Francos, and I. Jermyn. (2006). A study of Gaussian mixture models of color and texture features for image classification and segmentation. *Pattern Recognition.* 39(4): 695-706.

Povinelli, R. J., M. T. Johnson, A. C. Lindgren, and J. Ye. (2004). Time Series Classification using Gaussian Mixture Models of reconstructed phase spaces. *IEEE Trans. knowledge and data engineering.* 16(6): 779-783.

Sauer, K. and B. Liu. (1991). Nonstationary filtering of transmission tomograms in high photon counting noise, *IEEE Trans. Med. Imag.* 10(3): 445-452

Tao, Y., Z. Chen, and C. Griffis. 2004. Chick feather pattern recognition. *IEE Proc – Vision, Image and Signal Processing.* 151(5): 337-344.

Vargas, A., M. Kim, Y. Tao, A.M. Lefcourt, Y. Luo, and Y.R. Chen. (2004b). Detection of fecal contamination on cantaloupes using hyperspectral fluorescence imagery. *Journal of Food Engineering.* 70(8-2005): 471-476.

Vargas, A.M., Y. Tao, M. Kim, A.M. Lefcourt, Y. Luo, and Y.R. Chen. (2004a). Safety Inspection of Fruit and Vegetables Using Optical Sensing and Imaging Techniques. *2004 ASAE Annual International Meeting*. Ottawa, Ontario, Canada. August 31- July 4, 2004.

Wahba, G. (1990). *Spline models for observational data*, Philadelphia: Society for Industrial and Applied Mathematics.

Wang, J., T. Li, H. Lu and Z. Liang. (2006). Noise Reduction for Low-dose Single-slice Helical CT Sinograms. *IEEE Trans. Nucl. Science*, 53(3): 1230-1237.

Wen, Z. and Y. Tao, (2000). Dual-camera NIR/MIR imaging for stem-end/calyx identification in apple defect sorting. *Trans. ASAE*, 43(2): 449-452.

Xing, J., M. Ngadi, N. Wang, and J. D. Baerdemaeker. (2006). Wavelength Selection for Surface Defects Detection on Tomatoes by Means of a Hyperspectral Imaging System. Paper number 063018, *2006 ASAE Annual Meeting*.

Yao, H., L. Tian, and N. Noguchi. (2001). Hyperspectral Imaging System Optimization and Image Processing. *ASAE International Annual Meeting*. July 30-August 1, Sacramento, California.

Zhu, B., L. Jiang, and Y. Tao. (2007). 3D Shape Enhanced Transform for Automatic Apple Stem-End/Calyx Identification. *Optical Engineering,* 46(1):017201.

Zhu, B., L. Jiang, X. Cheng, and Y. Tao. (2005). 3D surface reconstruction of apples from 2D NIR images. *Proc. SPIE 6000*, 242-251.

Zhu, H., and R. Rohwer. (1996). No free lunch for cross-validation. *Neural Computation.* 8: 1421-1426.

Ziehe, A. and K.-R. Miller. 1998. TDSEP - an efficient algorithm for blind separation using time structure. *ICANN'98*, 675-680, Skovde.

Zuzak, K. J., M. D. Schaeberle, I. W. Levin, N. E. Lewis, J. Freeman, J. D. McNeil, and L. C. Cancio. (1999). Visible and infrared hyperspectral visualization of normal and ischemic tissue. *Proceedings of the First Joint BMES/EMBS Conference,* Atlanta, GA, USA, 2:1118, 13-16.

Supplemental A

The typical evaluation web pages are shown in Figure SA.1 and Figure SA.2.

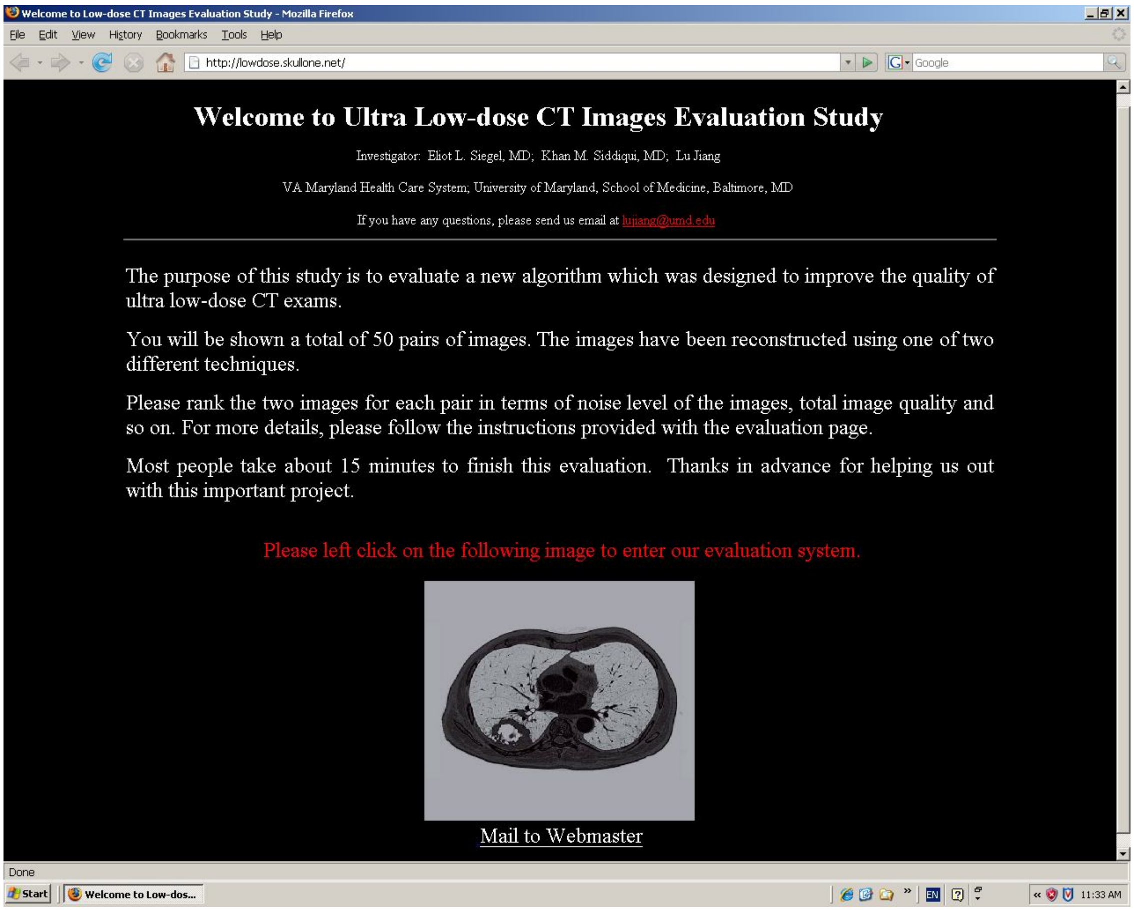

Figure SA.1 The main page of ULD CT image evaluation study website.

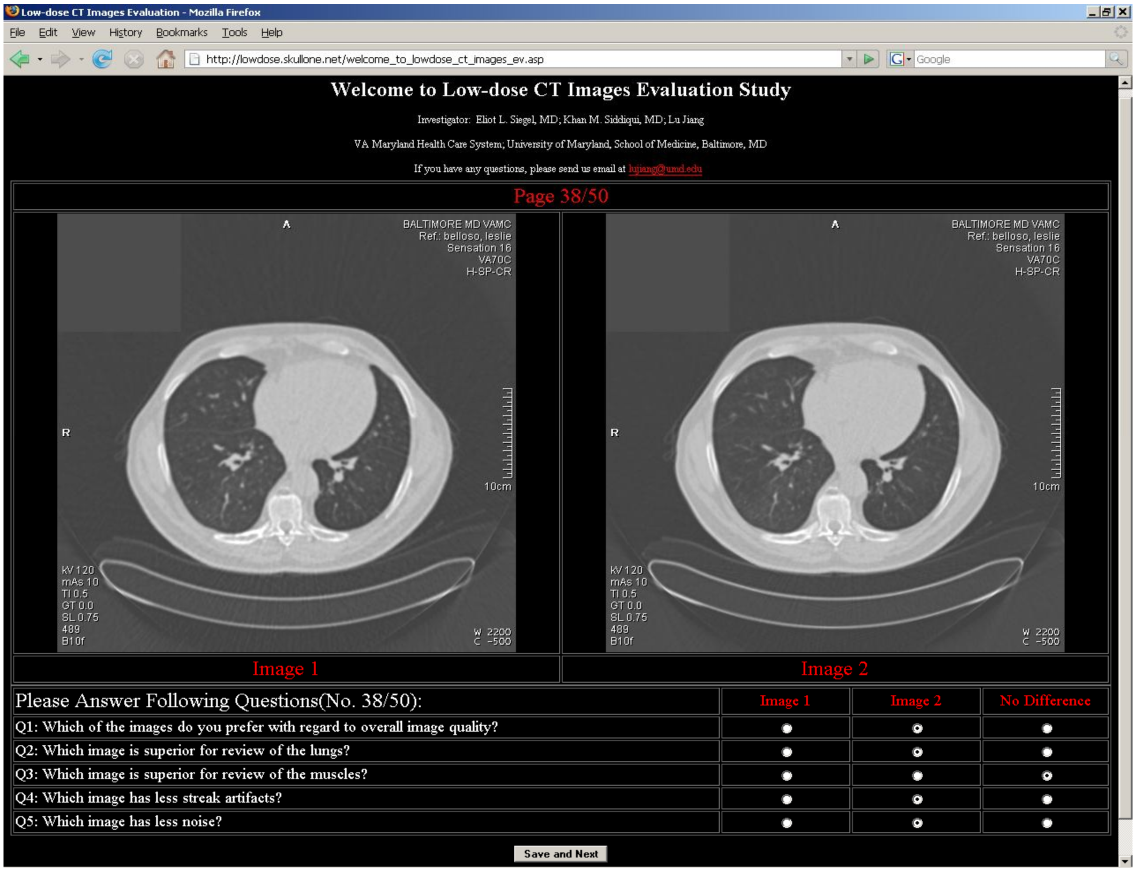

Figure SA.2 The evaluation webpage of ULD CT images study website.